2014

Quantitative Scanning Transmission Electron Microscopy of Thick Samples and of Gold and Silver Nanoparticles on Polymeric Surfaces

Aniruddha Dutta
University of Central Florida

QUANTITATIVE SCANNING TRANSMISSION ELECTRON MICROSCOPY OF THICK SAMPLES AND OF GOLD AND SILVER NANOPARTICLES ON POLYMERIC SURFACES

by

ANIRUDDHA DUTTA
M.S. University of Central Florida, 2010

A dissertation submitted in partial fulfillment of the requirements
for the degree of Doctor of Philosophy
in the Department of Physics
in the College of Sciences
at the University of Central Florida
Orlando, Florida

Fall Term
2014

Major Professor : Helge Heinrich

ABSTRACT

Transmission Electron Microscopy (TEM) is a reliable tool for chemical and structural studies of nanostructured systems. The shape, size and volumes of nanoparticles on surfaces play an important role in surface chemistry. As nanostructured surfaces become increasingly important for catalysis, protective coatings, optical properties, detection of specific molecules, and many other applications, different techniques of TEM can be used to characterize the properties of nanoparticles on surfaces to provide a path for predictability and control of these systems.

This dissertation aims to provide fundamental understanding of the surface chemistry of Electroless Metallization onto Polymeric Surfaces (EMPS) through characterization with TEM. The research focuses on a single EMPS system: deposition of Ag onto the cross-linked epoxide "SU8", where Au nanoparticles act as nucleation sites for the growth of Ag nanoparticles on the polymer surface. TEM cross sections were analyzed to investigate the morphology of the Au nanoparticles and to determine the thicknesses of the Ag nanoparticles and of the Ag layers. A method for the direct measurement of the volume and thickness of nanomaterials has been developed in the project using High-Angle Annular Dark-Field (HAADF) Scanning Transmission Electron Microscopy (STEM). The morphology of Au and Ag NPs has been studied to provide reliable statistics for 3-D characterization. Deposition rates have been obtained as a function of metallization conditions by measuring the composition and thickness of the metal for EMPS.

In the present work a calibration method was used to quantify the sensitivity of the HAADF detector. For thin samples a linear relationship of the HAADF signal with the thickness of a material is found. Cross-sections of multilayered samples provided by Triquint Semiconductors, FL, were analyzed as calibration standards with known composition in a TECNAI F30

transmission electron microscope to study the dependence of the HAADF detector signal on sample thickness and temperature.

Dynamical diffraction processes play an important role in electron scattering for larger sample thicknesses. The HAADF detector intensity is not linearly dependent on sample thicknesses for thick samples. This phenomenon involves several excitation processes including Thermal Diffuse Scattering (TDS) which depends on temperature-dependent absorption coefficients. Multislice simulations have been carried out by Python programming using the scattering parameters [2] available in the literature. These simulations were compared with experimental results. Wedge-shaped Focused Ion Beam (FIB) samples were prepared for quantitative HAADF-STEM intensity measurements for several samples and compared with these simulations. The discrepancies between the simulated and experimental results were explained and new sets of absorptive parameters were calculated which correctly account for the HAADF-STEM contrasts. A database of several pure elements is compiled to illustrate the absorption coefficients and fractions of scattered electrons per nanometer of the sample.

In addition, the wedge-shaped FIB samples were used for studying the HAADF-STEM contrasts at an interface of a high- and a low-density material. The use of thick samples reveals an increased signal at the interfaces of high- and low-density materials. This effect can be explained by the transfer of scattered electrons from the high density material across the interface into the less-absorbing low-density material. A ballistic scattering model is proposed here for the HAADF-STEM contrasts at interfaces of thick materials using Python. The simulated HAADF-STEM signal is compared with experimental data to showcase the above phenomenon. A detailed understanding of the atomic number contrast in thick samples is developed based on the

combination of experimental quantitative HAADF-STEM and simulated scattering. This approach is used to describe the observed features for Ag deposition on SU8 polymers.

THIS DISSERTATION IS DEDICATED TO MY FAMILY

ACKNOWLEDGMENTS

The present work would not have been possible without the guidance of my advisor, Dr. Helge Heinrich. He introduced me in the exciting world of Electron Microscopy and I would like to thank him for spending time with me in discussing measurements and models and writing complex codes. “You are one of the best teachers I have ever met and I thank you from the bottom of my heart for your financial and academic support to make this work successful”.

I would like to thank my co-advisor, Professor Stephen Kuebler of Chemistry Department, UCF for giving me a chance to work in the NSF grant #0809821 with his group and also for serving on my dissertation committee. I’m especially thankful for his thought-provoking questions and suggestions. I am thankful to Dr. Aniket Bhattacharya for the insightful discussions I had with him.

I would also like to thank Professor Lee Chow, Dr. Enrique Del Barco and Dr. Bo Chen of Physics Department, UCF for reviewing my dissertation and serving on my dissertation committee.

I would like to acknowledge AMPAC’s Material Characterization Facility (MCF) for providing me the chance to learn different material characterization techniques. Special thanks to Mikhail and Kirk for keeping the instruments running and for the training. Thank You Karen for processing my equipment reservations in time. I would also like to thank Ms. Cindy Harle, Ms. Kari Stiles and Ms. Angelina Feliciano for your excellent administrative support.

My sincere gratitude to all faculty and staff members of Physics Department at UCF. Special thanks to Elizabeth and Felix for the administrative support. I would like to thank Dr. Biao

Yuan and Mr. Haider Ali as my lab members. A special thanks to Dr. Kuebler's group and Dr. Florencio Eloy Hernández in Chemistry department for providing samples for measurements.

Graduate Student Association (GSA) and Student Government Association (SGA) financially supported me for attending several conferences and also with Graduate Excellence Fellowships. I would like to acknowledge the Graduate School for their help.

I would like to thank TriQuint Semiconductors, UCF, and the National Science Foundation (NSF-CHE grant 0809821) that funded my Assistantship since Fall 2008.

Last, but not least, I am indebted to my parents and my wife who supported me at every step of this journey. They never stopped encouraging me and lifted my spirits in tough times.

TABLE OF CONTENTS

LIST OF FIGURES

LIST OF TABLES

LIST OF ACRONYMS/ABBREVIATIONS

2-D	Two-Dimensional Space
3-D	Three-Dimensional Space
ADF	Annular Dark Field
AEP	Aminoethylenepeparazine
AMPAC	Advanced Materials Processing and Analysis Center
BF	Bright-Field
CB	Contrast & Brightness
CBED	Convergent-Beam Electron Diffraction
CCD	Charge-Coupled Device
DF	Dark-Field
EDS	Energy-Dispersive X-Ray Spectroscopy
EELS	Electron Energy-Loss Spectroscopy
EFTEM	Energy Filtered Transmission Electron Microscopy
EMPS	Electroless Metallization on Polymeric Surfaces
EXLO	Ex Situ Lift Out
FIB	Focused Ion Beam
FL	Florida
HAADF	High-Angle Annular Dark-Field
HRTEM	High-Resolution Transmission Electron Microscopy
INLO	In Situ Lift Out
MCF	Materials Characterization Facility

NP	Nano Particle
NPs	Nanoparticles
STDEV	Standard Deviation
STEM	Scanning Transmission Electron Microscopy
TDS	Thermal Diffuse Scattering
TEPA	Tetraethylenepentamine
TEM	Transmission Electron Microscopy
XRD	X-Ray Diffraction

LIST OF SYMBOLS

a_H, a_{Bohr}	Bohr Radius
a_j	Scattering Coefficient
A	Fitting Parameter
b, b'	Incident Electron Beam, Final Electron Beam
b_j	Scattering Coefficient
B	Fitting Parameter, Debye Waller Factor
c	Speed of Light
C	Centigrade, Constant
D_n	Effective Diameter
e	Charge of an Electron
eV	Electron Volt
E	Accelerating Voltage
E_i	Initial Electron Energy
E_f	Final Electron Energy
f	Atomic Scattering Factor
f^e	Elastic Scattering Factor
f_{abs}	Absorptive Scattering Factor
F	Fraction of electrons per nm
$\mathcal{F}$	Fourier Transform
$\mathcal{F}^{-1}$	Inverse Fast Fourier Transform
|g|	Reciprocal Lattice Vector

$g(\omega)$	Phonon Density of States
h	Planck Constant
ħ	Reduced Plank Constant or Dirac Constant
H_n	Height of Ellipsoid
H_t	Average Height of NP
I	Intensity
I_0, $I_{incident}$	Intensity of Incident Beam
k, k'	Initial Wave Vector, Final Wave Vector
K	Prefactor, Kelvin
k_B	Boltzman Constant
m_0	Rest Mass
m	Mass
n1	First Measurement
n2	Second Measurement
N	Total No of NP
N_A	Avogadro's Number
|q|	Scattering Vector
R	Correlation Coefficient. Shielding Radius
T	Temperature, Thickness
T_m	Temperature at Maximum Phonon Frequency
U	Potential
U_x	Thermal Displacement in x Direction

V	Volume, Voltage
W_{at}	Atomic Mass
x_n	Distance Along x
y_n	Distance Along y
Z	Atomic Number
dk	Pixel Size in Diffraction Space
α	Fitting Parameter
γ	Relativistic correction
ε	Initial Slope of Wedge Shaped Sample in per nm
ε_H	Error in Height
ε_V	Error in Volume
ε_0	Vacuum Permittivity
μ	Absorption Coefficient, Reciprocal Mean Free Inelastic Path
θ	Braggs Angle
Θ	Half of the Scattering Angle
λ	Wavelength
π	Mathematical Constant (Ratio of a Circle's Circumference to its Diameter)
σ	Interaction Cross Section
ρ	Density
φ_i	Initial State
φ_f	Final State
$\mathcal{L}$	Fresnel Propagator

ω	Phonon Frequency
ω_m	Maximum Phonon Frequency
σ_H	STD in Height
σ_V	STD in Volume
Θ_{max}	Half of the Outer Radius of the Detector
Θ_{min}	Half of the Inner Radius of the Detector

CHAPTER 1: INTRODUCTION

With emerging new processing techniques for nanostructured materials, improved and accurate characterization techniques are required for proper structural and chemical analysis. As the properties of nanostructures depend on their morphology, structural characterization plays an important role for the precise understanding of these systems. TEM has been an effective analytical tool (both as direct and reciprocal methods) for the study of nanostructures, especially the size, shape and distribution of nanoparticles. 3-D characterization of nanostructures with atomic resolution has already been achieved in several cases, e.g., [3, 4] using TEM.

Electroless Metallization onto Polymeric Surfaces (EMPS) is a functional method for creating electrically conductive and optically reflective structures. Through electroless deposition at ambient temperature, polymeric surfaces with arbitrary shapes can be conformally metalized [5]. Ag/SU-8 EMPS is an effective system for fabricating MEMS, micro-fluidic, photonic devices and also for using in biological systems [6-8]. A study of the morphology and arrangement of metallic nanoparticles (Au & Ag NPs) deposited on SU-8 polymeric surfaces using electroless deposition is presented in this dissertation. HAADF-STEM has proven to be a quite effective tool for analyzing catalytic nanomaterials [9-13] and it has been used extensively in this project for the structural characterization of metallic NPs. In this dissertation the HAADF-STEM is used to obtain 3-D information of individual NPs. With proper calibration of the HAADF-STEM detector a detailed method has been presented to obtain the data on individual thicknesses and volumes of NPs as well as statistically relevant data on a large number of NPs. High-resolution TEM and tilt series imaging techniques have been used to gain additional knowledge about the structure of NPs to understand the processing parameters for controlling the Ag/EMPS system [14].

Previous research has already shown that quantitative information can be extracted from Z contrast micrographs in HAADF-STEM mode [15-24]. One aspect of the present work is to study the temperature dependence of the HAADF-STEM intensity. In the HAADF mode electrons undergo inelastic scattering which contributes to absorption of electrons inside the materials [25, 26]. The inelastic scattering phenomena and its dominance in wedge shaped TEM samples have been studied in this dissertation. While the classical multislice method or the Bloch wave approach are used for simulations of thin samples, these methods fail to generate accurate parameters for thick TEM samples as shown in this work. Certain limitations of work done by researchers previously are discussed in this dissertation. Modifications of the multislice method (for TEM simulations) are introduced to provide a procedure to simulate the behavior of the HAADF-STEM signal in thick sample and in parts of wedge-shaped samples. Absorptive parameters for several elements in the periodic table are determined from simulations using python programming. Additionally, a ballistic model to simulate the atomic number contrast at the interface of two materials in HAADF-STEM is presented in the last part of this dissertation. Results of these simulations using python are compared with experimental data.

1.1 Ag- Electroless Metallization

SU-8 is an important material for creating high-aspect-ratio microstructures [27, 28]. One reason for studying silvering is that bulk Ag has the highest electrical conductivity of all metals. The main goal of this study of Ag/EMPS is to understand the relationship between the deposition conditions and the morphology of the NPs. Gold and silver nanoparticles deposited on SU-8 polymer samples

provided by Prof. Stephen Kuebler's group in the Chemistry Department at UCF were used for analysis.

1.2 Sample Preparation

Silvering of polymeric surfaces involves a series of steps as follows:

a) cleaning of glass substrates;

b) crosslinking SU-8 films onto cleaned glass substrates;

c) functionalization of SU-8 polymer;

d) treating functionalized polymeric samples with a $HAuCl_4$ solution;

e) reduction to form Au nanoparticles using different reduction agents;

f) electroless deposition of silver.

Different methods of silvering have been tested and analyzed with TEM as described in the following paragraphs.

1.3 Polymer Cross-Linking and Reduction by $NaBH_4$

This section is in part based on the following publication:

- A. Dutta, C. J. Clukay, C. N. Grabill, D. J. Freppon, A. Bhattacharya, S. M. Kuebler and H. Heinrich, "Nanoscale characterization of gold nanoparticles created by in situ reduction at a polymeric surface", *Journal of Microscopy,* vol. 251, pp. 27-34, 2013.

Square 25 mm × 25 mm glass substrates were cleaned by immersion in aqueous 1.0 M KOH (Fisher, Hampton, NH, U.S.A.: CAS# 1310-58-3) for 1 h, rinsing with copious deionized water, and drying in an oven at 100°C. Cross-linked SU-8 films were prepared by spin coating SU-8 2035

resin (MicroChem, Newton, MA, U.S.A.) onto cleaned substrates. Substrates were cured by baking to remove the solvent at 65°C for 3 min followed by 95°C for 6 min. The substrates where then irradiated for 3 min using a broadband UV source (Loctite, Germany: ZETA 7411-5, 400 W metal halide source, 315–400 nm) with a longpass filter PL-360LP (Omega Optical, Brattleboro, VT, U.S.A.) having a cut-off wavelength of 360 nm, before baking exposures for 60 s at 65°C, 15 min at 95°C and 60 s at 65°C. The cross-linked polymeric films were functionalized with ethylene diamine [29], tetraethylenepentamine (TEPA) or N-aminoethylenepeparazine (AEP). Functionalization with ethylene diamine was achieved by immersing the cross-linked polymer film into a 20% 1, 2-diaminoethane (Acros, Belgium) (CAS# 107-15-3) solution in ethanol for 60 min, rinsing with copious ethanol, followed by water. Then the films were dried by standing in air. The amine functionalized polymeric samples were treated with an aqueous solution of 5.3×10^{-4} M $HAuCl_4$ (Acros, Hampton, NH, U.S.A.: CAS# 16961-25-4) for 30 min and rinsed with copious deionized water. For reduction three different procedures were followed. Some samples were immersed in 0.1 M aqueous $NaBH_4$ (Fisher, Hampton, NH, U.S.A.: CAS# 16940-66-2) for 60 s, rinsed with copious deionized water, and dried by standing in air [30-32]. Reduction by citrate was accomplished by immersing samples for 8 h in aqueous 1% (w/v) sodium citrate ($Na_3C_6H_5O_7$, Fisher: CAS# 6132-04-3) [32] . Reduction with hydroquinone was achieved by immersing samples in aqueous 0.1 M hydroquinone (Acros, HOC_6H_4OH, CAS# 123-31-9) for 1 h [33]. After reduction, samples were rinsed with copious water and allowed to dry by standing in air.

1.4 Silver Electroless Deposition

The silvering media are based on a formulation reported by Danscher and co-workers [33]. A citrate or lactate buffer (pH = 3.8) was prepared consisting of 1.5 M citric acid and 0.5 M trisodium citrate or 1.32 mL 85% lactic acid and 3.1 mL NaOH, both of which are then diluted to 7.5 mL. Aqueous silver lactate solutions having concentrations of 5 mM, or 33 mM were prepared by dissolving the parent salt in deionized water.

Hydroquinone was dissolved in deionized water to give a 0.58 M solution. A reductant solution was prepared by combining 7.5 mL of citrate buffer, 11.25 mL of hydroquinone solution, and 45 mL of deionized water.

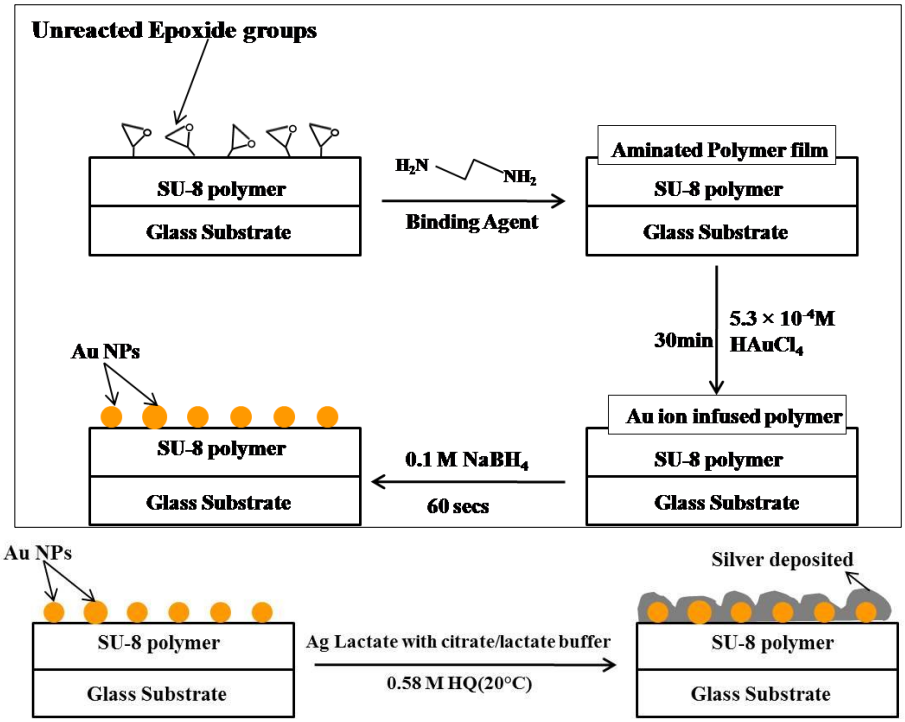

Figure 1 The schematic of the electroless deposition process

The reductant solution and 11.25 mL of the silver lactate/citrate solution were then equilibrated at (20 ± 1) ℃ and rapidly combined immediately prior to use. Baths formulated in this was had a final Ag^+ concentration of 5.6 mM, or 33 mM.

The Au-NP functionalized polymeric films were silvered by immersing the sample into a freshly prepared electroless silvering bath for a fixed period of time while continuously stirring. The silvering bath was maintained throughout at a constant temperature of (20±1) °C. After silvering, the sample was extracted from the bath, rinsed with deionized water, and allowed to dry in air. Figure 1 summarizes the steps involved in electroless deposition.

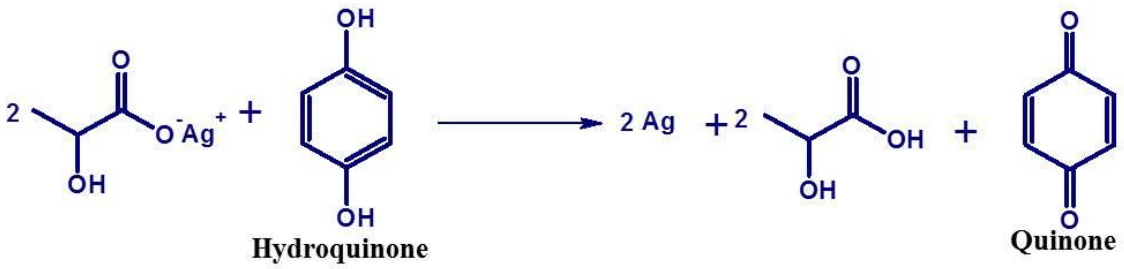

Figure 2 The reaction mechanism for deposition of silver

The reaction of silver lactate in a citrate or lactate buffer in the presence of hydroquinone is shown in Figure 2 above. Silver ions are reduced to form metallic silver while hydroquinone is oxidized to quinone. Prepared silver samples are shown in Figure 3 below.

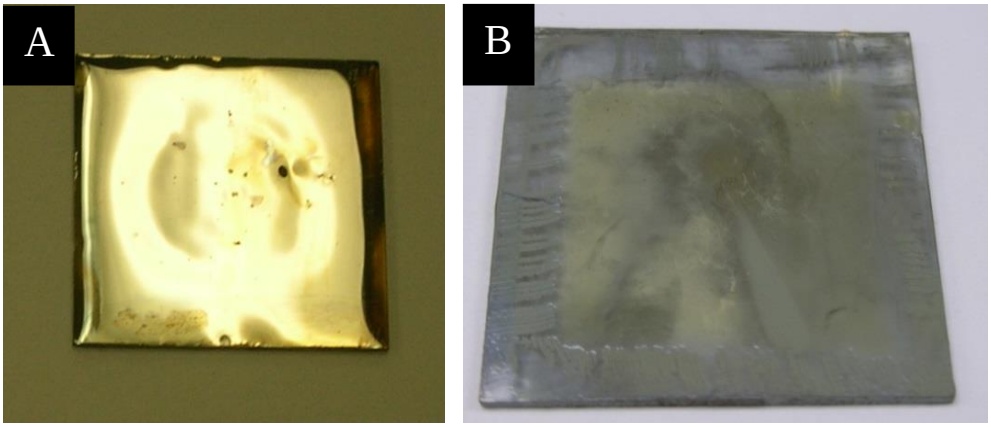

Figure 3 Silver films that undergo typical treatment, as described above are highly reflective and have a silver layer thickness of 450-500 nm. (B) Picture of silver deposition with no catalytic gold nanoparticles. Note that surfaces are not reflective [1].

1.5 Sample Preparation for Transmission Electron Microscopy (TEM)

Two types of TEM samples were prepared with the gold and silver nanoparticles deposited on SU-8 polymeric samples.

Cross sections - For Focused Ion Beam (FIB) cross sections the samples are placed inside a vacuum evaporator (JEOL JEE 4X, Japan) for coating with carbon. This is done to distinguish the nanoparticles on the surface of the polymer from the platinum layer on the top of the sample which is deposited during the FIB process. Inside the bell jar of the evaporator there are two electrodes with a manual shutter mechanism serving the second electrode. Vacuum is maintained in the bell jar with the help of a rotary pump and a diffusion pump as shown in the Figure 4 (Left) below.

Two carbon rods are attached to one of the electrodes so that they touch each other head on and the sample is placed just below the rods as shown in Figure 4 (Right). At a pressure of (1-3) x 10^{-4} Pa the filament is slowly heated up with increasing power and carbon coating is carried out on the samples. A typical good carbon coating is around 50-70 nm thick which improves the contrast for cross-sectional samples containing nanoparticles deposited on the surface of the polymer.

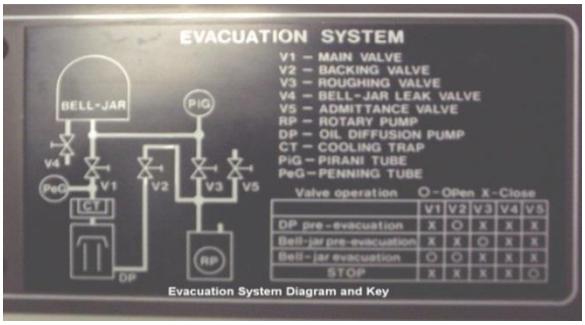

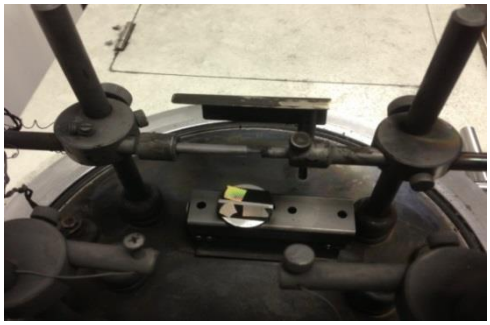

Figure 4 (Left)The evacuation system of the carbon coater used for carbon coating on the sample surface before FIB cut. (Right) Shows the two electrodes where sample is placed under one electrode ready for carbon coating.

To improve conductivity and contrast inside the FIB, the C-coated samples were additionally coated with an Au-Pd alloy for 3–4 min in a sputter coater (Emitech K550, UK) at $1x10^{-1}$ mbar pressure and with a deposition current of 20 mA. The sputter coater uses a 60 mm diameter and 0.1 mm thick magnetron target assembly giving fine grains without the need to cool the specimen.

Plan-view – Portions of the Au & Ag deposited film on glass substrate are scraped off with tweezers and placed directly on the Cu grid. This is done carefully so as not to scrape off too much polymer, which produces high-background (noisy) signals during imaging under the TEM. Plan-

view samples are used for thickness measurements of gold and silver nanoparticles on SU-8 polymer.

1.6 Focused Ion Beam (FIB) Technique

A Focused Ion Beam (FEI, FIB 200) system shown in Figure 5 operating at 30 kV was used to prepare cross-sectional TEM samples of gold and silver. The FIB system can be operated at low-beam currents for imaging or high-beam currents for site-specific sputtering or milling. Currents as low as 50 pA or 100 pA are used to position the sample and check the necessary alignments. The FIB stage is tilted 45° and the eucentric height is adjusted before saving the final position of the sample. Specific positions are considered for the FIB cuts after proper focusing of the sample at lower beam currents. A 1 μm thick platinum layer is deposited on the sample surface using a 100 pA beam current on a typical rectangular area of 15 μm (length) ×1 μm (width) to protect the interior of the FIB cross section from gallium ion implantation with the help of the Pt deposition needle within the instrument as shown in Figure 6 (A).

Figure 5 FEI FIB 200 system used at the MCF in the University of Central Florida.

This needle contains an organometallic gas which decomposes to deposit Pt in the Ga ion beam. After platinum deposition, milling is carried out on the desired rectangular area with precise control by using large ion beam sizes (3000 pA and 1000 pA) initially and then lowering the beam size (Figure 6 (B)) for the final high quality cut. For FIB processing the sample is tilted to 45° and the bottom and side cuts are made as shown in the Figure 6 (C) below. Currents as low as 50 pA are used for the final thinning of the sample to prevent back deposition of gallium ions and to limit the thickness of the amorphous (radiation damaged) layer forming at the surfaces of the FIB cross section [34, 35] as shown in Figure 6 (D). Using an ion beam of 50 pA one side of the cross sectional sample is cut off fully at 0° tilt and the other side is milled half way to let the sample hang inside the FIB trench (Figure 6 (E, F)). The typical dimensions of the final sample for *ex situ* lift-out (EXLO) are 15 μm (length) x 4 μm (height) x 50 nm (thickness).

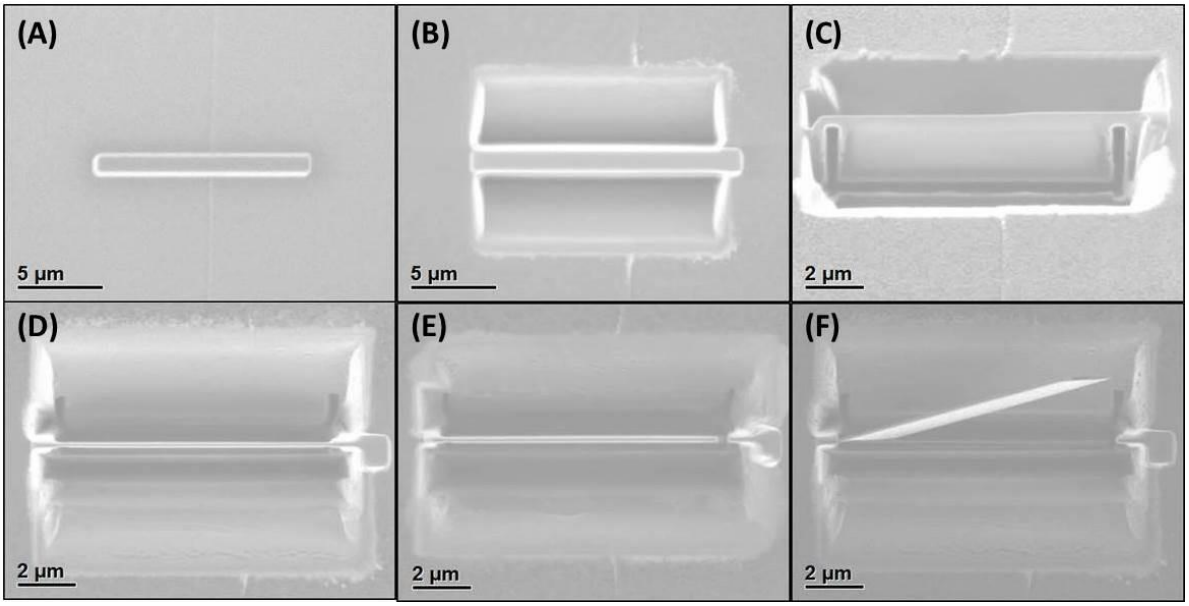

Figure 6 (A-F) FIB steps for cross sectional sample preparation.

There are two different types of lift out techniques available for FIB processing: *ex situ* lift-out (EXLO) and *in situ* lift-out (INLO). In this project the EXLO technique has been exclusively used [36-39]. The ex-situ foil extraction is faster, more versatile and offers high yields at lower cost in comparison to the in-situ technique [40]. A Mitutoyo (Japan) VM Zoom 40 optical microscope equipped with hydraulic micromanipulators (Figure 7(Left)) was used for EXLO from the bulk and for placement of the TEM sample on a holey carbon-coated Cu grid [41]. The microscope is connected to a TV screen which is used to locate the FIB cross-sectional cut. The prepared cross-sectional sample attaches to the micromanipulator needle shown in Figure 7(Right) via electrostatic forces and can easily be transferred onto the TEM grid.

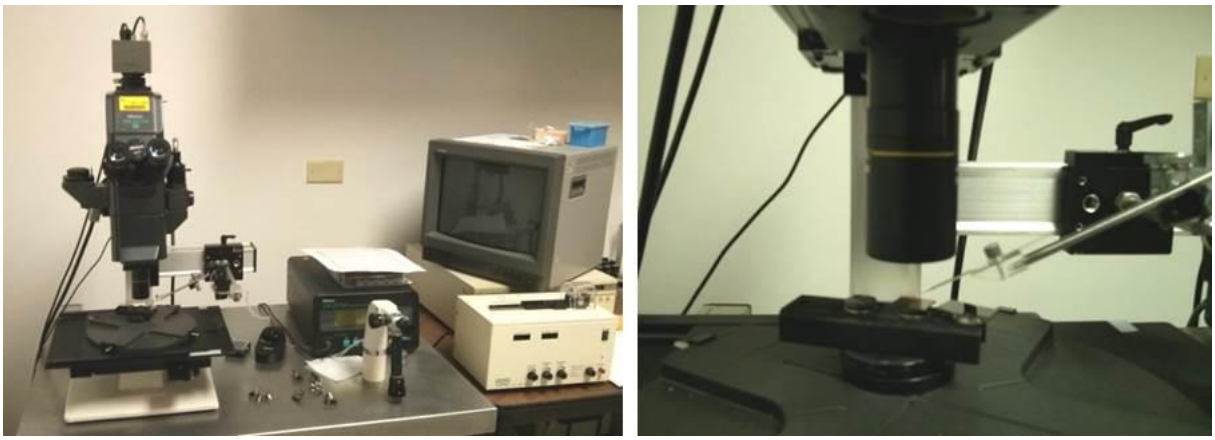

Figure 7 (Left) Optical microscope equipped with hydraulic manipulators connected to camera. (Right)Micromanipulator needle for sample lift out.

CHAPTER 2: METHODOLOGY

2.1 Focused Ion Beam

As the FIB technique has been used extensively for preparing cross sectional TEM samples including wedge shaped samples, it is worth looking at some specific properties of the FEI FIB 200 system used here and shown in Figure. 5. It consists of a vacuum system and chambers, detectors, gas delivery system, ion column, a liquid metal ion source, gas inlets, an in-situ lift out needle and a stage capable of five-axis motions.

There are two types of Liquid Metal Ion Source (LMIS) used in the FIB [42]. The conical emitter contains the source material gallium which liquefies on heating. Gallium is used as ion source because of its low melting point, low vapor pressure, very high brightness and long life time for an FIB system [42].

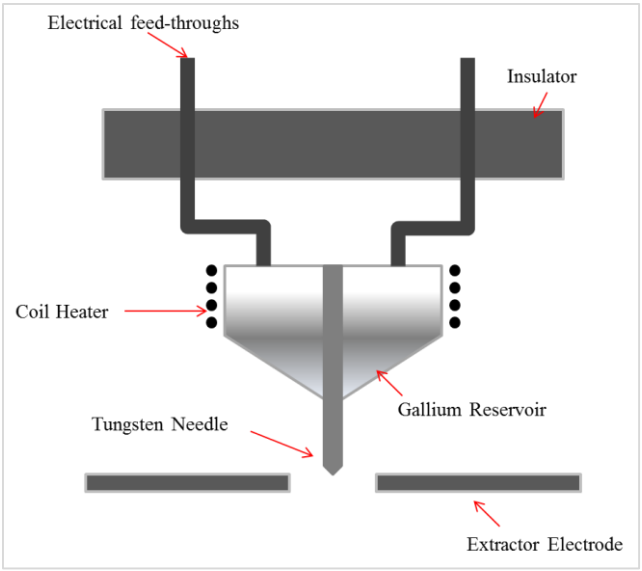

Figure 8 Schematic of the LMIS inside the FIB [42].

A tungsten needle remains in contact with a gallium reservoir as shown in Figure 8. An extractor voltage of around 10 kV is used to generate a high electric field of the order 10^{10} V/m at the tip. The gallium atoms in the reservoir get ionized and a drop of gallium gets ready to be emitted from the needle. Varying ion probe currents of 10 pA to 20,000 nA can be used to remove material from specific locations to prepare a cross sectional sample. A 30 kV negative bias is applied by which the Ga^{+} ions leave the LMIS and accelerate towards the specimen.

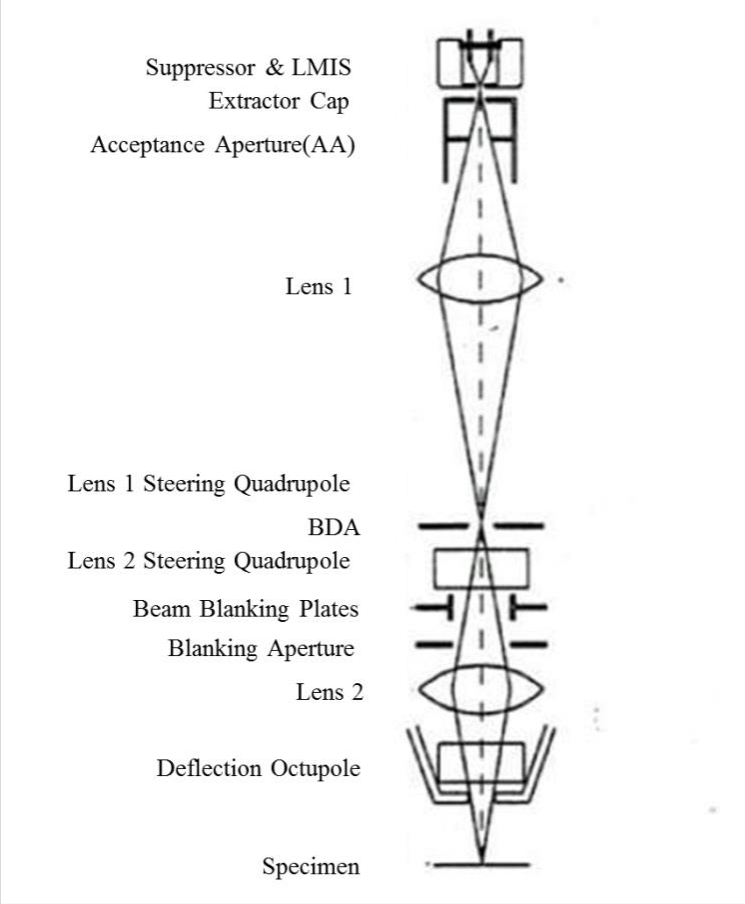

Figure 9 Schematic of the FEI FIB 200 [43].

The lens system in the FIB consists of two electrostatic lenses, a steering quadrupole and an octupole deflector which focus the beam and scan on the specimen [43] (Figure 9). The Ga^+ ions scan the surface and penetrate into the surface at different depths in different materials. A high number of secondary electrons is produced so the FIB can be used in secondary electron imaging mode. So the image is created by secondary electron emission from microstructural features at the sample surface. The interaction volume in FIB is less than that for an SEM and so the image quality of the FIB is not the same as for an SEM. The current of secondary electrons is measured by the secondary electron detector. Figure 10 schematically shows the secondary electron and ion emission during the FIB milling process [44].

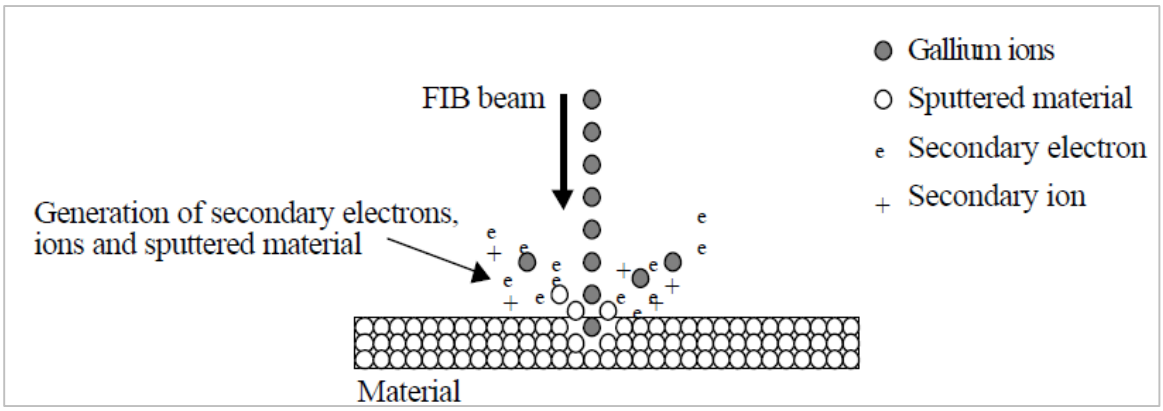

Figure 10 Schematic of the electron and ion emission during FIB milling process [44].

2.2 Bright Field Transmission Electron Microscopy

Transmission electron microscopes are used in materials science to obtain crystallographic and other structural and chemical information of thin sample. Crystallographic information is contained in the transmitted electrons. TEM is a powerful tool which is used for electron diffraction

at a localized level (a few nm to several microns) including convergent-beam electron diffraction (CBED). The diffraction pattern is to a large extent formed by elastically scattered electrons according to Bragg's law and provide structural information of a crystalline sample [17].

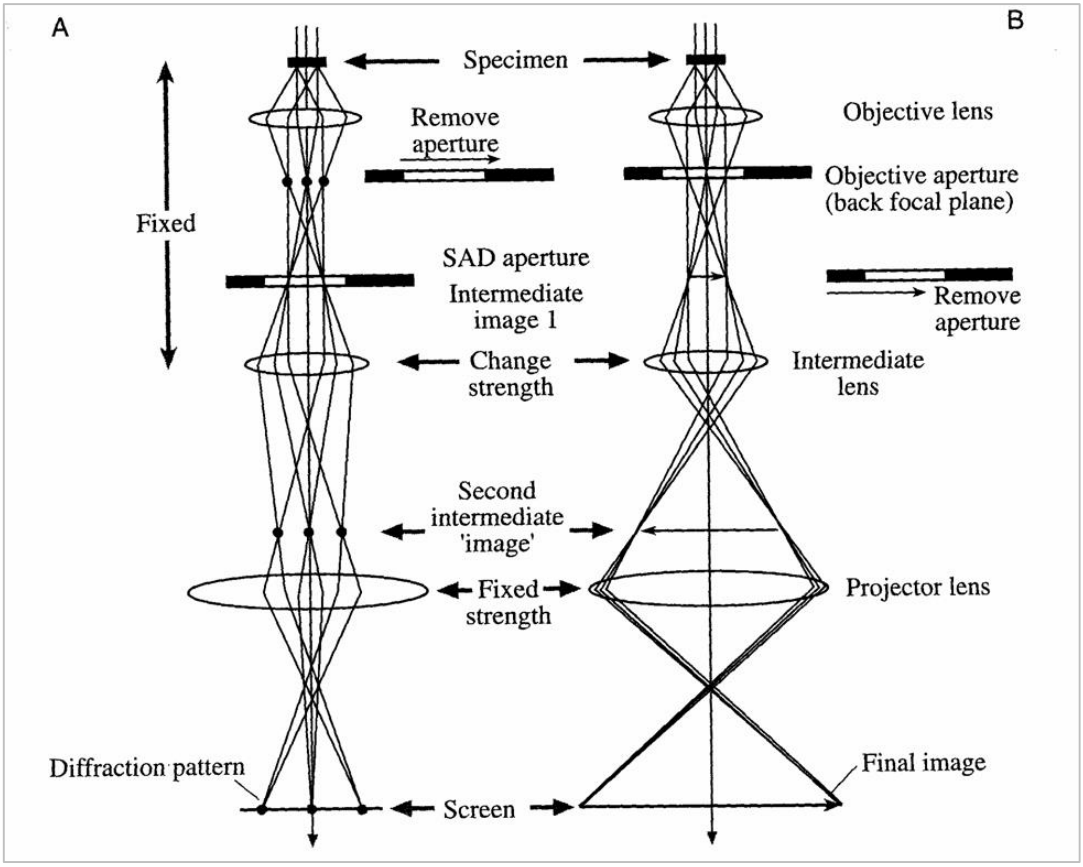

Figure 11 Schematic of the optical system inside the TEM. (A) Projection of the diffraction pattern on the viewing screen. (B) Formation of the magnified image on the viewing screen [17].

In the transmission electron microscope the electron gun emits electrons through thermal emission and/or field emission. When the electrons pass through an electric field introduced by the voltage difference of anode and cathode (300 kV) they get accelerated and pass through the optical system

of the TEM which consists of electromagnetic lenses. An electron probe is formed with a small diameter at the sample. Electrons passing through the sample may suffer elastic and inelastic scattering and get detected by various detectors. An image can also be formed on the fluorescent viewing screen (Figure 11).

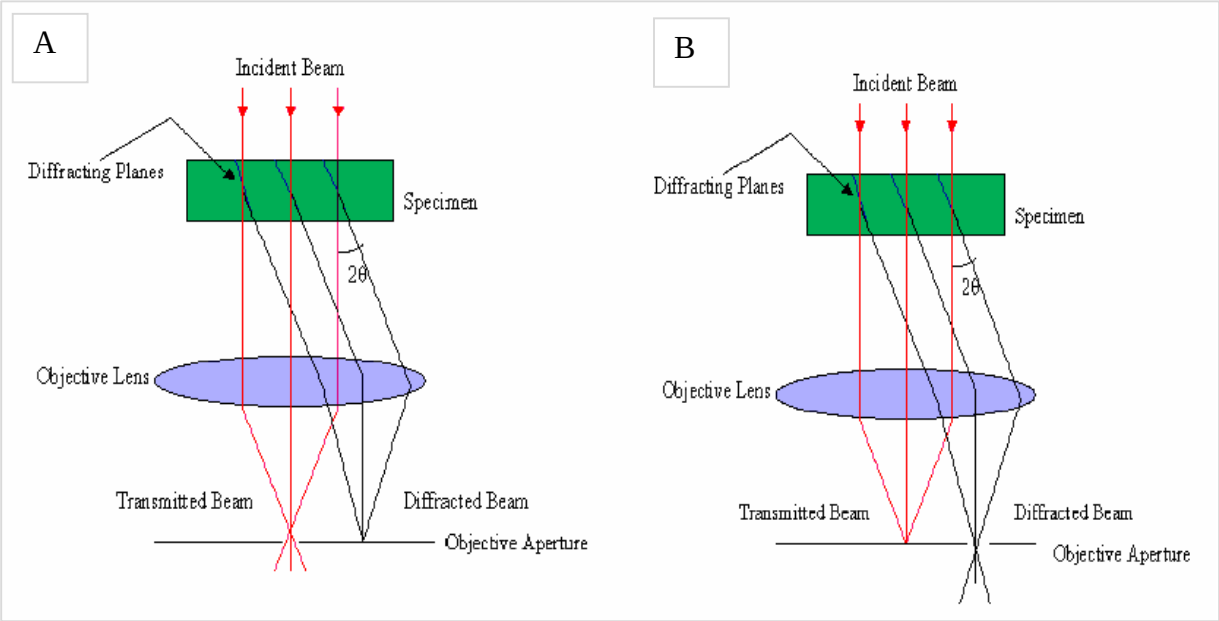

Figure 12 (A) Bright Field imaging technique. (B) Dark Field imaging technique using a scattered beam [17].

The interference of the transmitted and the diffracted rays leads to the formation of real-space images with very little contrast in the TEM. With only the transmitted electrons we can form a Bright Field (BF) image (Figure 12A) when the objective diaphragm is placed to let only the undiffracted through the aperture. When positioning the objective aperture in such a position in the back focal plane so as to select only the electrons diffracted into a certain angular range a Dark Field (DF) image is formed (Figure 12B). Usually, however, the incident electron beam is tilted in a way to let diffracted electrons through the objective aperture while it remains centered around

the optical axis of the electron microscope. This reduces aberration lens errors for off-axis electron. High-Resolution TEM (HR-TEM) images represent the intensity modulations which arise from the superposition of the exit plane electron wave after passing through the sample and the phase shift caused from the spherical aberration and the defocus of the objective lens. HR-TEM images are often difficult to interpret because they are very sensitive to changes in the focus of the objective lens. This makes analysis of defects and grain boundaries difficult for HR-TEM.

2.3 Scanning Transmission Electron Microscopy (STEM)

In the STEM mode a fine highly focused beam of electrons is scanned over a specimen area. The transmitted electrons are either scattered elastically, inelastically or remain unscattered. The difference between TEM and STEM image formation is related to the path of the electrons, as it is essentially inverted as shown in the Figure 13 below.

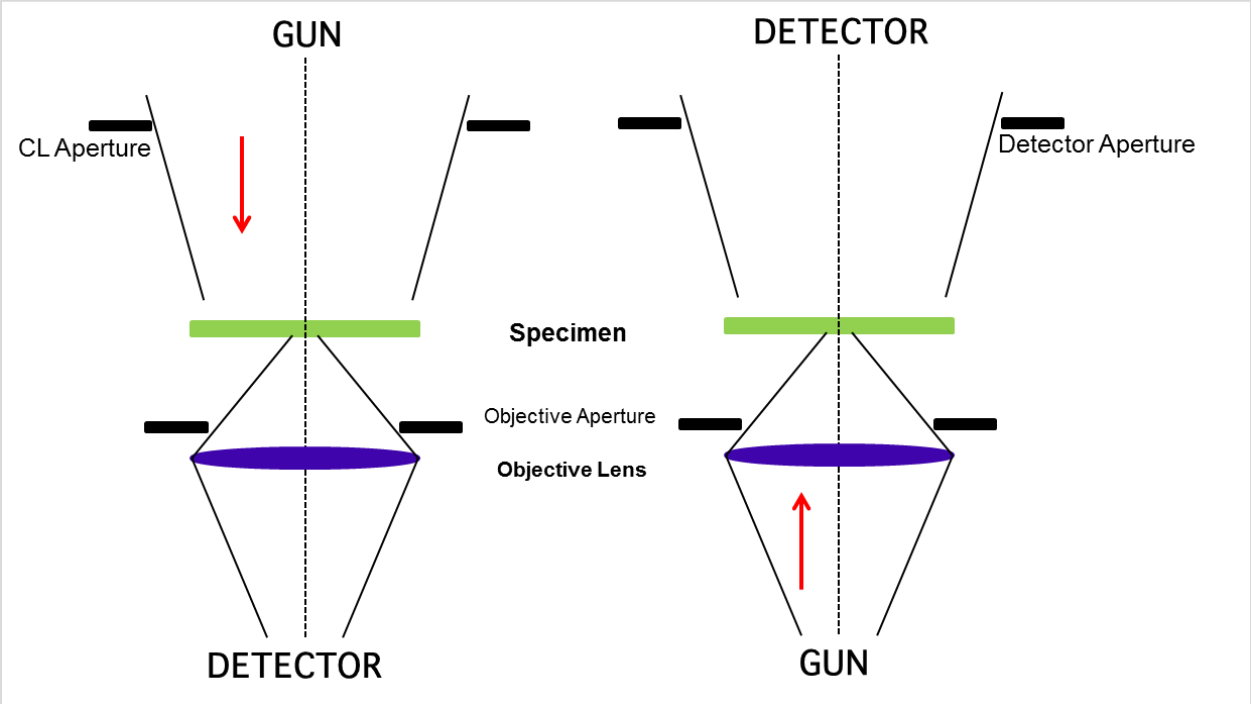

Figure 13 Equivalence of TEM (left) and STEM (right)

Physically, both TEM and STEM modes can be realized however in a transmission electron microscope without exchanging the electron gun by utilizing the lower pole piece of the objective lens for the image formation in the TEM mode and the upper pole piece of the objective lens for beam formation in the STEM mode.

With larger detectors the STEM mode is also used to collect electrons inelastically scattered at larger angles providing additional chemical information about the sample. Another benefit of using STEM is that much thicker samples can be imaged by this technique. The electron loses energy as it travels through the specimen. In the TEM mode the objective lens (below the sample) causes a loss of contrast and resolution by focusing electrons of different energies at different focal points (chromatic aberration). Such effects are absent in STEM, so thicker samples can be evaluated

without any loss of contrast in STEM micrographs. Delocalization effects present in TEM micrographs are mostly absent in STEM, so image interpretation is easier. However, dark-field STEM images are typically noisy (due to only scattered electrons contributing to the image) and require longer acquisition times compared to HR-TEM.

2.4 High Angle Annular Dark Field Scanning Transmission Electron Microscopy

Other than the normal bright-field and dark-field imaging modes some transmission electron microscope systems also have the option of the scanning mode. In scanning transmission electron microscopy (STEM) signals are collected from small areas where the electron beam is focused on the sample. In STEM three different detectors can be used: a bright field detector (BF), a dark field (DF) detector, and a high-angle annular dark field (HAADF) detector. All three detectors are located in the diffraction plane of the sample. In the TECNAI F30 system used in this project, the HAADF detector is retractable above the fluorescent screen. The BF and DF detectors are off-axis below the fluorescent screen. When using the BF or DF detector (they can also be used together) the fluorescent screen is lifted and the operator has to deflect the transmitted electron beam onto the BF detector in the projector system of the electron microscope. An HAADF detector collects electrons which are scattered at high angles unlike the normal bright field and dark field detectors which collect Bragg-scattered electrons at low angles. Howie in 1979 proposed a high-angle annular dark field (HAADF) detector which mostly measures the signal from electrons which are incoherently scattered at high angles ($2\Theta > 50$ mrad corresponding to $>3°$). Due to the incoherent nature of the imaging process with the HAADF detector, the contrast of HAADF-STEM images depends on the atomic number of the element and on the sample thickness. This technique

therefore often referred to as Z-contrast imaging. If the electron probe is small enough (below 0.2 nm diameter) it is possible to obtain information on the position of the atomic columns (and in some cases even chemical information of individual atomic columns [45]) in a crystal with Angstrom resolution. If the sample is properly oriented parallel to atomic columns in a crystal the atomic columns appear brighter than the spacing between atomic columns. The main advantage of the HAADF-STEM technique over conventional HR-TEM is that Z-contrast images create a strong bright contrast of atomic columns of elements of higher atomic number, while atomic columns containing atoms of lower atomic number produce a less bright contrast. Thus atomic columns of gold (atomic number 79) atoms will appear brighter than columns of titanium (atomic number 22) atoms if present together. HAADF-STEM micrographs are also strongly thickness dependent, thus areas of higher thicknesses appear brighter than thin sample parts. In this case, the higher intensity doesn't necessarily mean a higher atomic number. Additional contrast changes from crystal tilts and defects need to be considered [46, 47]. In this work the main emphasis is on samples not oriented parallel to any specific crystallographic orientation. In this case atomic column resolution is not achieved and electron probe diameters of more than a few angstroms yield comparable results as small probe sizes. For larger electron probes (larger than the projected spacing between nearest-neighbor atomic columns) we therefore expect no contrast difference between on-column probe position and off-column position. Only atomic numbers, atomic densities, and sample thickness determine the HAADF-STEM contrast. Orientation effects are suppressed and are often neglected in first-order approximation. In this case the relation between the intensity of the signal acquired by a HAADF detector, the thickness (t) of the specimen and the atomic number (Z) is given by:

$$I \propto tZ^{\alpha} I_{\text{incident}} \qquad (2.1)$$

where α is a fitting parameter and 1< α <2[17]. Equation 2.1 is a first approximation of the HAADF-STEM intensity and valid only for very thin samples where multiple scattering is negligible. Different atomic densities of different materials are also not considered in this equation. For very thick samples the final intensity approaches the intensity of the incident beam due to multiple scattering events and additional corrections for absorption are necessary.

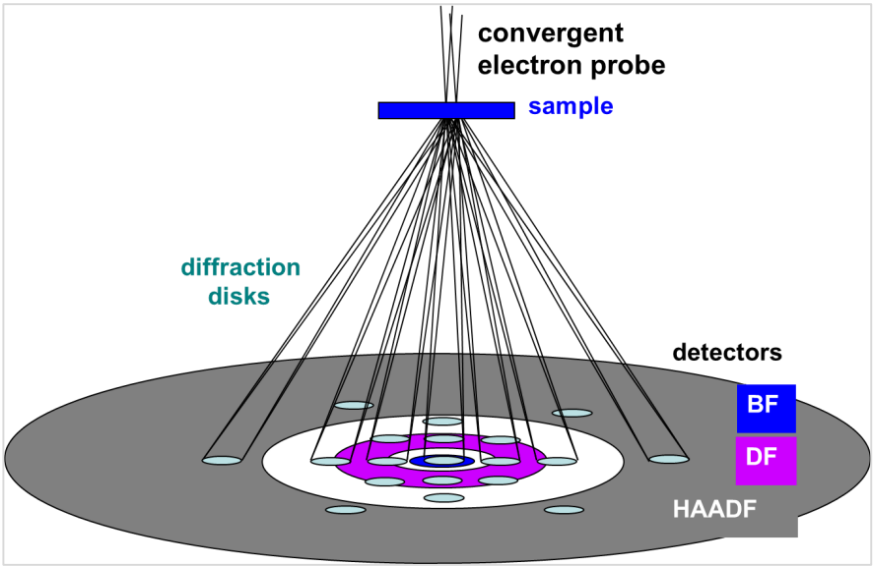

Figure 14 Schematic of a HAADF-STEM detector

A schematic of the HAADF-STEM detector is shown in the Figure 14. The convergent electron probe determines the spatial resolution as the focused electron beam moves across the specimen generating varying signals depending on the crystal structure, composition and orientation of crystallographic planes.

The quantitative measurement of the thickness and volume of NPs from images of plan-view samples requires the intensity calibration of the HAADF detector intensity. To accomplish the contrast calibration both the HAADF detector intensity and the corresponding CCD camera intensity were measured in the direct imaging mode. A contrast/brightness setting of 12.5% and 46.875% and a camera length of 80 mm was consistently used The beam intensities were acquired for different spot sizes, gun lenses and condenser aperture sizes keeping the extraction voltage in the electron microscope constant. The HAADF detector shows some variability (about 10%) of its sensitivity depending on where the electron beam hits the detector. Figure 15(B) shows an image of the HAADF detector.

The background signal in the dark areas of the insert shows variations of less than 3%. A linear interpolation of the background signal over the bright detector area was used. The background was subtracted and the intensities were averaged ($I_{\mathrm{HAADF,avg}}$) over the HAADF detector for calibration of different incident electron beam probes (Figure 15(A)).

The HAADF detector intensity scales with the linear CCD signal and can be best fitted as the following:

$$I_{\mathrm{HAADF,avg}} = A I_{\mathrm{CCD}}^{B} + I_{\mathrm{Background}} \qquad (2.2)$$

where $I_{HAADF,avg}$ is the intensity of the HAADF detector, I_{CCD} is the intensity (per second) of the CCD detector, A and *B* are constants [17, 48].

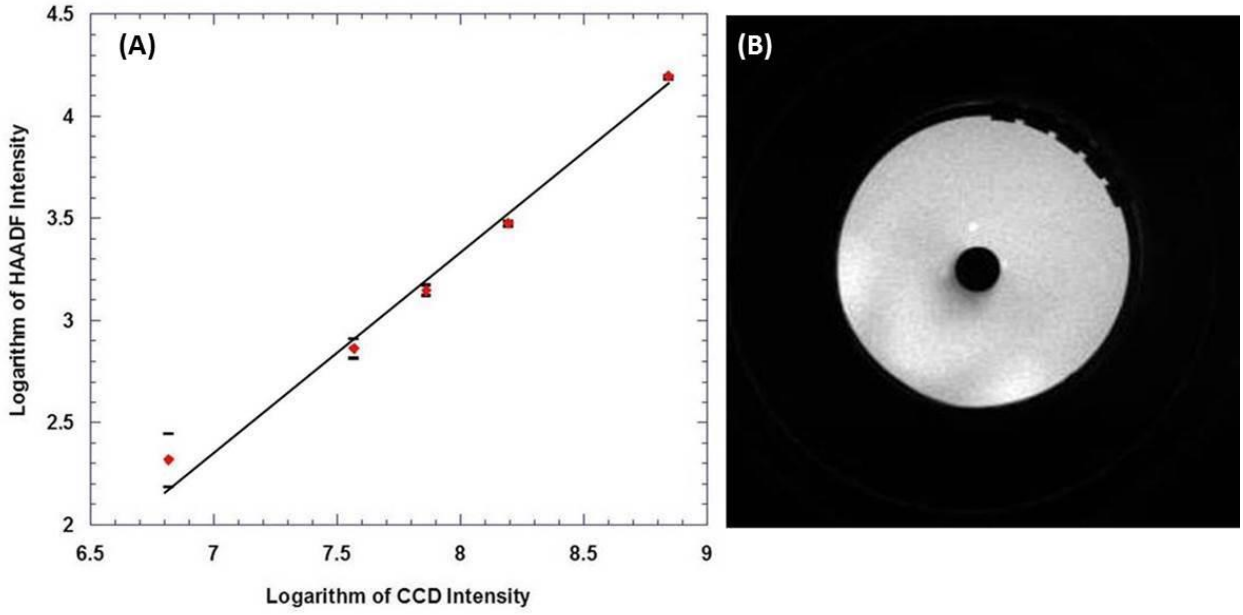

Figure 15 (A) Plot of the intensity of the HAADF detector versus CCD camera. (B) The HAADF-STEM detector image in imaging mode shows the sensitvity of the detector in different angular ranges. The dark hole in the detector corresponds to the low angular range where electrons don't hit the detector. The detecor itself shows some variation in sensitivity as can be seen from the different brightnesses of the detector in different areas.

$$\log I_{\mathrm{HAADF,avg}} = B \log I_{\mathrm{CCD}} + \log A \qquad (2.3)$$

The following values were obtained: slope B = 1.01(±0.014), A = (8.0±0.16)*10^{-6} and the correlation coefficient R = 0.99947.

$$I_{\mathrm{HAADF,avg}} = (8.0 \pm 0.16) * 10^{-6} I_{\mathrm{CCD}}^{1.01(\pm 0.014)} \quad (2.4)$$

2.5 Energy Dispersive X-ray Spectroscopy (EDS)

In TEM electrons passing through the sample interact with inner-shell electrons. The emission of inner-shell electrons thus produces vacant electron states in the inner electron shell of atoms. Higher energy electrons fill up these vacant states which results in X-ray emission (and Auger electron emission) with energies characteristic for specific elements. The emitted X-rays are then detected with an energy dispersive detector. EDS is used for detection of heavier elements as X-rays from lighter elements tend to get absorbed more (and as lighter elements have a higher probability of emission of Auger electrons than emission of X-rays). The EDS detector is always situated above the specimen to minimize the background signal (e.g., from bremsstrahlung X-rays generated as the electron beam passes through the sample) in the spectrum. A typical X-ray detector consists of Si (Li) or Ge with a Be window. The sample is tilted approximately 15° towards the detector to minimize the absorption of low-energy X-rays. An X-ray spectrum is collected where different X-ray energies can be correlated to different elements. Usually, EDS spectra are obtained either from point measurements, line scans across the sample or as area scans/maps where the electron probe is sequentially positioned on different points to form distribution maps of elements. The schematic of the EDS detector geometry is shown in Figure 16.

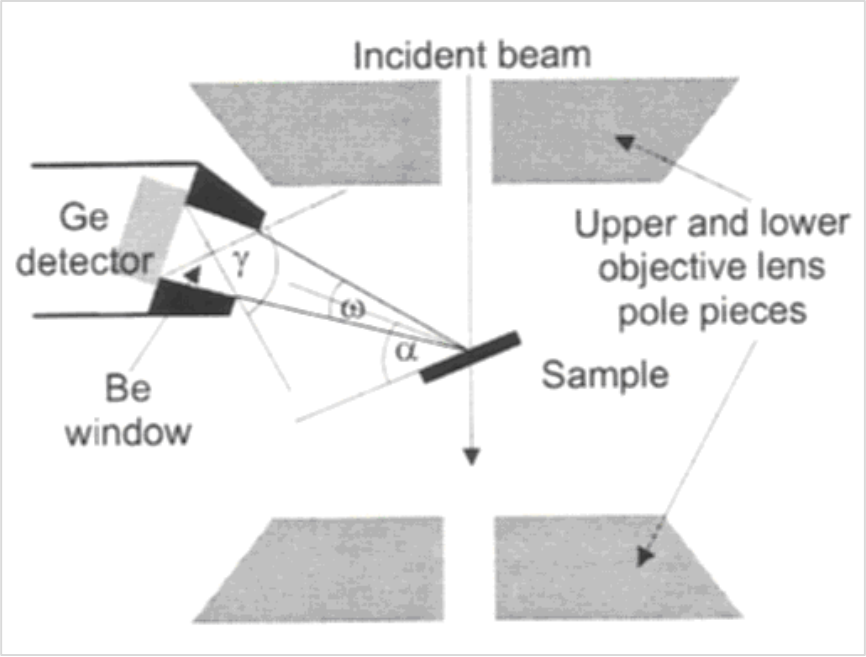

Figure 16 Schematic of the EDS detector geometry.

CHAPTER 3: TEM STUDIES

3.1 Morphology of Au NPs from BF-imaging

Direct evidence concerning the morphology, size and density comes from the transmission electron microscopy studies of colloidal Au bound to SU-8 polymer on the TEM grids. Plan-view samples of Au NPs prepared by reduction of $NaBH_4$ reveal that the NPs are spherical in shape with a diameter in a range of 2-3 nm. They are evenly spaced with no agglomeration and no apparent faceting (Figure 17).

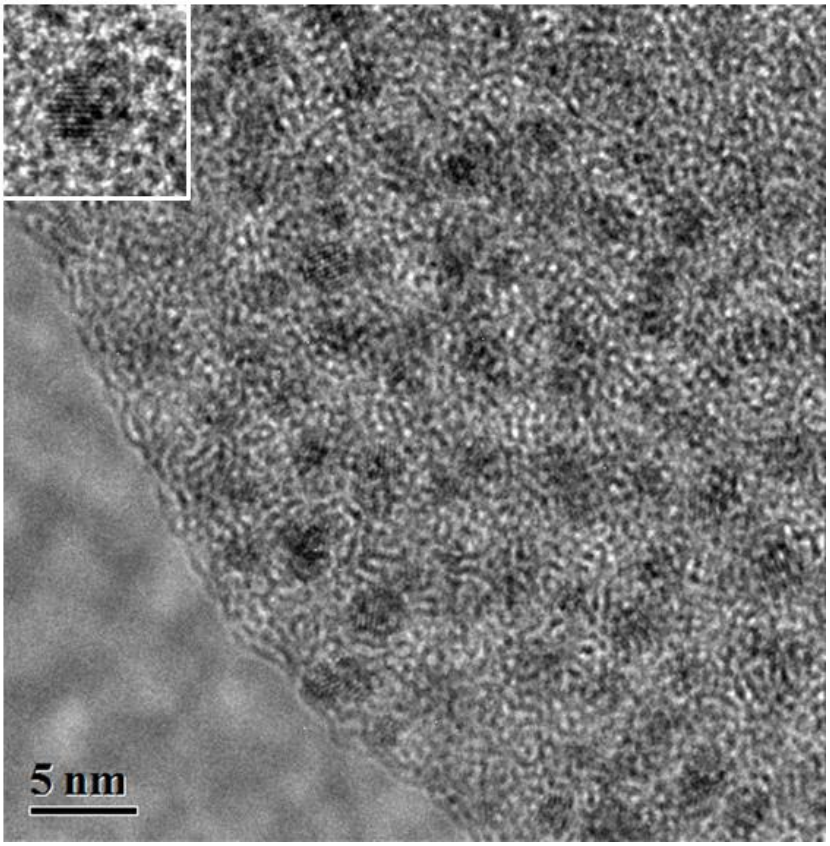

Figure 17 TEM plan view image of Au NPs evenly spaced on SU-8 polymer.

High-resolution TEM images reveal that the NPs are crystalline. The diffraction patterns confirm the F.C.C. structure (lattice plane spacing 4.07 Å) of gold. Figure 18(A), (B) and (C) shows the BF-TEM micrograph of Au NPs formed on SU-8 polymer using three different reducing agents of varying standard reduction potential.

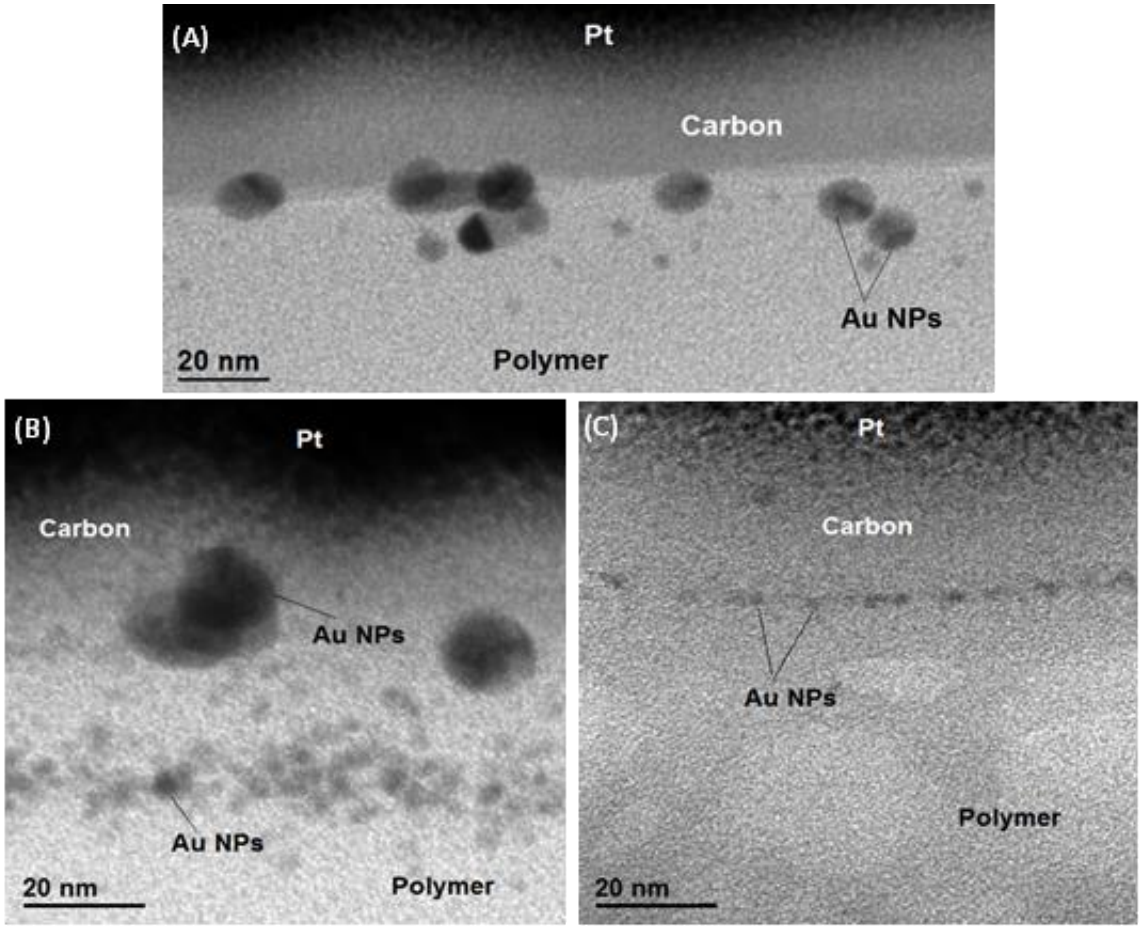

Figure 18 (A) Cross-sectional Bright Field (BF) TEM micrographs of Au NPs formed by reduction with hydroquinone (HQ). (B) Au NPs formed from reduction of Au^{3+}ions by sodium citrate. (C) $NaBH_4$ reduced Au NPs on the SU-8 polymer surface.

Cross-sectional TEM images reveal crystalline NPs with typical {111} and {200} lattice plane spacing. For hydroquinone-reduced gold, the Au NPs form a band on or near the surface of the polymer, with particle sizes in the (5-10) nm range, as shown in Figure 18(A). As hydroquinone is a bulky reducing agent, there is less penetration into the polymer matrix, so the NPs are mostly formed near the surface of the polymer confirming recent findings by *Taleb et al*. [49]. Figure 18(B) shows Au NPs that are (10-15) nm in diameter formed by citrate reduction of Au^{3+} ions. These Au NPs formed by citrate reduction are found on the surface as well as up to 20 nm below the surface of the polymer. Smaller nanoparticles of (3-4) nm average diameter are formed 20 nm inside the polymer matrix, whereas larger Au NPs of (12-15) nm average diameter are found only on the surface. Au NPs are formed on or near the surface of the polymer by reduction of gold ions by $NaBH_4$ as can be seen in Figure 18(C). The nanoparticles are spherical in shape and they are of range (2-5) nm in diameter with almost no faceting. Moreover, the Au NPs are aligned along a straight line (10-20) nm below the polymer surface. Sodium borohydride is a strong reducing agent which produces small Au NPs whereas hydroquinone, having a higher standard reduction potential, generates bigger nanoparticles. Moreover, hydroquinone, being a bulky molecule, fails to penetrate the polymer matrix to act upon the Au^{3+} ions that have adsorbed into the polymer matrix. Bright-field TEM images in Figure 18(A) and (B) suggests that when hydroquinone acts as reducing agent the Au NPs have smaller height (4-5 nm in diameter) than when formed by sodium citrate, in which case they are (10-15) nm in height. The measurement of the height confirms that the nanoparticles are spherical in shape and they are not faceted.

3.2 HAADF Measurements

Section 3.2 and 3.3 is partly based on the following publication:

- A. Dutta, C. J. Clukay, C. N. Grabill, D. J. Freppon, A. Bhattacharya, S. M. Kuebler and H. Heinrich, "Nanoscale characterization of gold nanoparticles created by in situ reduction at a polymeric surface", *Journal of Microscopy*, vol. 251, pp. 27-34, 2013

The HAADF technique has the advantage that the contrast is highly dependent on the atomic number of the material and not on the crystal orientation; it can provide structural and chemical information with atomic resolution as shown by [50, 51]. After the calibration of the detector signal to correctly account for non-linear effects, the fraction of electrons scattered onto the HAADF detector for each scan position in an experiment is obtained. Before and after the HAADF-STEM measurement for an Au sample, a STEM image of the detector (in imaging mode) is acquired. This measurement is done twice to ensure that the electron beam intensity did not change during the acquisition of HAADF-STEM images. Au NPs of diameter (50-60) nm were used to determine the fraction of scattered electrons per nm thickness of the gold sample. Among the nanoparticles viewed without sample tilt and two sample tilts of 45° and -42°, several showed no change in diameter indicating a nearly spherical shape. In addition the measured HAADF-STEM intensity of those selected nanoparticles did not change significantly for the three viewing directions. The measured diameter (49.5±0.2) nm and the corresponding volume ($V = 6.34 \times 10^4$ nm^3) of the selected nanoparticle shown in Figure 19 remains the same when the sample is tilted in the microscope holder in the positive and negative direction thus when the

sample is tilted in the microscope holder in the positive and negative direction thus confirming its spherical shape. In addition to HAADF-STEM micrographs BF-TEM images of the same nanoparticles were taken to confirm the measured diameters and shapes at the three same tilt angles. Summation of the intensities of each pixel ($\sum I$) over the whole nanoparticle gives us $(\frac{\sum I}{I_{HAADF,avg}})*(\frac{pixel\ area^2}{V})$ = 0.213%, representing the fraction of the HAADF signal intensity per nm of Au thickness relative to the HAADF intensity for the incident beam directly on the detector.

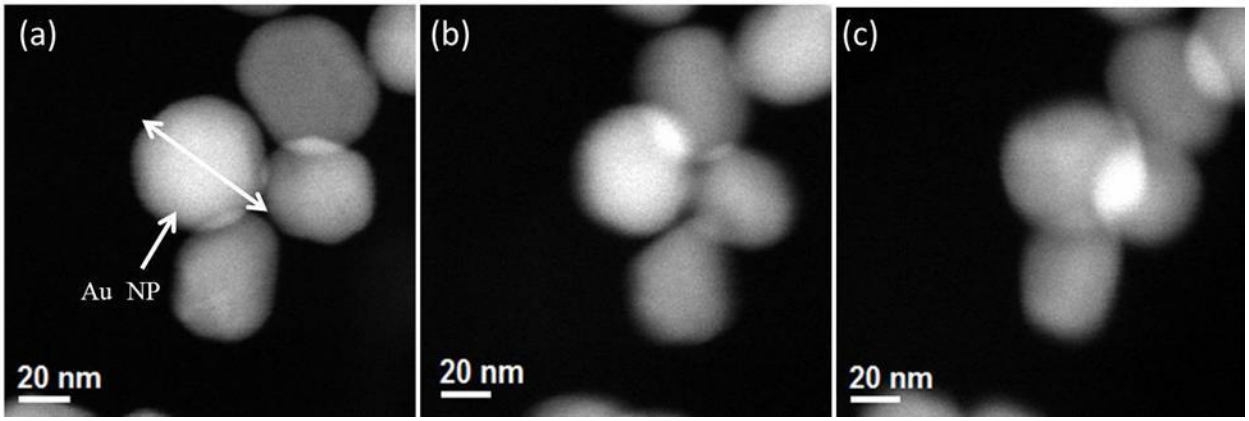

Figure 19 (a–c) STEM micrographs of Au NPs 50–60 nm in diameter at 0◦, 45◦ and −42◦ tilt of the TEM holder. The tilt axis is vertical and the particle.

Taking the average of several Au nanoparticle measurements this signal fraction is (0.207±0.010) %. After correcting for the non-linearity of the HAADF detector, the fraction of scattered electrons is 0.25% per nm of Au thickness with the above detector contrast and brightness settings. The local thickness of the selected nanoparticle shown in Figure 19 is calculated by $\left(\frac{\frac{Intensity}{pixel}}{I_{det,avg}}\right) * (\frac{1}{0.0021})$ at each point through the nanoparticles' center (grey curve in Figure. 20). Considering the selected

nanoparticle to be spherical in shape, the thickness is calculated shown in black curve in Figure 20. The overlapping of the two curves signifies the consistency of the method of thickness determination of nanoparticles talked about in this dissertation.

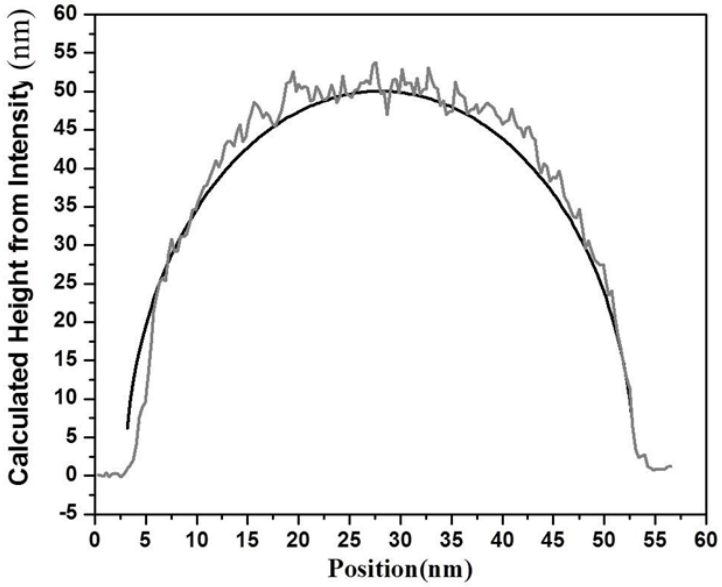

Figure 20 Height of the selected nanoparticle in Figure 19 from HAADF Intensity.

3.3 Quantitative Analysis of HAADF-STEM Images

Plan-view samples were studied in the STEM mode using the HAADF detector. Evaluation of the NP size, volume and distribution on the surface has been carried out in the past using HAADF images [52-55]. A representative plan-view HAADF-STEM image of an Au deposited sample from reduction by $NaBH_4$ is shown in Figure 21. The Au NPs, which can be seen as bright contrast features on the dark contrast SU-8 polymer, can be thought of as isolated particles deposited on the SU-8 polymer. An integration time of ten microseconds for each of the 2048x2048 pixels was

used to acquire an HAADF-STEM image. In the STEM mode with a HAADF detector, atomic number contrast was used to identify the nanoparticles and to measure their sizes. The intensity-calibrated HAADF-STEM image confirms that the (1) the particles are isolated, evenly spaced and not aggregated in two dimensions; (2) the particle coverage is uniform over areas macroscopic compared to the particle size; (3) only about 25% of the surface is covered without much long-range ordering.

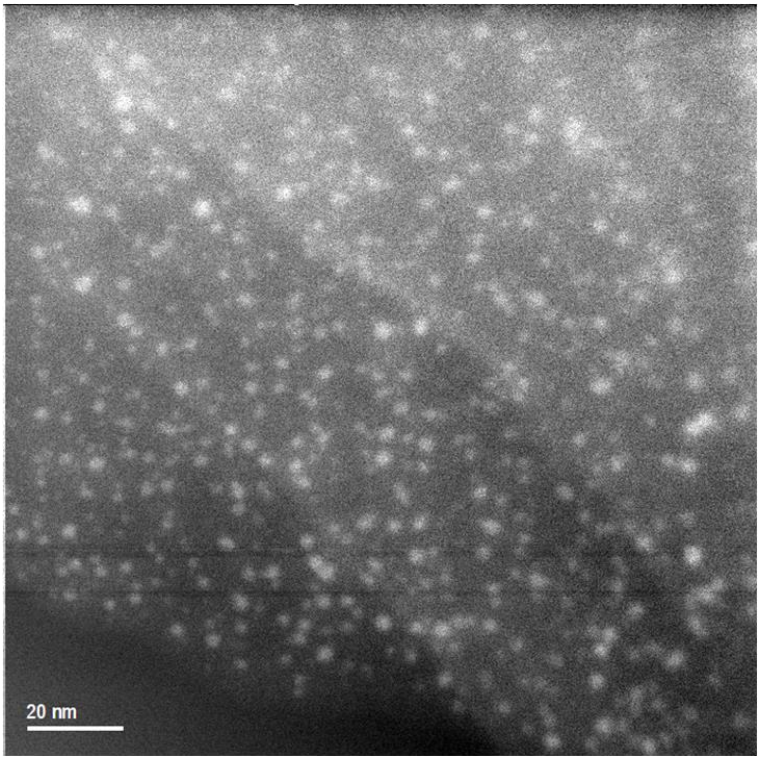

Figure 21 Plan-view HAADF STEM image of Au NPs formed from reduction.

To obtain information about the heights of the nanoparticles, quantification of the intensity distribution in the calibrated STEM image is necessary. For incoherent scattering conditions in

HAADF, the final pixel intensity consists of the sum of the individual scattering contributions from Au atoms together with the background signal [17].

$$I_{\mathrm{Final}} = I_{\mathrm{Au}} + I_{\mathrm{Background}} \quad (3.1)$$

where $I_{\mathrm{Background}}$ is the background signal of the image, which can be easily determined considering that the thickness of the polymer layer is either constant or linearly changing over the area of each nanoparticle. Polymer layers without NPs were used to test how thickness changes affect the HAADF-STEM signal. The image intensity modulations across a micrograph caused by thickness variations of the polymer appear on a scale of significantly more than 20 nm of equivalent Au thickness. However, the local amplitude variations of the signal due to the polymer are at most 20% of the intensity caused by Au NPs of 2 nm diameter. These background intensity variations appear on a larger scale than the size of the NPs studied here. The background signal was therefore determined around each nanoparticle and a linear interpolation of this background signal was subtracted from the image intensities of each nanoparticle. A total of 150 nanoparticles with observable intensity were manually evaluated from the images using the Digital Micrograph *(Gatan Inc*.) software package. The volume of each nanoparticle was determined from the sum of the intensities over the total number of pixels considering the size of each pixel. From the intensity calibration, the volume of each nanoparticle was determined. A mean thickness was obtained for each nanoparticle, as well as the volume. The corresponding volume distribution is shown in Figure 22.

It has to be noted that sodium borohydride is a strong reducing agent which produces small surface bound nanoparticles [56-58]. The average volume <V> of the nanoparticles was found to be 8 nm^3 with a 56% relative standard deviation (RSD) whereas the average area <A> of the nanoparticles was determined to be 6.5 nm^2 with a particle size distribution width of 0.7 nm. Considering the Au NPs to be circular in cross section, the height of each nanoparticle was calculated using equation 3.2.

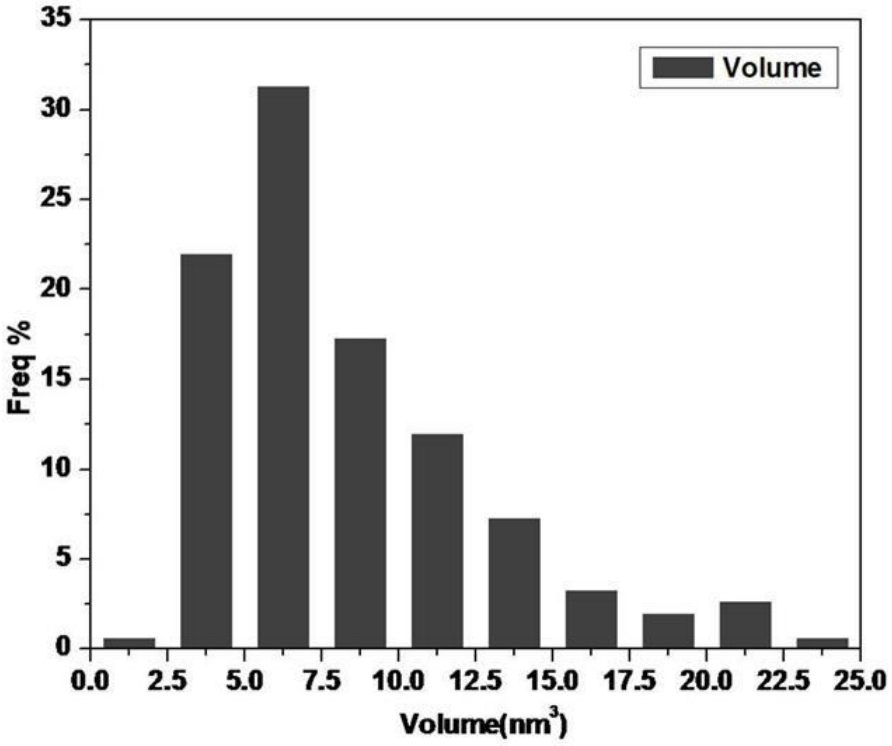

Figure 22 Volume distribution of 150 Au NPs.

$$H_t = 1.5 * Average\ Thickness \quad (3.2)$$

The height distribution of the Au NPs is shown in Figure 23. The nanoparticle height distribution shows that almost 60% of the particles have a height of (1-2) nm. A positive skewness value depicts

the asymmetry of the distribution about the average value and that most nanoparticles have heights below the average height of all the nanoparticles.

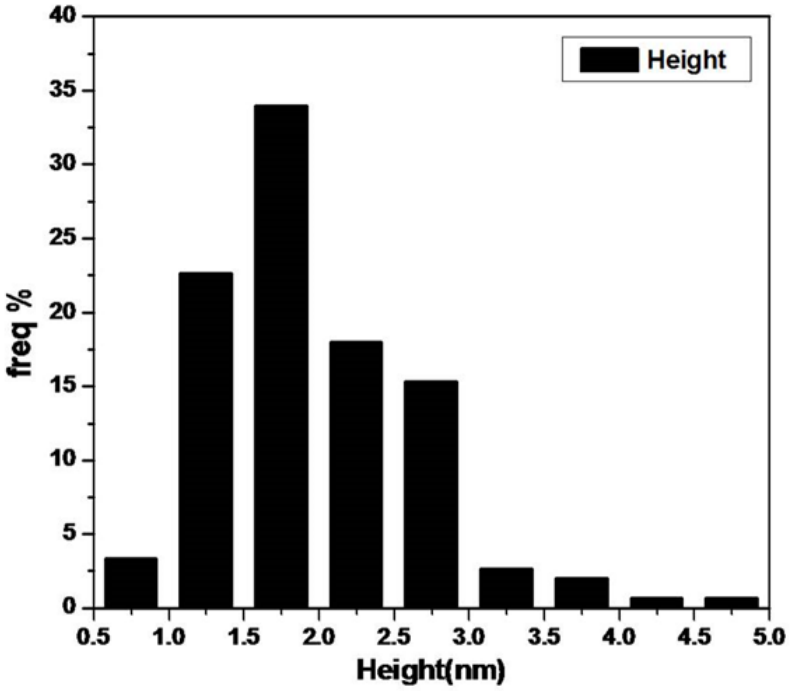

Figure 23 Height distribution of Au NPs from calibrated HAADF-STEM.

The average Au NP height (<H_t>) is calculated taking into consideration the non-linearity of the HAADF detector. The NPs were considered to be circular in cross section and yield a value for <H_t> of 1.97 nm for the 150 NPs. The standard deviation of the height of the nanoparticles σ_H was found to be 0.74 nm from the measurements.

A further attempt was made to study the detailed morphology of the Au NPs if we consider the nanoparticles as ellipsoidal [59]. The in-plane projected shape of the nanoparticles is elliptic rather than circular with a long axis x_n and a short axis y_n, giving an effective diameter of $D_n = \sqrt{x_n y_n}$. Independent of the first measurements where we assumed a circular projection, the long and the

short diameter were now measured manually for each nanoparticle. The same nanoparticles were analyzed again to determine the shape and size (volume) of each nanoparticle. This independent measurement of NP volumes was also performed to test if the criteria for background subtraction and determination of cross sectional area can be consistently applied.

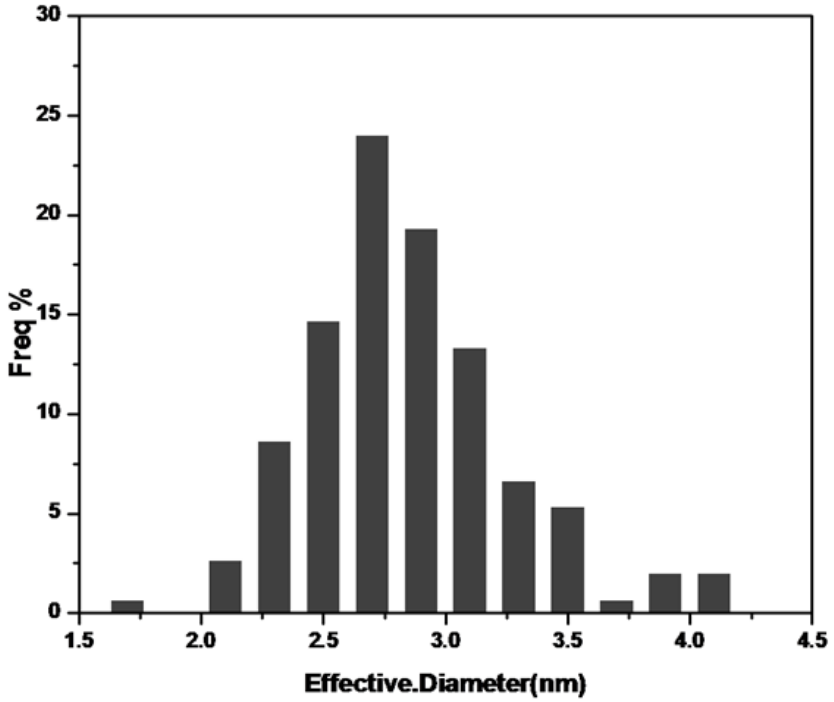

Figure 24 Distribution of the effective diameter of Au NPs.

The effective diameter of the particles distribution is shown in Figure 24. The average effective diameter D_n of Au NPs is 2.84 nm with a majority of nanoparticles having a diameter between 2.5 nm to 3 nm. The in-plane aspect ratio ($\frac{y_n}{x_n}$) of less than 1 suggests that most of the Au NPs are oblate spheroids with ($\frac{y_n}{x_n}$) > of 0.90. Only about 5% of the measured nanoparticles show no deviation from circular projected shape.

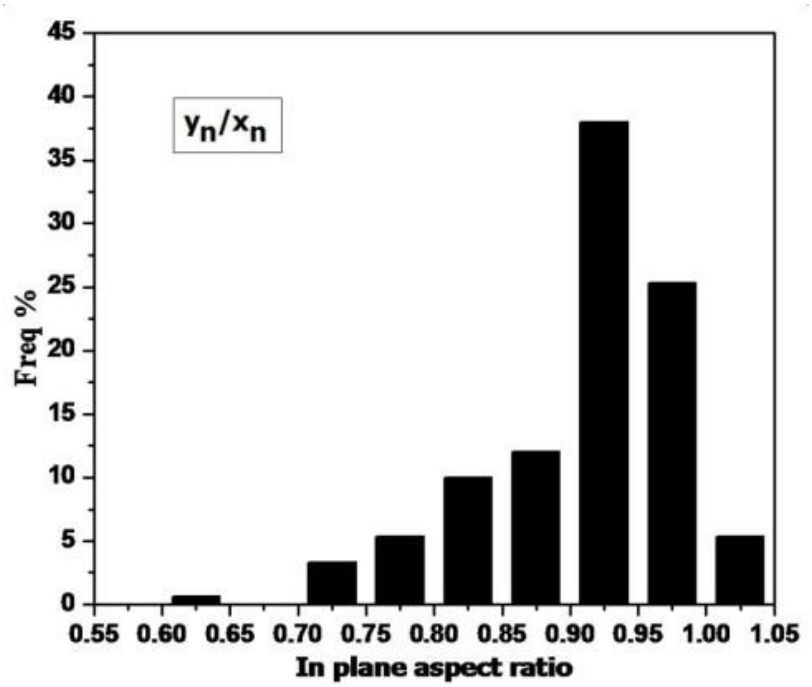

Figure 25 In-plane aspect ratio of distribution of Au NPs

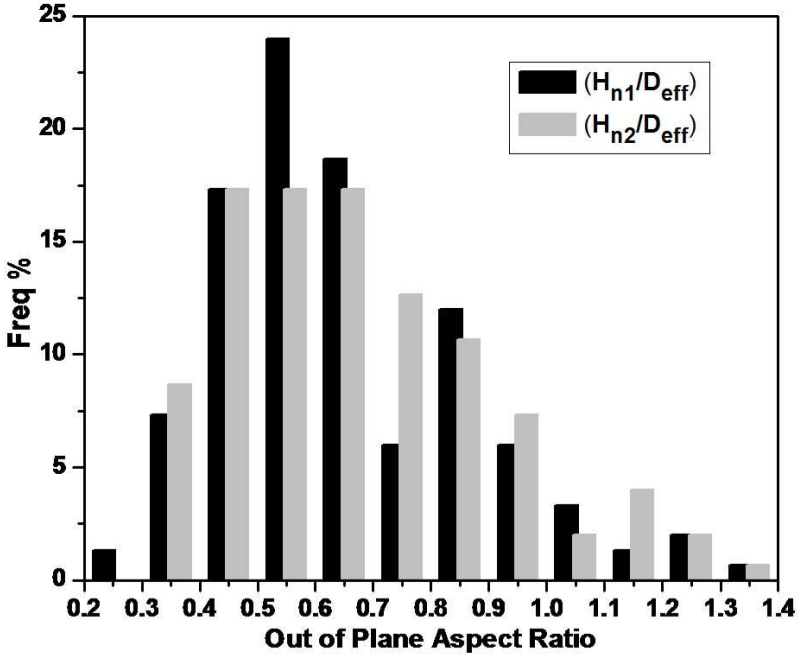

Figure 26 Out of plane aspect ratio of Au NPs distribution.

When further considering that the nanoparticles are ellipsoids having height H_n, the volume is given by $V_n = \frac{\pi x_n y_n H_n}{6}$. The in-plane and out-of-plane aspect ratios $(\frac{y_n}{x_n})$ and $(\frac{H_n}{D_n})$ are shown in the histograms of Figure 25 & 26.

After measuring and evaluating the sizes of 150 nanoparticles, the dimensions of each nanoparticle were determined again in a separate measurement. This was done to check if the data evaluation from the HAADF-STEM micrographs was consistent.

The mean out-of-plane aspect ratios $<\frac{H_n}{D_n}>$ for both independent measurements (the first measurement is indexed as 'n1' and the second as 'n2' in the following) are 0.64 and 0.66, respectively. The mean value <H> and standard deviation σ_H of the height distribution are smaller than the corresponding $<D_n>$ and σ_D values which proves the assumption that the nanoparticles are ellipsoids.

The standard deviation in the height and volume of the nanoparticles is given by:

$$\sigma_H = \sqrt{\frac{\sum(H_{n1}+H_{n2}-2<H>^2)}{4N}} \qquad \sigma_V = \sqrt{\frac{\sum(V_{n1}+V_{n2}-2<V>^2)}{4N}} \qquad (3.3)$$

where the error in the HAADF-STEM data evaluation is:

$$\varepsilon_H = \sqrt{\frac{(H_{n1}+H_{n2})^2}{N}} \qquad \varepsilon_V = \sqrt{\frac{(V_{n1}+V_{n2})^2}{N}} \qquad (3.4)$$

where N is the total number of nanoparticles, V_{n1} and V_{n2} are the volumes from calibrated HAADF STEM images from the two separate measurements. Calculated ε_H and ε_V values from equation 4.4 are 0.04 nm and 1.48 nm^3. ε_H is much smaller than ε_V i.e., the measurement error in the height measurement is significantly smaller than the standard deviation in the size distribution.

3.4 Morphology of Ag Nanoparticles on SU-8 Polymer

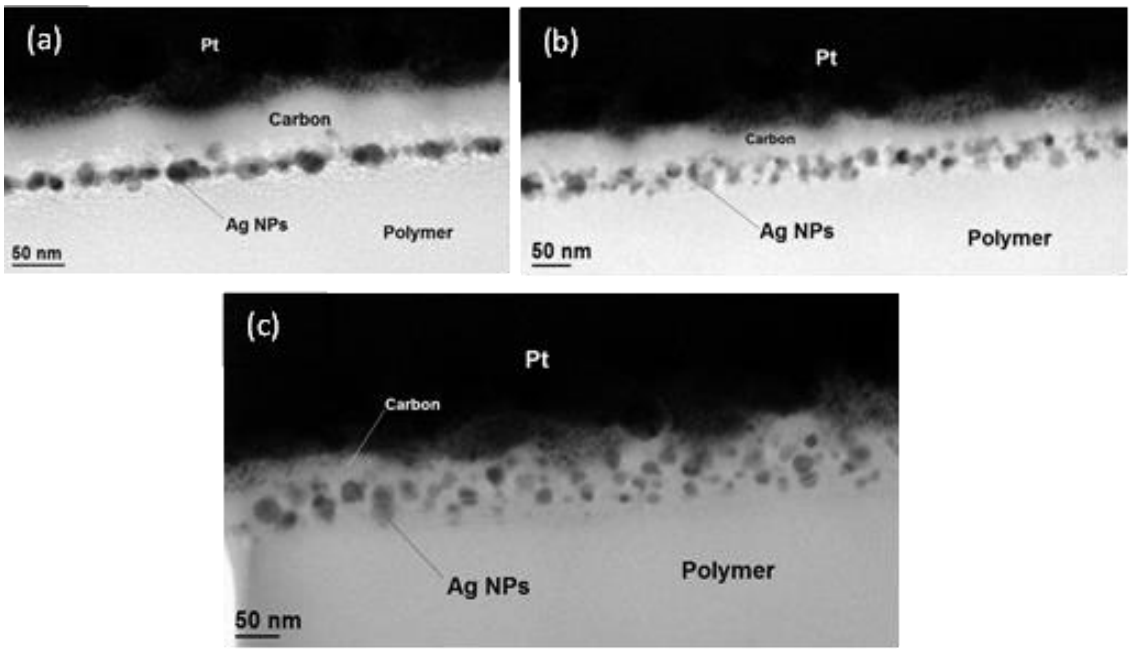

Figure 27 Bright Field TEM micrograph of 30 sec Ag NPs deposited on SU-8 polymer at (a) 0° tilt inside the TEM holder (b) -15° tilt inside the TEM holder and (c) +15° tilt inside the TEM holder.

A set of samples was prepared for different silvering times ranging from 30 secs to 8 min. Figure 27 shows BF-TEM micrographs of a 30 sec silver deposited sample at 0° tilt(a), -15° tilt(b) and at +15° tilt(c). Figure 27(a) reveals that a low deposition time of silver nanoparticles (Ag NPs) the

surface coverage is not 100%. From the edge-on view (Figure 27(a)) the silver layer thickness was calculated to be 30 nm and the Ag NPs are aligned on the surface of the polymer along a straight line. The sample was tilted in the positive and negative direction in the TEM holder to study the distribution of the NPs on the surface of the polymer. From Figure 27(b) and 27(c) it was confirmed that the Ag NPs are distributed on the surface of the polymer one behind another and some of them didn't show up in the edge on view. The TEM sample thickness was determined to be (145±10) nm and the density of the NPs as $7*10^{-4}nm^{-2}$.

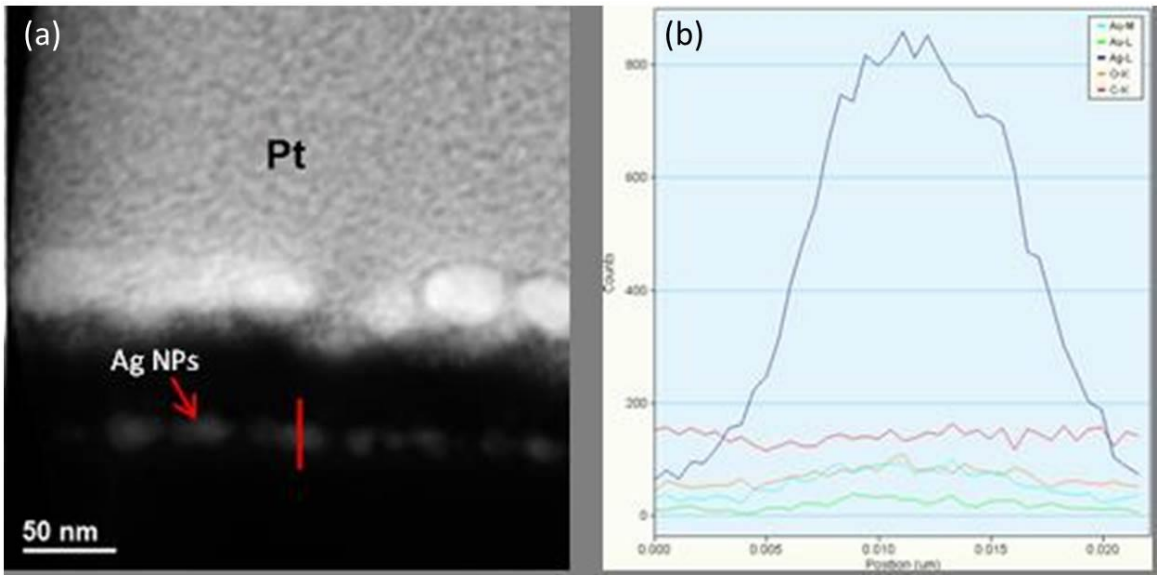

Figure 28 (a) HAADF-STEM micrograph of a 30 sec silver deposited sample. (b) EDS line scan map along the red line shown in (a).

HAADF-STEM micrographs (Figure 28(a)) were taken for EDS analysis. The EDS line scan map across the silver layer is shown in Figure 28(b). Chemical analysis shows no Au signal after the

Ag deposition suggesting the fact that Ag NPs grows on top of Au NPs. EDS measurements confirm the deposition of Ag NPs on top of the Au NPs.

Cross sectional silvered samples were imaged under the TEM in bright field mode to determine the thickness of the silver layer for increasing deposition time. Figure 29 (a) shows such a TEM image of a 3 min silvered sample. The thickness of the silver layer measured in Figure 29(a) is (100±10) nm. The thickness of the silver layer for deposition times varying from 1 min to 8 min from two independent silvering preparations and TEM measurements are shown in Figure 30(a). We see that the thickness increases linearly in the initial stages.

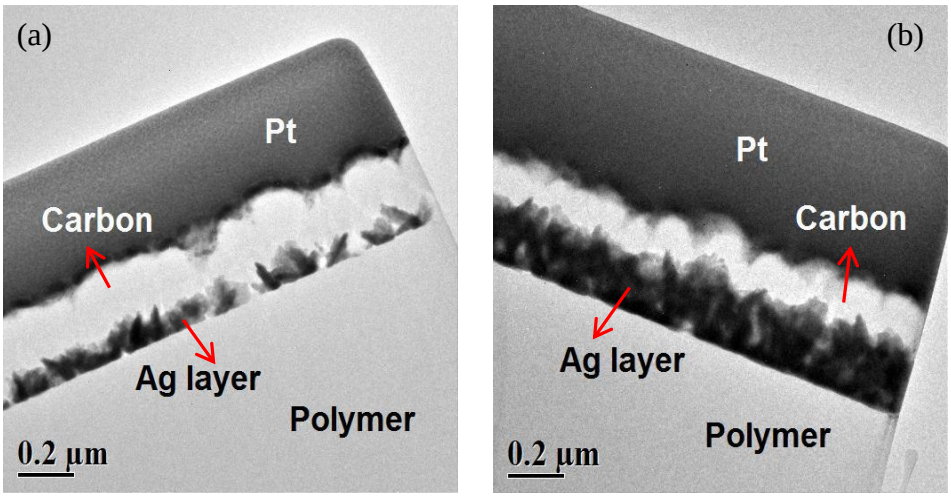

Figure 29 (a) BF-TEM micrograph of 3 min silvering on SU-8 polymer. (b) BF-TEM micrograph of 8 min silvering on SU-8 polymer.

The silver deposition seems to undergo saturation for higher deposition times. For the initial stages of silver growth (Phase I), we confirm that the thickness grows linearly with time up to around six min in the silvering bath where the thickness is roughly around 200 nm. A slow saturation of the

thickness of the silver layer has been noticed as the sample is kept in the silvering bath for longer time when the solution turns greyish.

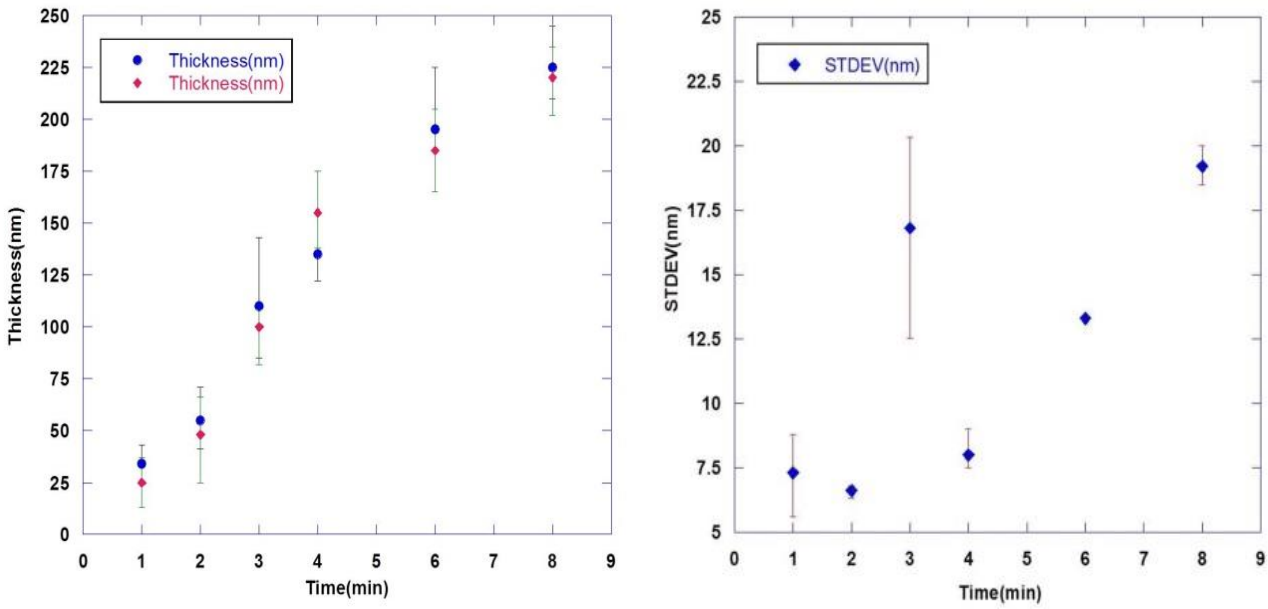

Figure 30 Left (a) Thickness of Ag layers on SU-8 polymer as a function of time. Right (b) Sample roughness studied over deposition time of Ag NPs on SU-8 polymer.

Figure 30(a) also shows that we get almost the same response of the thickness curve at a later time. This confirms that the thickness of the silver layers prepared by electroless deposition does not change over time.

The standard deviation of the height fluctuations increases over longer periods of deposition. At first the polymeric surface is not fully covered with silver nanoparticles which attributes to the high value of surface roughness after 1 min silver deposition (Figure 30(b)). For longer deposition time the sample gets slowly covered with the silver layer, so the sample roughness increases gradually. After 3 min deposition, we notice an abrupt increase in roughness due to needle-like growth on initial layers as can be seen from Figure 29(a).

The increased roughness of the surface of the silver layer after 3 min deposition is due to the silver particles growing on top of each other to form platelet-like structures. These platelets are made of spherical structures which grow with time. The platelets are oriented randomly as shown in Figure 31.

Gum Arabic, a complex protein, acts as a gluing agent in solution and hinders the growth of silver. It also stabilizes the growth morphology as shown in Figure 31. The surface roughness of the silver layer is reduced with use of gum arabic in solution (Figure 32). It does not reduce the particle size but controls the growth of the silver layer. With gum arabic in the electroless silver solution we control the thickness of silver layer at varying deposition times.

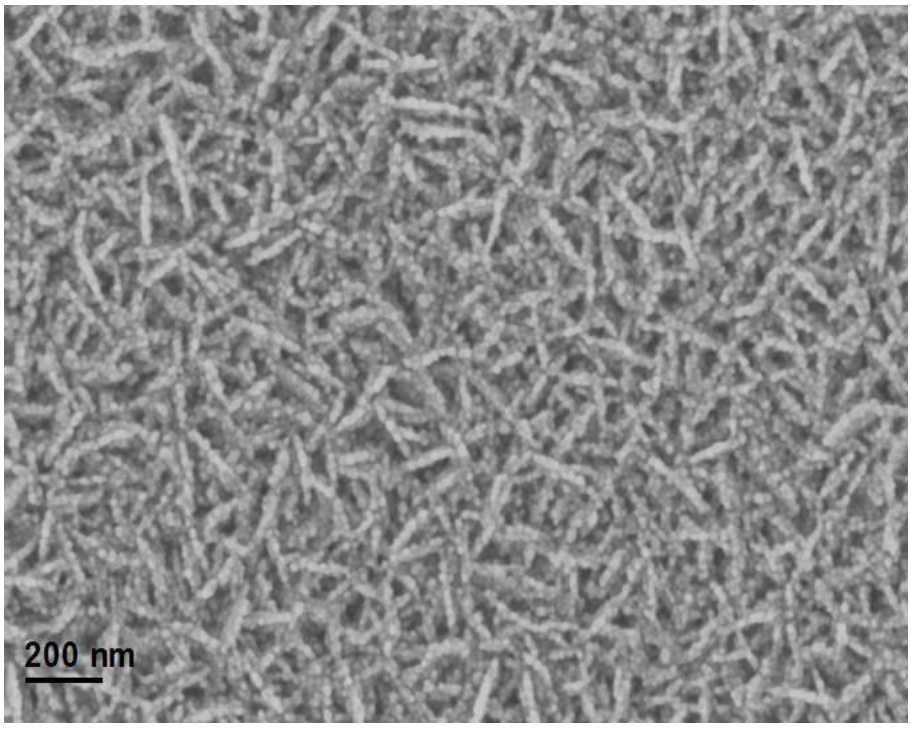

Figure 31 SEM image of 3 min Ag deposition (without gum arabic).

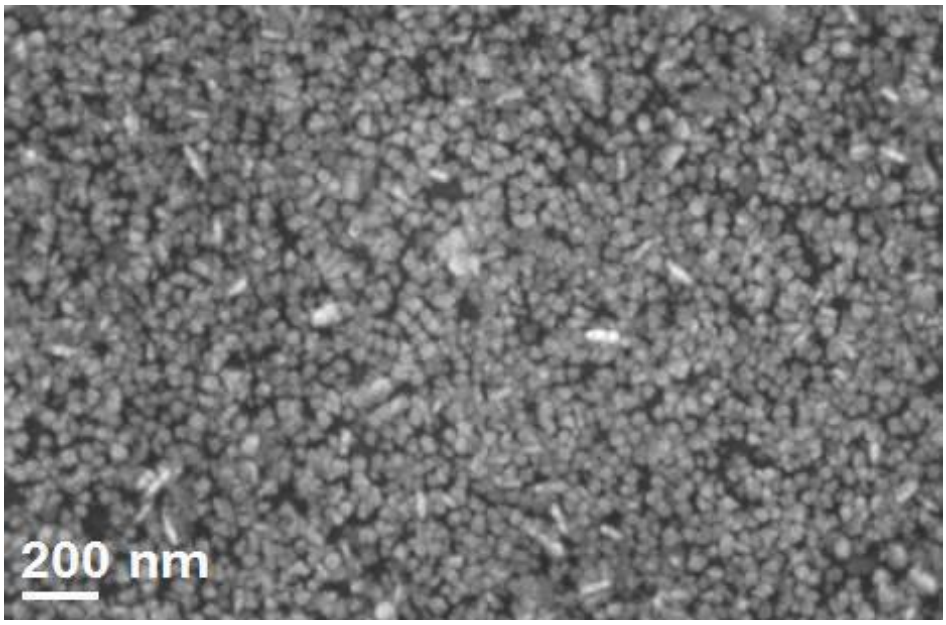

Figure 32 20 min Ag deposition(with gum arabic).

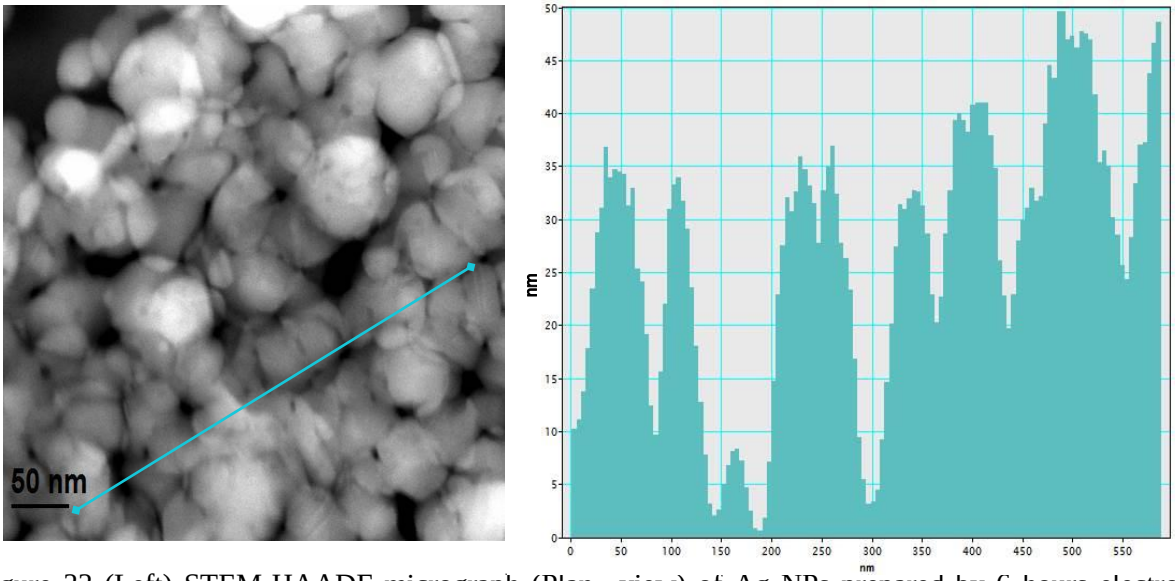

Figure 33 (Left) STEM-HAADF micrograph (Plan –view) of Ag NPs prepared by 6 hours electroless deposition in presence of Gum Arabic. (Right) Thickness vs Position (Line Profile) across line shown in Left image.

Figure 33(Left) shows a plan-view HAADF-STEM micrograph of Ag NPs formed on SU-8 polymer using gum arabic in solution. The fraction of electrons scattered per nm for silver is 0.16% from reference samples. The thickness of the silver layer was determined at different positions of the samples according to the procedure described in section 3.3. The background noise was subtracted and the summation was done over all the pixel intensities keeping the contrast-brightness settings same as for the Au NPs. The average signal on the HAADF detector was taken into account to determine the average integrated thickness of the silver grains. The average thickness of the silver layer is 45 nm with a standard deviation of 18 nm. Figure 33 (Right) shows the thickness profile across the sample shown by the line in the left image. The granular structure of silver grains accounts for the large standard deviation. The average volume calculated for the Ag grains is (65000±9000) nm^3 yielding an average particle diameter of 50 nm.

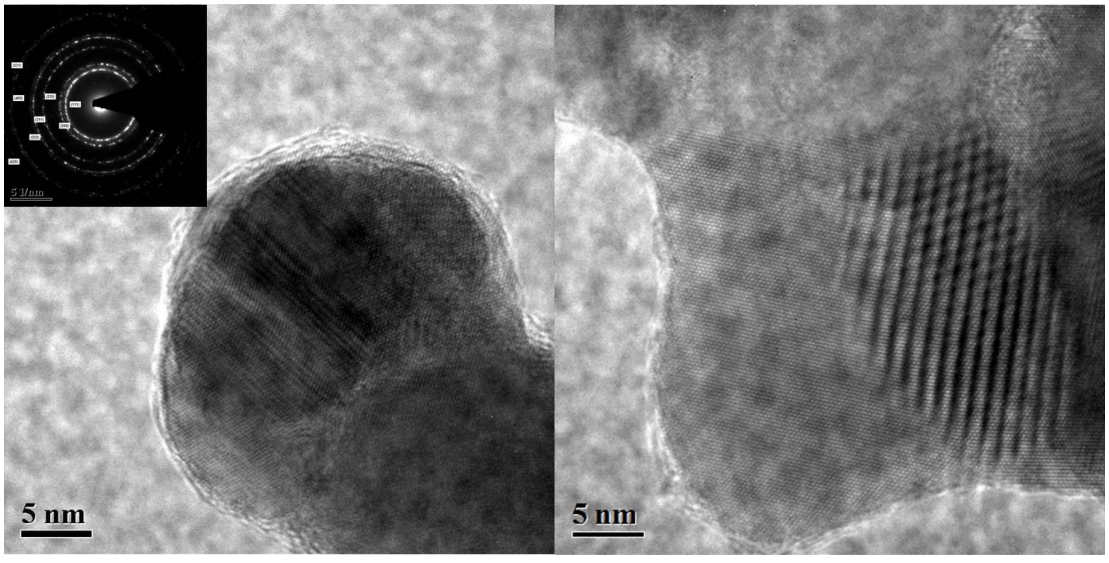

Figure 34 (Left) HR-TEM micrograph of a Ag NP with the diffraction pattern in the inset. (Right) Formation of Moiré pattern as seen in HR-TEM micrographs.

The crystal structure of the nanoparticle was studied from the HR-TEM micrograph of a silver nanoparticle. The diffraction pattern was indexed and the F.C.C structure of silver was confirmed with (111) and (200) as the most dominant planes as shown in the Figure 34 (Left). The high resolution micrographs also reveal the formation of Moiré pattern (Figure 34 (Right)) which stems could be from the combined electron scattering of neighboring planes (111) and (200) overlapping in projection.

Figure 35 shows silver nanoparticles formed from electroless deposition using gum arabic as a stabilizing agent. The concentration of the silvering media was maintained at 5.6 mM as discussed earlier.

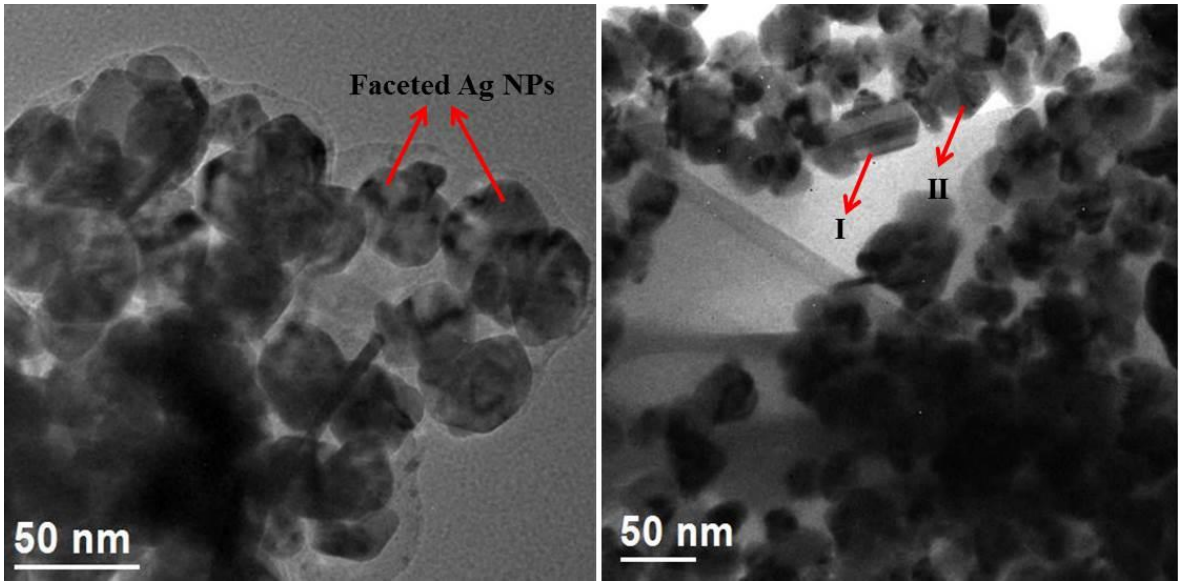

Figure 35 (a) Faceted Ag NPs formed from 6 hr electroless deposition with gum arabic using silvering solution concentration 5.6 mM. (b) Twinned hexagonal shaped Ag NPs viewed from different angles.

The electroless deposition was carried on for 6 hrs after which we get faceted silver nanoparticles as shown in Figure 35 (a). Random faceting was observed and Ag NPs overlapped with each other as can be seen from the TEM micrograph in Figure 35 (a). Faceting of Ag NPs may be due to the stabilizing agent (gum arabic) which hinders the growth of the nanoparticle. In Figure 35 (b) two specific nanoparticles are shown, nanoparticle I is cylindrically shaped while nanoparticle II is hexagonal in shape. When viewing the particles in different angles a twin boundary can also be seen in the middle of the particle (nanoparticle I in Figure. 35(b)). These densely faceted structures maintain their size uniformity exhibiting a well-defined shape.

Fivefold twinning has been observed in silver nanoparticles prepared by electroless deposition method as shown in Figure 36. In addition to the twin boundaries the electron diffraction reveals a d-spacing of the planes ~ 2.07 Å which corresponds to the (200) planes.

The twin boundaries are equivalent to a crystallographic rotation and the (200) planes covered a much larger fraction of the particle surface. In fact in F.C.C structures, lattice mismatch and errors in the stacking of atoms during grain nucleation is a common reason for the formation of twin defects [60]. These twin defects are also formed due to the lack of a significant difference of binding energy for atoms in the local structure around a twin boundary and other (perfect) parts of the grain [60]. In other words, the stacking fault energy of silver is low with (0.02-0.03) J/m^{-2} [61, 62] making it possible that hexagonal stacking sequences appear besides the stable FCC stacking sequence. Numerous TEM studies on nano-crystal have shown that with slight excitation energy, even at room temperature (~k_BT) is enough to induce structural changes in the crystal structures.

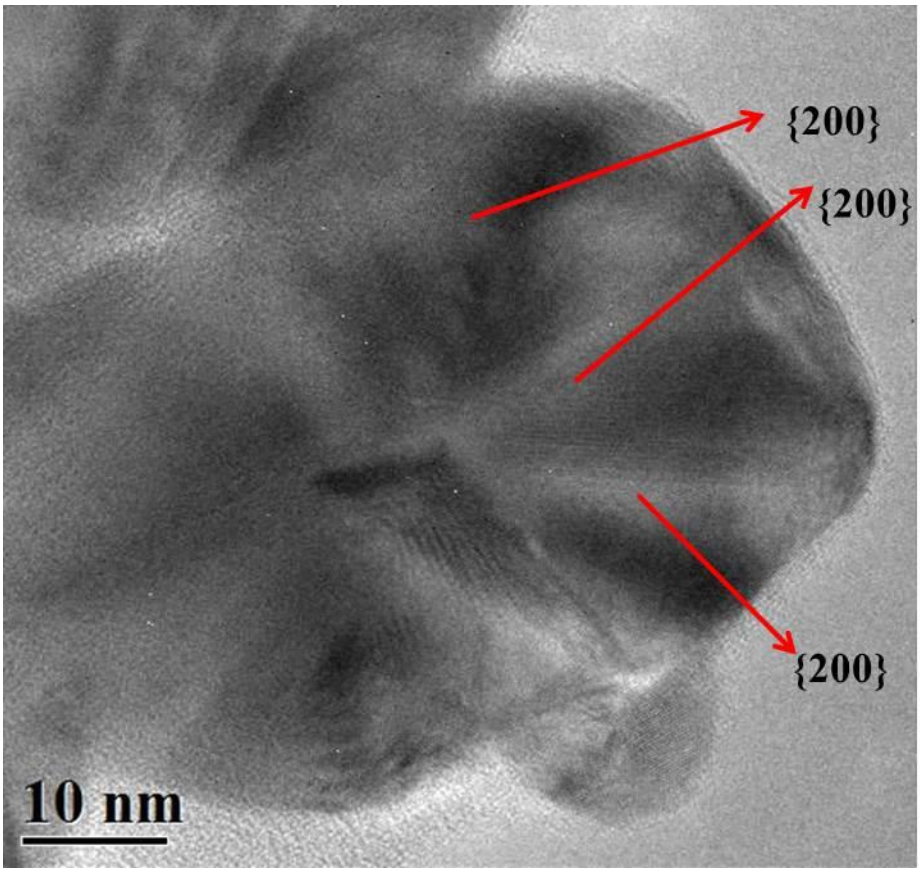

Figure 36 Faceted silver nanoparticle showing five fold twinning.

These fluctuations increase with a decrease in the size of nano-crystals [63, 64]. Figure 37 (A) shows the HAADF-STEM micrograph of 4 min Ag NPs deposition by EMPS. Due to the longer deposition time, silver gets deposited homogeneously on the polymer which is represented by higher intensity (white areas) on the image. Some areas in the image show regions with darker contrast. A profile scan of a portion of the image depicts the fact that silver deposition is hindered in some regions (black areas) where the HAADF-STEM signal falls as shown in Figure 37 (B). This possibly is the result of silver growth on nucleating sites of gold ion. Such distributions of silver layers were not seen in cross-sectional samples studied under the TEM.

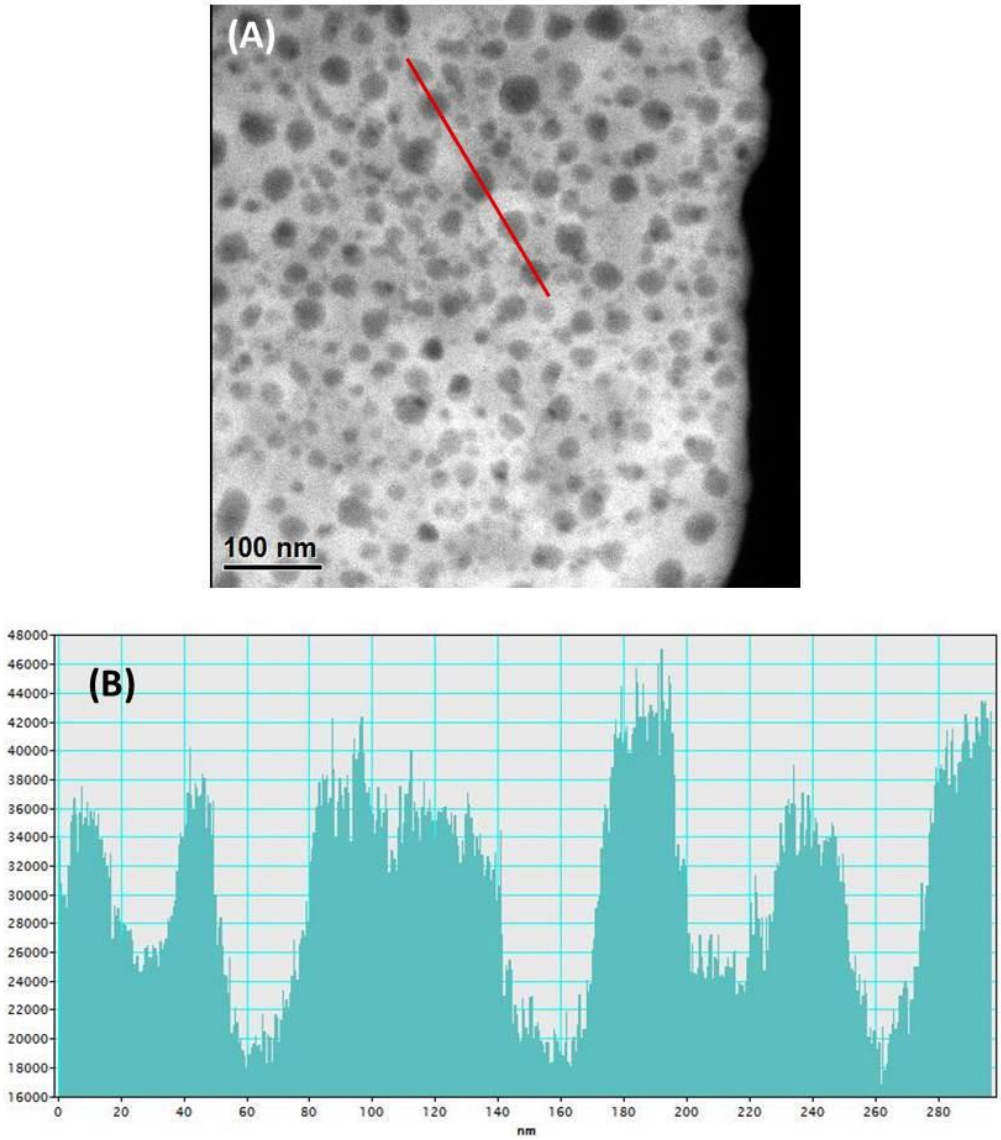

Figure 37 (A) Plan-view HAADF-STEM micrograph of Ag NPs on SU-8 polymer. (B) Profile scan of Ag NPs depicting the intensity in the HAADF-STEM mode.

The SEM images in Figure 31 & 32 show regions where the coverage is not 100% as confirmed by plan-view studies. When the thickness of the object is not negligible to its lateral dimension, the 2D characterization of various structural features such as volume distribution, densities and distances between the particles are not accurate.

3.5 Tilt Series Imaging

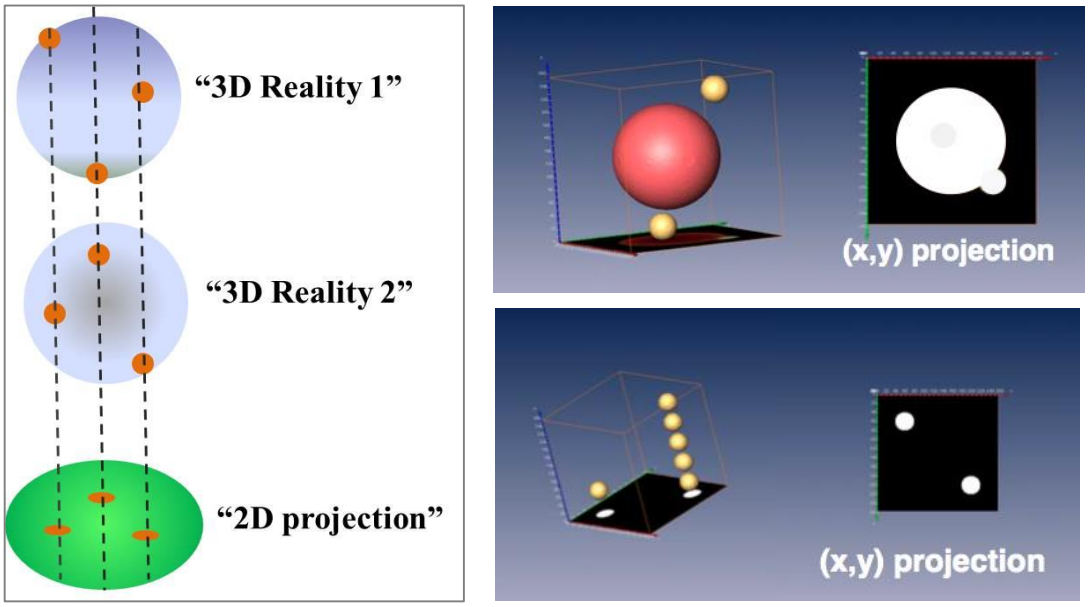

Figure 38 3D Reality and 2D Projection.

As shown in the schematics in Figure 38 for different locations of nanoparticles on the surface of a material we get the same 2D projection which leads to wrong parameters and distributions. To obtain the real parameters (volume, density and distance between the NPs) a stereoscopic approach is needed which in our present case is done by tilt series imaging.

In this case the Au NPs formed on or near the surface of the polymer reduced by sodium borohydride are 2-3 nm in diameter with average height of 1.97 nm. To study in detail the morphology and distribution of nano-scaled objects, tilt-series imaging has been performed by many research groups using TEM, e.g, [48, 65-67]. Tilt-series imaging of crystalline samples in the STEM and EFTEM mode has been carried out in the past to determine the morphology of the nanoparticles [4, 68, 69].

In the present work samples were prepared by reduction with $NaBH_4$. Cross sectional samples for tilt series imaging were prepared using FIB which are sufficiently thin since the projected thickness increases drastically at large tilts (>45°). Images for the tilt series were taken at intervals of 3-5° by tilting the sample in the holder. Different sets of images were acquired both in the BF mode and scanning mode. The maximum tilt for the experiment was ±40° partly due to hardware restrictions for the sample holder in the microscope and also due to overlapping of the Au NPs layer with the top carbon coating which decreases the viewing angle of the NPs. Figure 39(b) shows a 25° tilted HAADF-STEM micrograph of Au NPs reduced by $NaBH_4$.

As the sample is tilted away from the edge-on position the nanoparticles move in a direction perpendicular to the tilt axis. Figure 39(b) below shows a band of width ≈ 90 nm where the nanoparticles are distributed. In the edge-on view of Figure 39(a), the nanoparticles overlap each other.

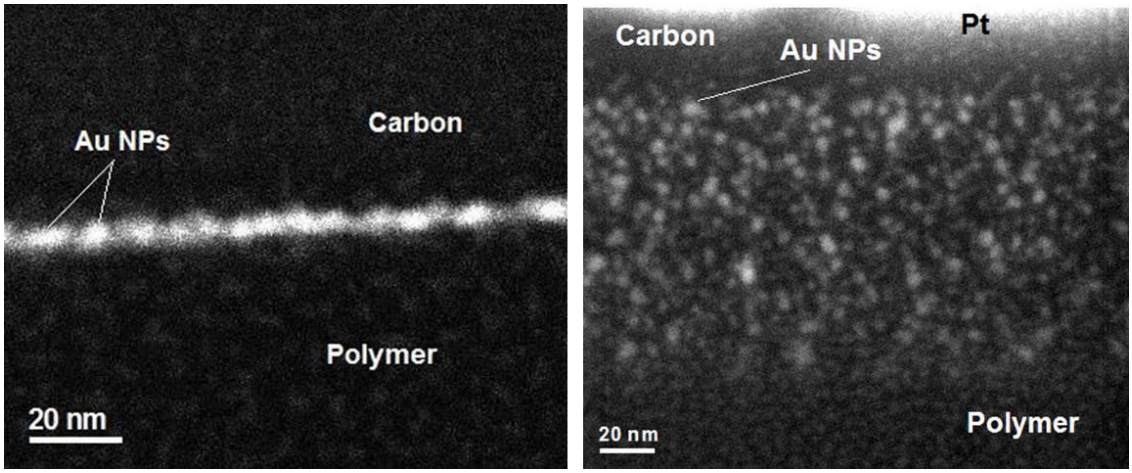

Figure 39 (a) STEM 0° degree tilted micrograph of Au NPs created by TEPA functionalization of SU-8 polymer. (b) Au NPs 25° tilted micrograph.

From more than one micrographs at different tilt angles, we figured out the trajectory of a nanoparticle with a known tilt direction. Due to the random orientation of samples on the Cu grid, it sometimes becomes difficult to tilt the sample so that sample is viewed edge-on with respect to the electron beam. Therefore, accurate sample tilts for edge-on viewing were carefully evaluated before proceeding with a tilt series and in some cases, the TEM grid has to be realigned in the sample holder.

CHAPTER 4: TEMPERATURE DEPENDENCE OF THE HAADF-STEM SIGNAL

High-energy electrons (300 keV) scattered to high angles mostly suffer thermal diffuse scattering and the image formed yields atomic number contrast. These images are called the Z-contrast images where the scattering cross section varies roughly as Z^2 [70-72]. In crystalline materials the atomic channels get increasingly disrupted with an increase in temperature and high-angle scattering increases with temperature and thickness of the material as shown by Rumayana Petrova [73-75]. However only a few studies have been reported for amorphous materials [73, 76, 77]. Absence of extended channels, different Debye temperatures, different masses and different chemical bonding may be the reason for differences in the HAADF signal for amorphous materials [73]. HAADF-STEM intensities at different temperatures for different elements and compounds are measured here and possible explanations are provided in this chapter.

4.1 HAADF Intensity Dependence on Temperature

A cross sectional sample was prepared using the FIB (as described in section 1.6) from the specimen (provided by TQS) and used for the HAADF-STEM measurements. The sample studied here is a multilayered sample consisting of both polycrystalline and amorphous materials of fixed thicknesses. The specimen was heated in the FEI double tilt holder to 368 K and STEM images were acquired as the sample slowly cooled down. The temperatures at which micrographs were recorded are 368 K, 297 K (room temperature), 173 K and 98 K. Line scans were performed and the HAADF-STEM intensity was measured at specific positions of the sample in shown in Figure 40. The HAADF-STEM intensity was converted to CCD intensity using equation 2.4 and the ratio

of the CCD intensity and detector intensity (normalized) was plotted with position of the electron beam on the sample for Pt layer(Figure 41) and the Si layer (Figure 42). In this experiment the projected sample thickness was uniform throughout the sample.

A small fluctuation is observed in the CCD signal for the Pt layer with position suggesting that there is no significant effect of temperature on the scattering of electrons to high angles. Often in a crystal the incident electrons are channeled along the atomic columns parallel to the optical axis [78] thereby affecting the high-angle scattering and the fluctuations may be due to this channeling.

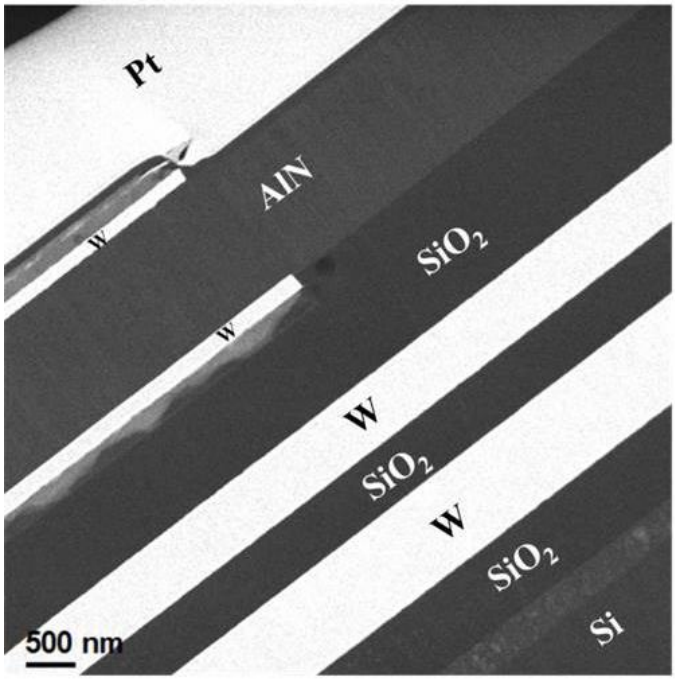

Figure 40 HAADF-STEM image of a multilayered sample.

Also displacement of atoms due to structural defects [79, 80] or thermal vibrations [77, 81, 82] along a channel increase the probability of scattering and small fluctuations of the CCD signal arise.

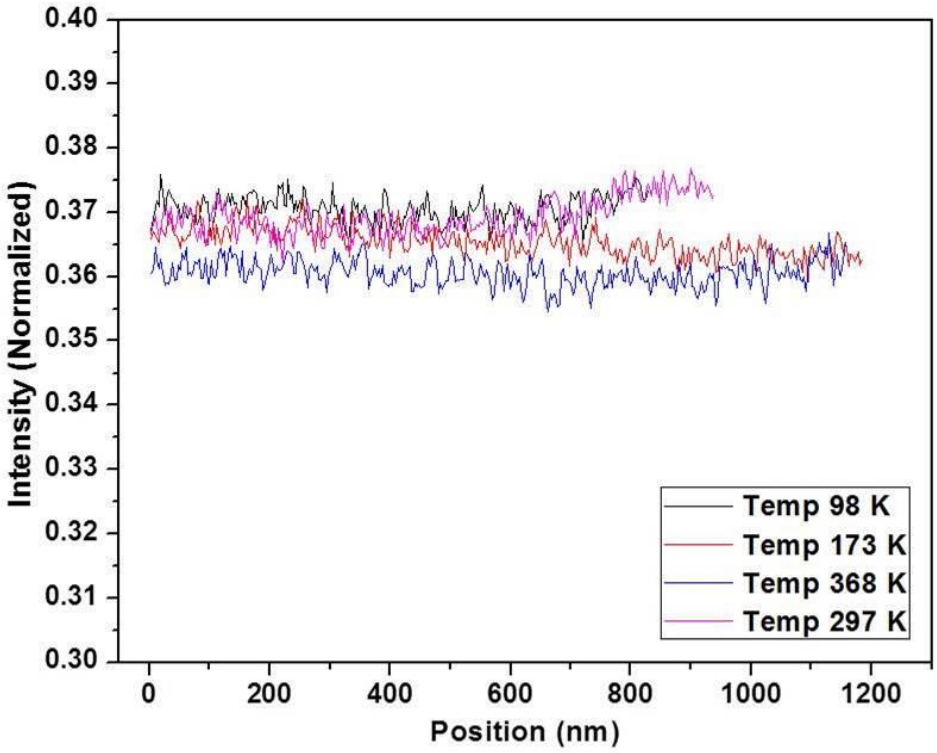

Figure 41 CCD signal with respect to position on the sample for a platinum layer.

Figure 42 shows the intensity line profile for the silicon layer which also confirms the fact that there is no significant change in the HAADF signal with temperature. However at 173 K considerable amount of variations is observed. These modulations may be due to the electron beam interactions with atoms arranged in specific crystallographic orientations and the strong Kikuchi patterns visible in the diffraction mode.

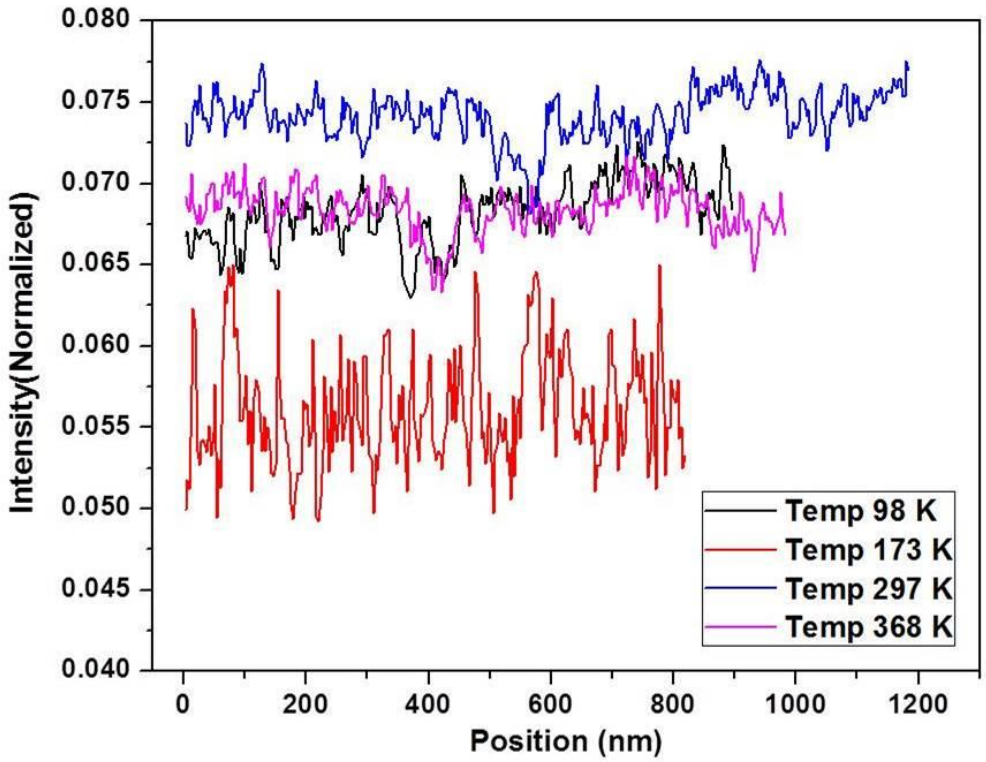

Figure 42 CCD signal with respect to position on the sample for Si layer.

The temperature dependence for the HAADF intensity was also measured for different elements including amorphous SiO_2. Figure 43 shows the plot for the normalized CCD intensity at four different temperatures for W, Si, Pt, AlN and SiO_2. While no significant change of the HAADF contrast is recorded at different temperatures for any of these specific materials, a relative temperature dependency of the atomic number contrast is observed in polycrystalline and amorphous materials. The HAADF–STEM contrast is higher in elements with higher atomic number (platinum & tungsten). This suggests that atomic masses, Debye temperatures and angular dependencies of their atomic scattering factors do play a role in determining the high angle scattering signal as follows from the Einstein model [73].

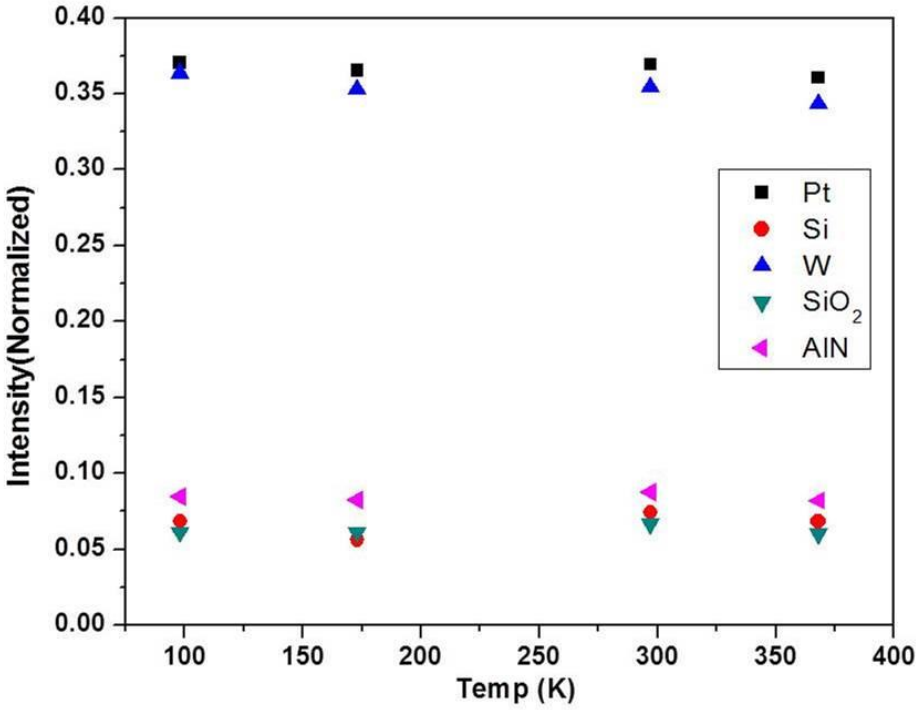

Figure 43 Normalized CCD signal for elements/compounds at different temperatures.

4.2 Conclusions

A change in the HAADF signal due to compositional variations in an alloy has also been reported by *Libera et al.* [73]. In such a case the total scattering is considered to be the weighted sum of scattering from individual atoms of elements in an alloy. In our case the thickness of TEM sample was constant. It can be concluded from the present study that temperature doesn't play a significant role in the variation of HAADF-STEM signal. This work confirms that minor fluctuations in the HAADF signal can arise due to crystallographic orientations.

CHAPTER 5: HAADF-STEM CONTRAST SIMULATIONS

5.1 Literature Review

HAADF-STEM images are to a large extent formed from incoherently scattered electrons. The influence of electrons coherently scattered from atoms and atomic columns as has been studied in the past and compared to incoherent scattering. Since thermal diffuse scattering (TDS) plays an important part in the formation of HAADF images, HAADF images are relatively free from thickness fringe or defocus effects compared to the image formation in conventional TEM [83]. Pennycook and Nellist have shown that coherently scattered electrons can also produce an incoherent image [84]. STEM contrast simulations play an important part in understanding the contribution of TDS to HAADF-STEM images. STEM image simulations require extensive computing time and power as at each scan position dynamical scattering effects need to be considered. STEM simulations have been carried out by *Kirkland et al*. [85-87], Pennycook & Jeson [83] , Wang & Cowley [81] with different approaches how to include the TDS contribution to the HAADF-STEM contrast.

The scattering cross-section σ for electrons scattered by an atom on the HAADF detector is given by:

$$\sigma = \frac{\varepsilon W_{at}}{N_A \rho} \qquad (5.1)$$

[88] where ε is the fraction of electrons scattered per nm of a single-element material, W_{at} is the atomic mass, $N_A$is the Avagadro number and ρ is the density of the material.

Müller and Rose [89] used a simple model by describing the electric potential around an atom with the Wentzel potential given by the following equation:

$$U(\boldsymbol{r}) = -\frac{2\gamma Z}{a_H}\frac{exp(-\frac{|\boldsymbol{r}|}{R})}{|\boldsymbol{r}|} \quad (5.2)$$

where R is the shielding radius, $a_H = \frac{\hbar^2}{m_0 e^2}$ denotes the Bohr radius and Z the atomic number. The parameter $\gamma = m/m_0$ in equation (5.2) is the relativistic correction.

The interaction cross section can be expressed by:

$$\sigma = \int_{2\Theta_{min}}^{2\Theta_{max}} |f^2(\theta)| 2\pi \sin(2\theta) d(2\theta) \quad (5.3)$$

with an integral over the whole angular range of the detector area. The atomic scattering factor *f* can be written as a function of scattering vector $|q|=2\pi \text{ Sin}(\Theta)/\lambda$ or Bragg angle according to:

$$f(q) = f(\theta) = \frac{2Z(1+\frac{eV}{m_0 c^2})}{a_{Bohr}(R^{-2}+q^2)} \quad (5.4)$$

where $$R = \frac{a_{Bohr}}{Z^{1/3}} \quad \& \quad a_{Bohr} = \frac{h^2 \varepsilon_0}{\pi m_0 e^2} \quad (5.5)$$

For small angles, $$q = 2\pi \frac{Sin\theta}{\lambda} = 2\pi|\overrightarrow{g}| \approx 2\pi \frac{2\theta}{\lambda} \quad (5.6)$$

Substituting the values of R and a_{Bohr} in (5.4) and integrating over the detector (Appendix A) we get:

$$\sigma = \frac{Z^2\lambda^4}{16\pi^3 a_{Bohr}^2}(1+\frac{eV}{m_0c^2})^2\left[\frac{1}{\frac{Z^{2/3}\lambda^2}{16\pi^2 a_{Bohr}^2}+Sin^2\Theta_{min}} - \frac{1}{\frac{Z^{2/3}\lambda^2}{16\pi^2 a_{Bohr}^2}+Sin^2\Theta_{max}}\right] \quad (5.7)$$

Therefore,

$$f(\theta)_{small} \approx \frac{2h^2(1+\frac{eV}{m_0c^2})}{\pi m_0 c^2} Z^{1/3} \quad (5.8)$$

To be consistent with the available literature, I used $a_H = a_{Bohr}$ in equation (5.4) as Müller and Rose used equations without the term $(4\pi\varepsilon_0)^{-1}$for interactions between charges as in equation (5.2)

For small scattering angles the interactions cross section is therefore, $\sigma \sim Z^{2/3}$

For larger angles however,

$$f(\theta)_{large} = \frac{2Z(1+\frac{eV}{m_0c^2})}{(\frac{Z^{2/3}}{a_{Bohr}}+\left(\frac{2\pi Sin\theta}{\lambda}\right)^2)} \quad (5.9)$$

yields $$\sigma \sim Z^2 \quad (5.10)$$

In the above equations σ is the interaction cross section, Z is the atomic number of the element, λ is the wavelength of electrons, 2θ is the angle of scattering on the HAADF detector, $a_{Bohr}$is the Bohr Radius, m_0 is the rest mass of an electron and c is the speed of light.

Equation (5.10) almost gives a Z^2 dependence of the interaction cross section σ, but experimental values calculated by Biao Yuan [90] yields a much lower exponent for the atomic number dependence of the scattering cross section as shown in the plot below.

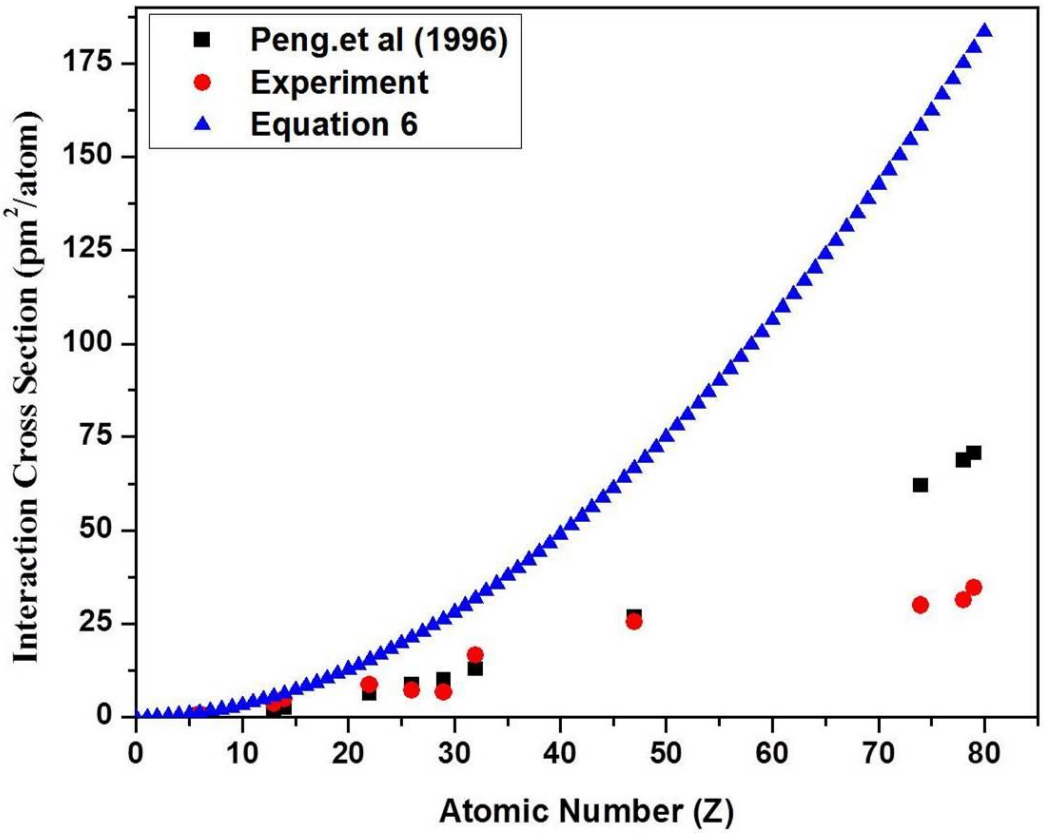

Figure 44 Interaction cross section for different pure elements. Experimental data points are from the dissertation of Biao Yuan [53]. Equation 5.7 yields the data shown with blue triangles. *Peng et al*. [2] data points are derived from the parameters given in *Peng et al*.[2].

For electron diffraction at high energies the electrons interact with the solid via an electrostatic coulomb potential. This potential exists between the incident electrons and electrons and positively charged nuclei of the solid. The incident electrons lose a part of their energy ($\Delta E = E_f - E_i$) (subscript f and i denotes the final and initial states) if scattered inelastically while the atom transitions to an excited final state from an initial state. If the scattering is an elastic one then the initial state of the atom is preserved ($\varphi_f = \varphi_i$).

For a solid containing N number of atoms, the complex potential representing the interaction between the electrons and the solid is given by:

$$V(r) = \sum_{i=1}^{N} \varphi_i(r - r_i) \qquad (5.11)$$

Equation (5.11) represents the contribution to the atomic potential from all the atoms. $\varphi_i(r)$ is the contribution from the i^{th} atom and is related to the atomic scattering factor $f^{(e)}(s)$ by the following Fourier transform :

$$\varphi(\boldsymbol{r}) = \left(\frac{h^2}{4m_0\pi^3}\right) \int f^{(e)}(\boldsymbol{q}) \exp(2i\boldsymbol{q}.\boldsymbol{r})\, d^3\boldsymbol{q} \qquad (5.12)$$

where m_0 is the rest mass of an electron and h is the Planck constant.

Some of the inelastically scattered electrons get ‘absorbed’ as they lose a significant fraction of their energy and are not anymore detected by any of the detection channels of a TEM. These electrons may have lost several keV energy and the chromatic aberration of the electron lenses deflects these electrons onto paths which do not permit the electrons to reach the camera system

of the transmission electron microscope. Other electrons are inelastically scattered, lose some energy (in the 10 meV range for phonon excitations, several eV for exciton and plasmon excitations to a few keV range for core losses and for Bremsstrahlung excitation), but still reach the camera system in TEM. These electrons have lost their phase relation with the incident electron beam and therefore do not contribute to the diffraction pattern of Bragg reflections. Instead they form an intensity background in the diffraction pattern and give rise to Kikuchi lines for crystalline materials. These electrons contribute to the imaginary part of the complex potential described in equation (5.11). The real part of equation (5.11) is referred to as *elastic scattering factor* and the imaginary part of the complex potential is the *absorptive scattering factor*. The real part of the atomic potential has been calculated by several authors [91, 92] using relativistic Hartree-Fock wave functions.

Doyle & Turner [92] gave analytical expressions for the *elastic scattering factors*:

$$f^e(s) = \sum_{i=1}^{n} a_i \exp(-b_i s^2) + c \qquad (5.13)$$

where a_i, b_i and c are parameters determined by curve fitting procedures [93]. In equation (5.13),$s = \frac{\sin\theta}{\lambda}$, where θ is half the angle of scattering (2θ total scattering angle) and λ is the wavelength of the incident electrons.

The elastic scattering factors for elements in the periodic table were computed by *Peng et al.* [2] using the combined modified simulated-annealing procedure [94] and the least-squares method for solving algebraic equations [95]. The computed values for elastic scattering factors by *Peng et al.* [2] for the range $s = 0 \rightarrow 6\,\text{Å}^{-1}$ are more accurate as compared to Doyle & Turner [92] ,

Weickenmeier & Kohl [96] and Bird & King [97]. The coefficients for elastic scattering factors by *Peng.et al*. [2] are used in this project for the simulation of HAADF-STEM images.

For an atom in a crystal vibrating around its mean equilibrium position, the thermal displacement is (in one dimension) described by U_x; the Debye-Waller factor is given by:

$$B = 8\pi^2 < U_x^2 > \quad (5.14)$$

where $< U_x >$ is the thermal average of the x-component of the displacement of the atom.

In the Debye model the average square displacement is given by [98]:

$$< U_x^2 >= (\frac{\hbar}{2m}) \int_0^{\omega_m} Coth\left(\frac{\hbar\omega}{2k_BT}\right)\left[\frac{g(\omega)}{\omega}\right] d\omega \quad (5.15)$$

in which m is the atomic mass, T the temperature, k_B the usual Boltzmann constant, $g(\omega)$ is the normalized phonon density of states and ω_m is the maximum phonon frequency. Substituting, $x = \omega/\omega_m$ and $y = T/T_m$ in equation (5.15) and inserting in equation 5.14:

$$B = \frac{4\pi^2\hbar}{m\omega_m} \int_0^1 Coth\left(\frac{x}{2y}\right)\left[\frac{f(x)}{x}\right] dx \quad (5.16)$$

where T_m is related to the maximum phonon frequency by $\hbar\omega_m = k_BT_m$.

Sears & Shelley in 1991 [99] computed the Debye-Waller factors for 46 elemental crystals in the periodic table with different cubic structures after determining the phonon densities of states for those elements. *Peng et al*.[100] used the Einstein model of thermal vibrations of the crystal lattice

[97, 101] to calculate the absorptive scattering factors for elemental crystals using the following equation:

$$f_{abs}(E,B,s) = \left(\frac{2h}{\beta m_0 c}\right) \int ds' f^{(e)}\left(\left|\frac{s}{2} + s'\right|\right) f^{(e)}\left(\left|\frac{s}{2} - s'\right|\right) \{1 - \exp\left[-2B\left(s'^2 - \frac{s^2}{4}\right)\right]\} \quad (5.17)$$

where $\beta = v/c$ and $f^{(e)}(s)$ is the elastic scattering factor. From equation 5.17, it is obvious that the absorptive part of the scattering factor depends on the Debye-Waller factor, accelerating voltage (E) and the scattering angle. The determination of the Debye-Waller factor is important for the computation of accurate absorptive factors of different elements. The absorptive factor reduces the scattering factors for coherent elastic scattering into Bragg reflection. The intensity removed from the Bragg reflections due to the absorptive factor is redistributed in the diffraction plane and contributes to the incoherent background. For thick crystalline samples this diffuse background between the Bragg reflections in the diffraction pattern is modulated by Kikuchi lines.

5.2 Sample Preparation

Wedge-shaped cross sectional samples were prepared by FIB to study the dependence of the HAADF-STEM signal with sample thickness. In the FIB the wedge shaped cross-sections with wedge angles between (18-24˚) were cut employing a similar process for sample preparation as described in section 1.6. The thickness of a typical wedge shaped sample is 4 μm on the thicker end and minimum on the thinner part.

For small sample thicknesses less than 100 nm the HAADF-STEM signal increases linearly with sample thickness described by $I = KFt$ where F is the fraction of electrons scattered per nm of the sample, t is the thickness and K is a pre factor. If the incident beam intensity is described by I_0 then K/I_0 represents the number of electrons transmitted through the sample onto the whole detector plane. The FIB micrograph of a wedge shaped Cu sample is shown in Figure 45.

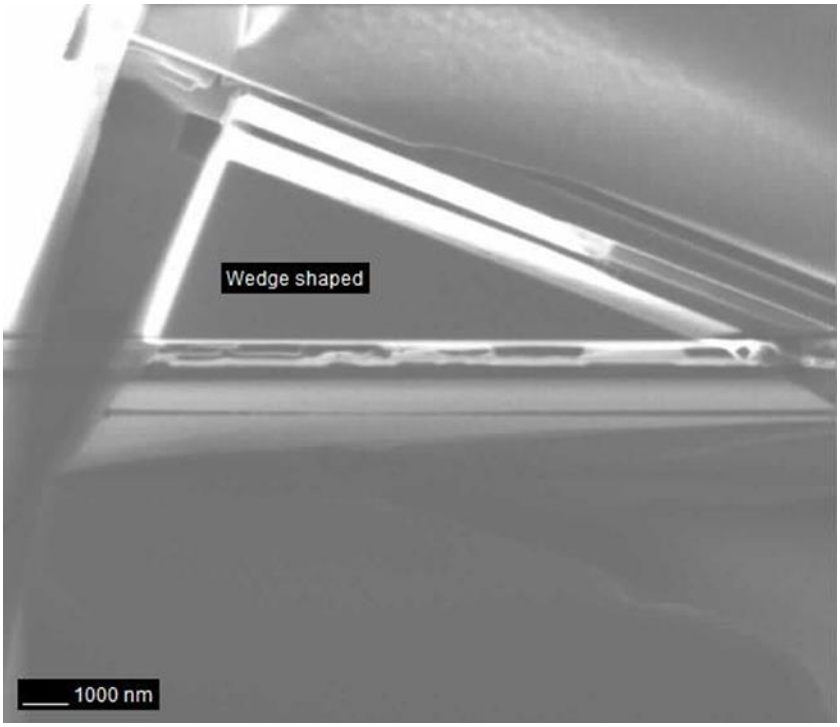

Figure 45 Wedge Shaped Cu sample prepared by FIB.

The wedge-shaped samples prepared by FIB are analyzed in the HAADF-STEM mode. The HAADF-STEM detector intensity is measured as a function of thickness for different elements in the periodic table. For these wedge-shaped samples the HAADF-STEM signal can therefore be measured directly for thicknesses ranging from 0 nm to several microns. Computational methods

thus need to cover not only the range of thin samples of a few nm or a few 10 nm, but they have to be capable to reproduce results for thick TEM samples, i.e., samples of more than a micron in thickness. This thick-sample contrast simulation requires however changes to standard simulation methods as explained in the following sections.

5.3 Differences to Standard TEM Contrast Simulation Methods

This project deals with samples that are often considered 'thick' compared to typical TEM analyses. Image contrast simulations have typically been done using the Bloch wave method [24, 102-104] and multislice methods [87, 105-109]. The Bloch wave method is used for periodic objects with a plane-wave incident electron beam. It is therefore not well suited for STEM, as the incident electron beam is convergent. Nevertheless, for each incident beam direction an independent Bloch wave simulation can be performed. The Bloch wave procedure will yield a convergent-beam electron diffraction pattern of coherently scattered electrons. The real-space image however is not available through the Bloch wave simulation with a convergent electron beam. For each incident beam direction a matrix has to be determined which contains the scattering information from one Bragg reflection to another. For HAADF-STEM several 100 electron beams have to be considered, and the eigenvectors and eigenvalues of a square matrix with several 10,000 or 100,000 elements have to to be determined. The eigenvectors represent the amplitudes of the Bloch waves, while the eigenvalues represent the wave lengths of the Bloch waves as they propagate through the periodic sample. This eigenvalue problem has to be solved for each incident beam direction separately. After transforming back from the Bloch waves to the Bragg reflections,

the intensities of Bragg reflections which are within the detector range of the HAADF-STEM detector can be added to yield a sample thickness dependent signal.

In conclusion, a Bloch wave simulation program has been written using Python, but this method has not been used for extended simulations for three different reasons:

i) it only yields diffraction space information,

ii) the process of solving an eigenvalue problem multiple times for a convergent electron beam requires significant computation time much larger than the time needed in the methods I finally used as described below,

iii) The Bloch wave method does not correctly account for thermal diffuse scattering, as only the coherent scattering contribution is calculated.

5.3.1 Multislice Simulation of TEM Micrographs

The multislice method determines the phase shift of the electron wave function as the electron wave is transmitted through a thin slice of a crystal. The local crystal potential produced by the atoms induces a local phase shift for the real-space electron wave function. However, we have to consider that electrons go through this slice at different incident angles. To account for this, the real-space wave function after being transmitted through a slice is Fourier transformed. The Fourier transform yields the wave function of electrons in the diffraction plane. A Fresnel propagator, $\mathcal{L} = \frac{t}{\cos 2\theta}$ (Figure 49) is introduced to account for the additional path length of those electrons which are inclined to the slice normal. Then a back Fourier transform is performed to obtain the modified real-space wave function again. This procedure is repeated for as many slices

as needed. The multislice method yields both an accurate diffraction pattern as well as a real space image. A schematic of the classical multislice method is given below in Figure 46.

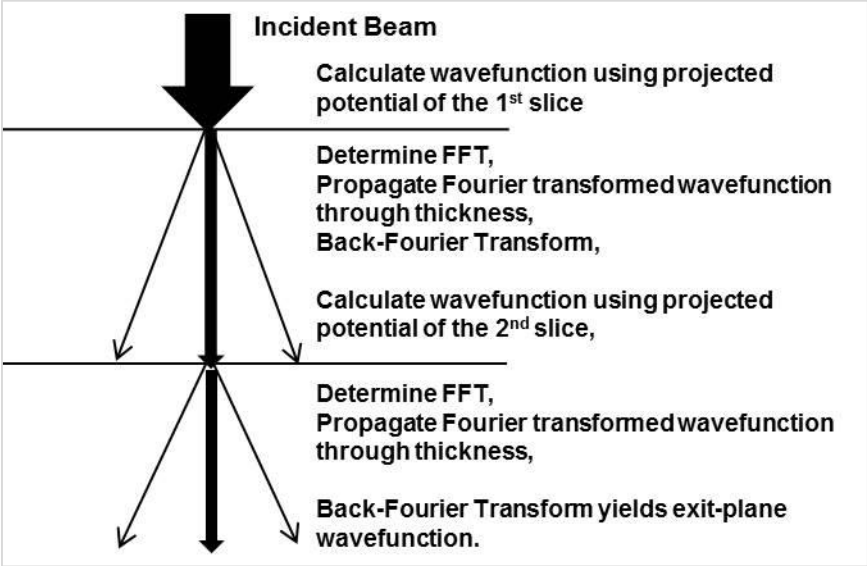

Figure 46 Schematic of the multislice method with two slices.

However, this classical multislice method becomes impractical for large sample thicknesses as explained below. To account for the Debye-Waller factor and the atomic displacements through thermal vibrations a 'frozen phonon' [110-112] approach is made. In each slice the atoms are displaced slightly so that the atomic displacements represent a snapshot in time for the thermal displacement. For each of those snapshots a full multislice simulation is performed and the resulting electron wave functions are summed up for all snapshots at all points in the diffraction plane and all points in the imaging plane.

The multislice method operates with wave functions which are correctly represented both in real as in reciprocal space if a sufficiently high number of 'frozen phonon' snapshots are used in the simulation.

5.3.2 Why not Multislice for Thick TEM Samples

The classical multislice method described in section 5.3.1 is not suitable for simulations of thick TEM samples. From Bragg's diffraction condition it follows:

$$2dSin\theta = \lambda \tag{5.18}$$

$$q_{max} = \frac{1}{d} \approx \frac{2\theta_{max}}{\lambda} \approx \frac{1}{4} pm^{-1}$$

where $2\theta_{max} = 460\, mrad$ is the maximum scattering angle, $\lambda = 2\, pm$ for 300 keV electrons used for this project and $v_{max} = w/2$ is half the frame size in dimensions as shown in the schematic below.

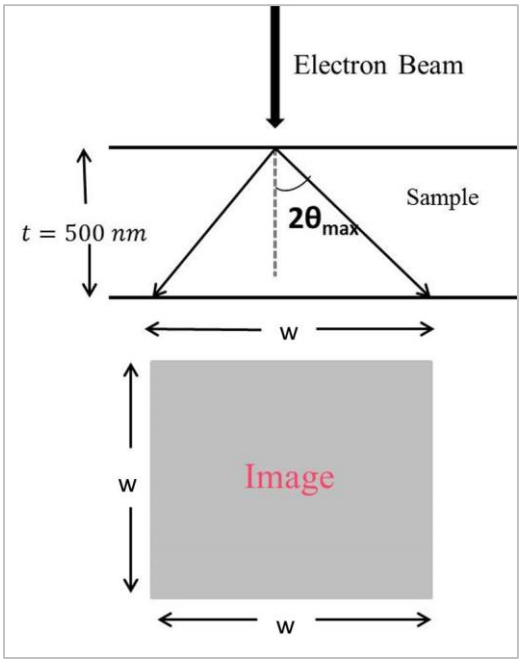

Figure 47 Schematic showing the frame size required for multislice simulations.

The pixel size in real space required for each frame for multislice simulations is $\frac{1}{2q_{max}} \approx 2\, pm$. The frame size as shown in Figure 47 for a sample thickness of 500 nm $is\ w \approx 4\theta_{max} t \approx 550\, nm$.

Thus, the number of pixels in each x and y dimension required to construct an image would be 275, 000. This means that for such multislice simulations of a 500 nm thick sample we would need at least a frame size of 2^{17} x 2^{17} for which Fourier forward and backward transformations have to be made repeatedly through the multislice process. With todays' computational capabilities, this is even impractical for large clusters like the Stokes system at UCF. These simulations need high computing power and are extremely time consuming, especially considering that the frame size needs to be increased proportional to the sample thickness. This classical multislice approach was therefore not followed. A different algorithm needed to be developed to perform efficient and reliable simulations of the HAADF-STEM contrast of thick TEM samples.

5.3.3 Modified Multislice Method for TEM Simulations

I here propose a modification of the multislice method. This modification deals with intensities of scattered electrons instead of wave functions. The crystal structure with discrete atomic positions is replaced with atomic densities without any specific atomic positions. Therefore, in the diffraction plane we cannot expect a diffraction pattern with diffraction spots or Debye-Scherrer rings. Instead, a radially symmetric intensity distribution will form. For each slice the scattering from each beam direction to each other beam direction is determined using the corresponding scattering cross sections.

This can be done by Fourier transforming the electron intensity in the diffraction plane and the angle-dependent scattering cross section [113]. In other words, a convolution of the electron intensity in the diffraction plane and the scattering cross section is performed. After multiplying these two Fourier transforms the result will be back Fourier transformed and multiplied with a

Fresnel propagator accounting for increased scattering if electrons have a longer path length as they are inclined to the slice normal.

$$\overrightarrow{b'}(k') = \vec{b}(k)[1 - \mathcal{L}(k)\sum_{k \neq k'} q(k' - k)] + \mathcal{F}^{-1}[\mathcal{F}(b(k) * \mathcal{L}(k'))\mathcal{F}(q)] \quad (5.19)$$

Here $\vec{b}(k)$ represents the initial electron beam having a wave vector k. The final electron beam $\overrightarrow{b'}(k')$ having a wave vector k' is calculated from the above equation for each slice thickness of the material. $\mathcal{F}$ and $\mathcal{F}^{-1}$ represent the Fourier transform and Inverse Fourier transforms.

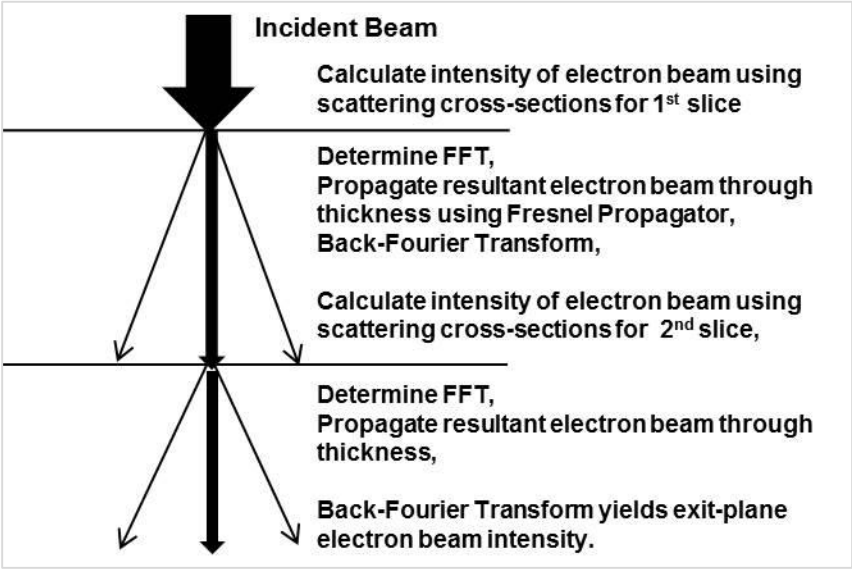

Figure 48 Schematic of the modified multislice method using intensities of scattered electrons.

The Fourier transform of the electron intensity in the diffraction plane however does not represent a real-space image of the electron intensity distribution. This modified multislice method therefore does not yield image information in real space. The schematic of the modified multislice method is shown in Figure 48.

It yields only a HAADF-STEM intensity of a uniform material as a function of thickness, independent of any specific crystal orientation. This modification is thus an approximation where crystal orientation effects are neglected.

5.4 Python Algorithm for Modified Multislice Method

To study the HAADF-STEM signal as a function of sample thickness a programming code was scripted using Python 3.2. Python was chosen as it allows programmers to express concepts in fewer lines of code than other languages such as C. A couple years ago, Candy Reid, an undergraduate Physics student at UCF, developed some initial code for calculation of electron scattering cross sections using Python during a semester of research. Only small parts of the current programs developed for this dissertation are still based on Ms. Reid's subroutines. Also due to its strong library, Python was preferred to other languages. Equation 5.13 can be written in the following form:

$$f^e(s) = 0.04787 \sum_{i=1}^{5} a_i \exp(-b_i s^2) \qquad (5.20)$$

As the electron beam hits the sample, the incident electrons interact with the electrons and nuclei of the material and undergo multiple scattering events. The main procedure starts by considering very thin slices of the material (1-10) nm and calculating the initial electron beam intensity ($b(k)$) after it passes through a sample slice. Electrons would be scattered at both lower and higher angles but the HAADF-STEM detector only collects electrons scattered between an angular range of (80-460) mrad. The algorithm has been developed using a centered intensity distribution, i.e., the

incident beam is centered in the field of the diffraction and image plane. The scattered intensity at any point on the grid (512 x 512 pixels) has been computed by $S(x,y) = |(f^e)^2 - (f_{abs})^2|$, where f^e and f_{abs} are the elastic and absorptive scattering factors computed from equation 5.10 and 5.16, using the coefficients from *Peng et al*.[100].

The schematic in Figure 49 shows an incident electron beam scattered at an angle 2θ traversing through a material thickness t, where the lateral dimension is of n pixels. The Fresnel propagator, $\mathcal{L} = \frac{t}{\cos 2\theta}$ accounts for the additional path length for those electrons which are inclined to the slice as shown in Figure 49.

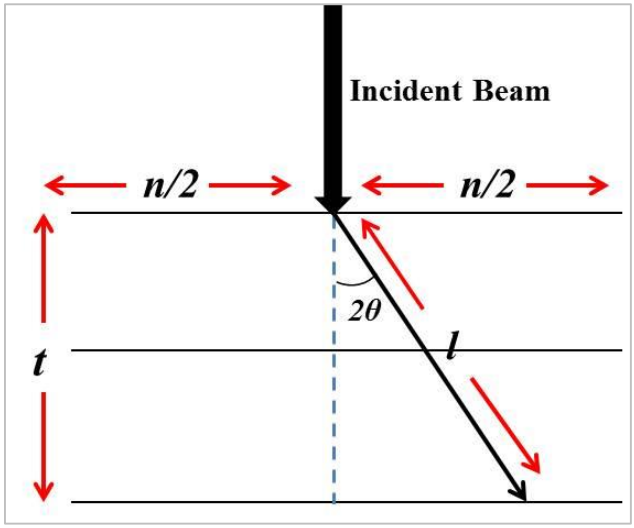

Figure 49 Schematic showing the path for electrons inclined to the thickness slice.

The fraction of electrons scattered for each slice with atomic density ρ and thickness t from an wave vector k into wave vector k' is given by:

$$\sum_{k \neq k'} q(k' - k) = \rho\sigma(k' - k)dkdkt \quad (5.21)$$

From equation (5.20) it follows that the total scattering from a thickness t and a material with atomic density ρ is given by:

$$f_{total}^{b} = (\frac{2\pi m_0 q\gamma}{h^2} f^e)^2 t\rho(d\theta)^2 \quad (5.22)$$

where m_0 is the rest mass of an electron,$V = 300\ keV$, $\gamma = 1 + \frac{eV}{m_0 c^2}$ is the relativistic correction and $\frac{2\pi\gamma mq}{h^2} = 3.317 * 10^{18}$.

The beam intensity $\overrightarrow{b'}(k')$ after traversing a slice of thickness t for each beam direction k is computed by considering the beam $\vec{b}(k)$ before it enters this slice and modifying it by adding the intensity scattered into the beam direction k' and subtracting the intensity scattered away from k' as shown in equation 5.19. The total intensity on the HAADF-STEM detector is calculated by integrating the the beam intensity over the detector range.

5.5 Python Simulations

Figure 50 shows the comparison for the HAADF-STEM detector signal for a wedge-shaped tungsten sample from experiment and simulation using equation 5.19 where elastic and absorptive coefficients from *Peng et al*. have been used [2, 100] .

Both the simulation and experimental curves exhibit similar behaviors with an initial increase in the detector signal as the thickness of the sample increases. A maximum detector count is recorded at 250 nm thickness for the experimental measurement while the maximum for the simulated signal is found to be at 175 nm. As the thickness increases we observe an exponential decrease in the HAADF-STEM signal for the in experiment.

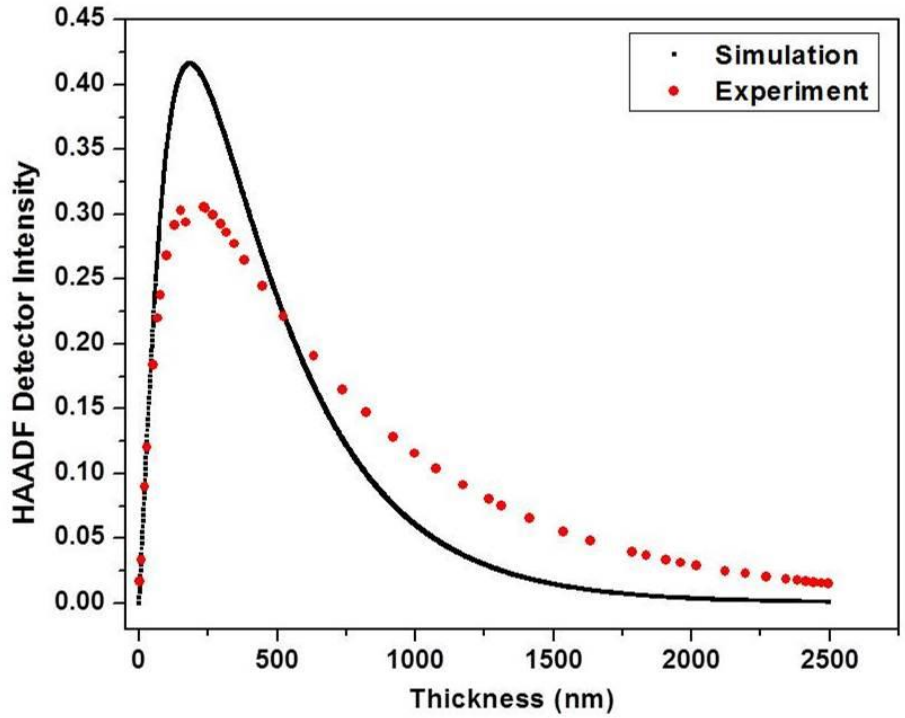

Figure 50 HAADF-STEM intensity vs thickness of wedge shaped W for both experiment and simulations using *Peng et al*. elastic & absorptive parameters.

In contrast the simulation curve falls faster than the experimental curve and the simulated signal almost becomes zero as the thickness of the sample increases to 2.5 μm.

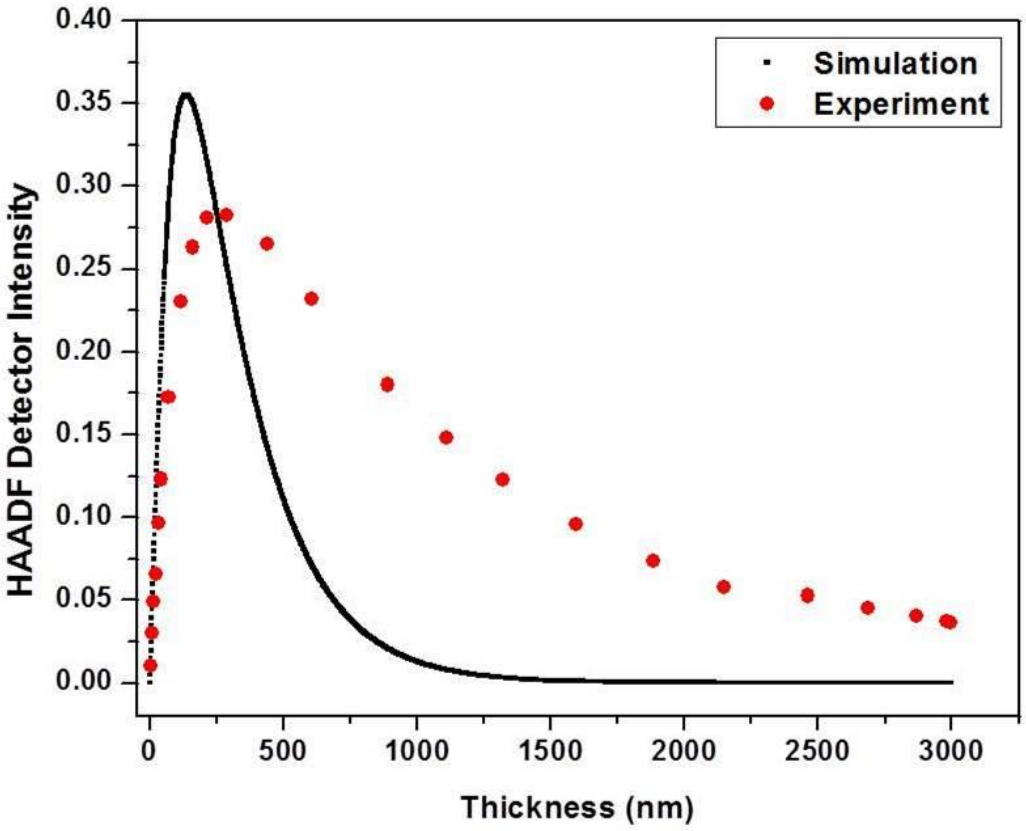

Figure 51 HAADF-STEM intensity vs thickness of wedge shaped Pt for both experiment and simulation using *Peng et al*. elastic & absorptive parameters.

A wedge shaped FIB sample for Platinum was prepared to measure the HAADF-STEM intensity with increasing thickness. In Figure 51 a comparison of the experimental and simulated values for Platinum for sample thicknesses up to 3 μm is shown. Here, the simulated values of HAADF signal fall rapidly and reach zero at around 1 μm while the experimental curve shows a slow and steady drop of HAADF-STEM intensity up to 3 μm of sample thickness. The maximum simulated intensity for the wedge-shaped Pt sample is at 100 nm while that for the experimental results it is at 280 nm.

The above differences in the HAADF-STEM detector intensity can be explained by considering a number of factors which play an important role in electron diffraction:

A fully quantitative analysis of absorption is very difficult. In principle all the possible excitation processes (phonons, plasmons, single-electron transitions, etc) which scatter electrons out of the Bragg reflections into the background need to be considered [97]. Thus the atomic potentials cannot be constructed from individual atomic contributions. Also, the solid state nature of every element needs to be implemented quantify the plasmon losses and the core excitations. The simplistic Einstein model used by early groups [96, 97] assumes that each atom vibrates independently of the others and considers TDS as the most significant process for attenuation of the reflections. This probably causes a variation in the signal of HAADF-STEM intensity at greater thicknesses where the TDS dominates at higher scattering angles. The Debye model is strictly applicable only for cubic lattices with one atom per primitive unit cell and it fails at higher temperatures [100]. Here absorbed electrons are those which stop inside the material after losing sufficient energy due to multiple scattering events. These electrons are considered not to enter the detection channel of the electron microscope. But absorbed electrons can reenter the detection channel after gaining energy due to other excitation processes and this phenomenon have not being accounted for in our algorithm.

At this point, it is worth discussing the meaning of the term ‘absorptive factors’ here. Absorbed electrons are those which stop inside the material after losing sufficient energy due to multiple inelastic scattering events. These electrons are considered not to enter the detection channel of the electron microscope. The term ‘absorbed electron’ for these electron lost to any detection process

is distinct from electrons which are not anymore coherently scattered into Bragg reflections. The paper by *Peng et al.* [100] deals with electrons only which get removed from the coherent scattering channels. However, in the current HAADF-STEM experiments these electrons are to a large part still detected as they constitute the diffuse background between Bragg reflections in the diffraction plane.

This difference in the meaning of 'absorption' prevents a useful application of absorptive factors of elements as described by *Peng et al*.[100], and thus the Debye model used here gives inaccurate results for most elements.

A simpler approach can be used to determine the absorptive scattering factors of different elements based on the following principles:

1. The HAADF-STEM intensity increases linearly with thickness for thin samples, given by $I = KFt$ [17].where F is the fraction of electrons scattered per nanometer of sample thickness (*t*).
2. At higher sample thicknesses the electrons undergo multiple scattering events and the HAADF-STEM intensity would reach a saturation value, if we had no absorption which can be represented in the form of$I = \frac{K}{I_0}[1 - \exp(-Ft)]$. Here K is a prefactor and K/I_0 represents the fraction of electrons passing through the sample and reaching the detector plane and I_0 is the initial beam intensity represented by $\vec{b}(k')$ in equation 5.19.
3. The modified multislice algorithm uses only the elastic potential coefficients as described by *Peng et al*. [2]. We have to introduce a single absorption parameter (μ) (specific to a material) in our algorithm which accounts for the absorption (electrons lost to any

detection) with increasing thickness. We also neglect f_{abs} as computed by *Peng et al*.[100]. The final thickness dependent HAADF-STEM intensity can be written as:

$$\frac{I}{I_0} = \frac{K}{I_0}[(1 - \exp(-\mathrm{Ft}))\exp(-\mu t)] \quad (5.23)$$

4. μ is determined from the simulation which match closely with the experimental plots. Values of μ for different elements are given in Table 1. I found no literature values from first principles calculations for these absorption parameters, so only matching to experimental data was used for determine the absorption parameters.

To determine one of these element specific absorption parameters, a wedge shaped sample of Fe was prepared and the HAADF-STEM signal was measured. HAADF signal was also computed using the modified multislice program described in section 6.3.3.

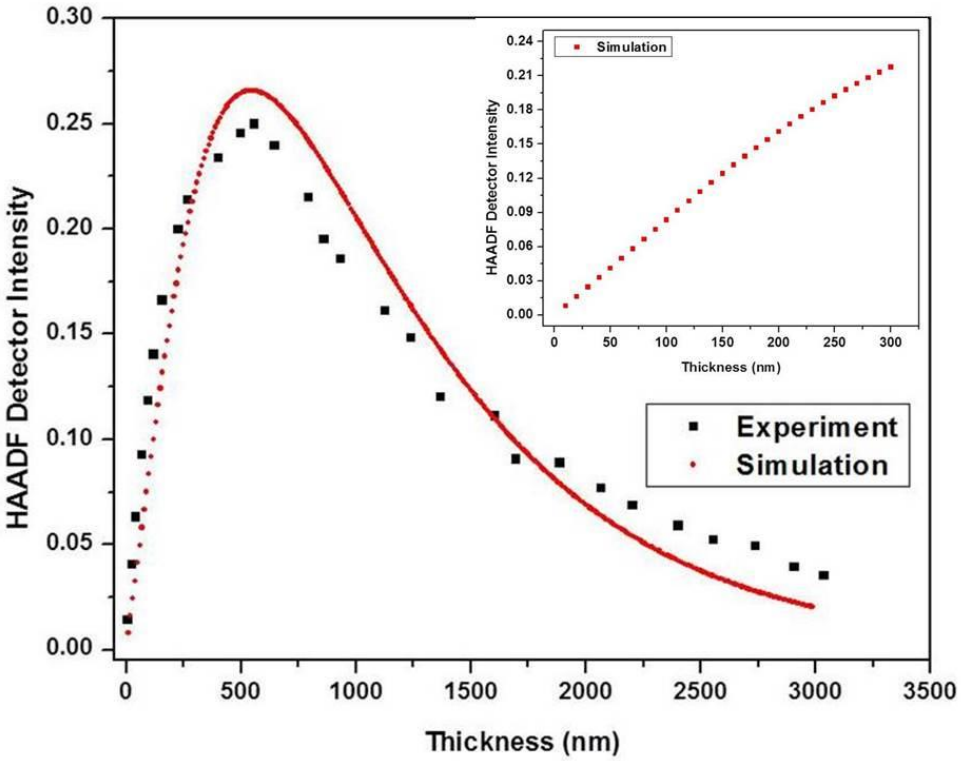

Figure 52 HAADF-STEM intensity vs thickness of wedge shaped Fe for both experiment and simulation using the modified multislice method. The inset shows the initial slope from the simulated curve.

Figure 52 shows the comparison of measured experimental values and simulated values of HAADF-STEM intensity for Fe sample for increasing thickness. Inset in Figure 52 shows the initial slope of the HAADF signal for simulated values.

The absorption parameter $\mu = (1.0 \pm 0.2) * 10^{-4}\text{nm}^{-1}$ is calculated from the best fit of multiple simulations to the experiment. The initial slope of the simulated curve in Figure 52, $\varepsilon = (1.12 \pm 0.08) * 10^{-3}\text{nm}^{-1}$and $F = (8.4 \pm 1.1) * 10^{-4}\text{nm}^{-1}$(Appendix II).

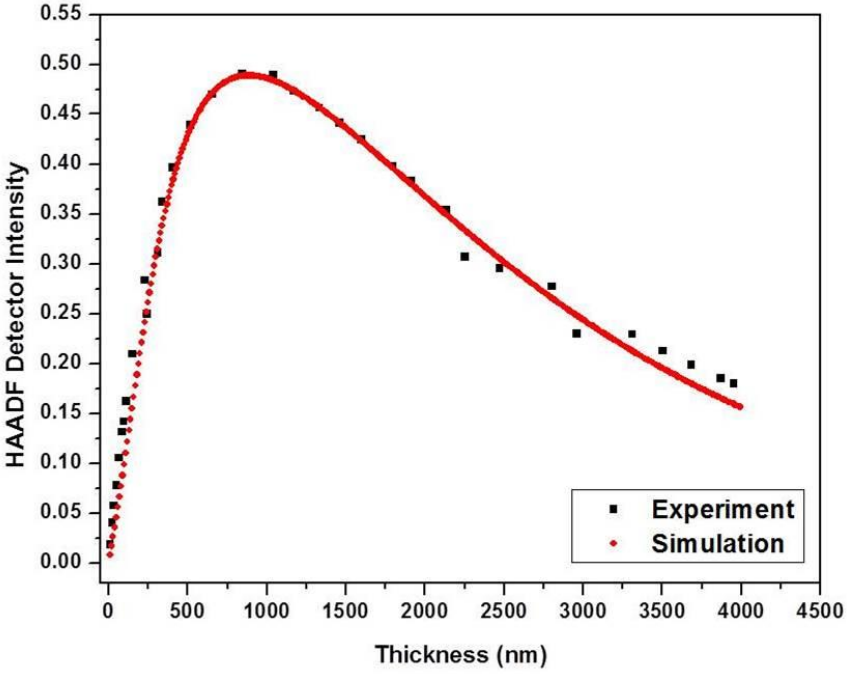

Figure 53 HAADF-STEM intensity of a wedge shaped Cu sample for experiment and simulation.

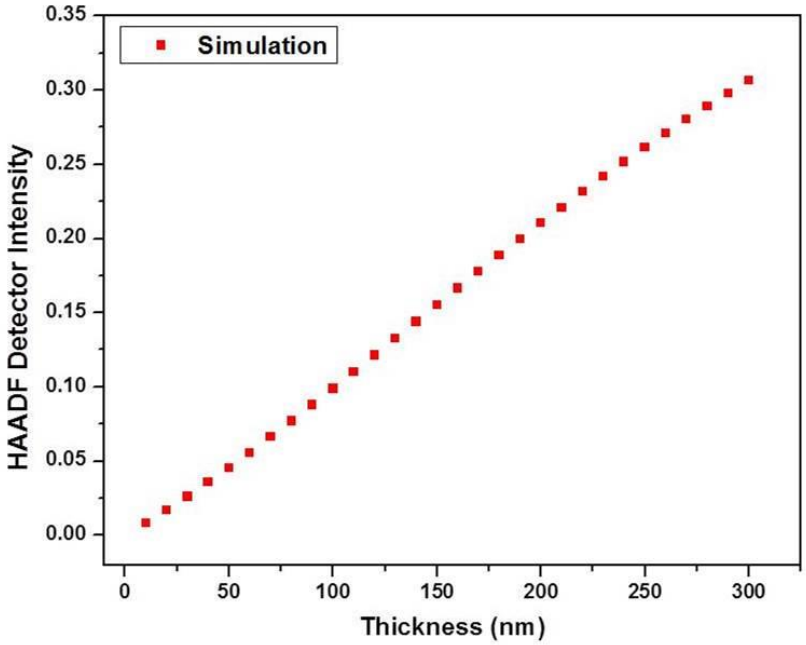

Figure 54 Initial slope of simulated curve for the Cu sample using the modified multislice method.

Figure 53 shows the HAADF-STEM intensity vs. the thickness of the Cu sample obtained from experiments and simulations. The HAADF signal increases with thickness and reaches a maximum at around 850 nm. Less absorption is seen in Cu as the HAADF signal falls off slowly up to 4 μm. The absorption parameter determined from the best fit to simulation curve is $\mu = (4.6 \pm 0.04) * 10^{-4}\text{nm}^{-1}$. The initial slope ε calculated from simulations is $(1.11\pm0.11)*10^{-3}\text{nm}^{-1}$ (Appendix II) and $F = (1.53 \pm 0.02) * 10^{-3}\text{nm}^{-1}$. From Figure 53 we see that the simulated curve matches well with the experimental curve. Small deviations arise from the surface roughness and ion implantation of the wedge shaped sample due to back deposition of gallium from FIB processing. The simulations and experiment also confirm the qualitative model described in equation 5.19 for the thickness dependence of the HAADF-STEM intensity.

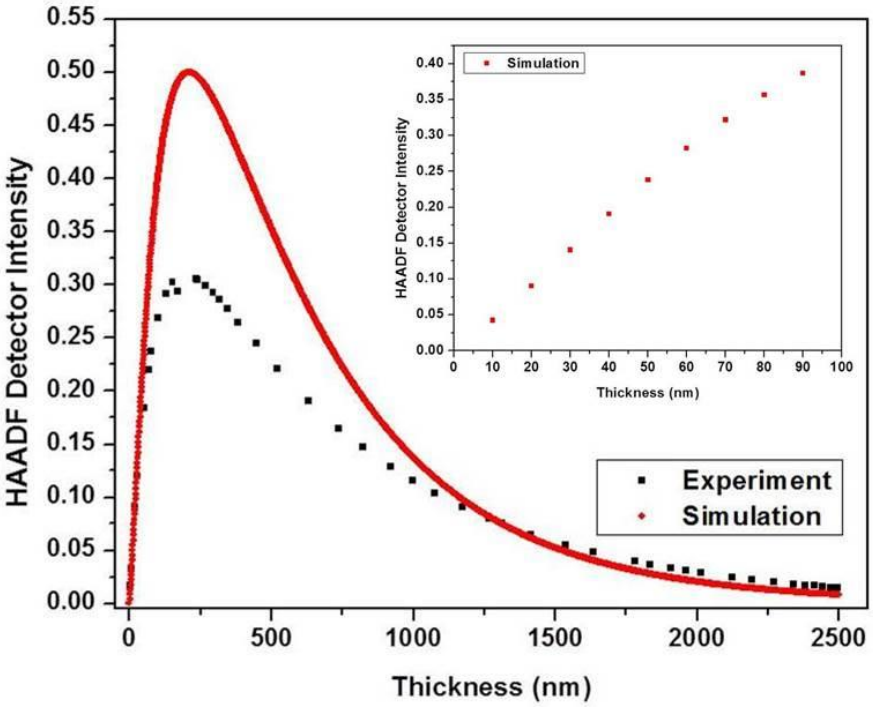

Figure 55 HAADF intensity of wedge shaped W vs. thickness for both experiment and simulations. Inset is the initial slope of the simulated curve.

Attempts were made to measure the HAADF intensity for elements with higher atomic number. Figure 55 shows the HAADF-STEM intensity for W with increasing thickness. The experimental and simulation curve do not match well for tungsten.

Simulations with the modified multislice method of W produce peak HAADF intensity almost 1.5 times that of the experimental value. One reason for the mismatch of experimental and simulation curve in Figure 55 may be due to the heterogeneity of sensitivity of the HAADF-STEM detector. The profile of the detector sensitivity is shown in Figure 56. The inset in the Figure 56 shows the HAADF-STEM detector along with the profile scan direction.

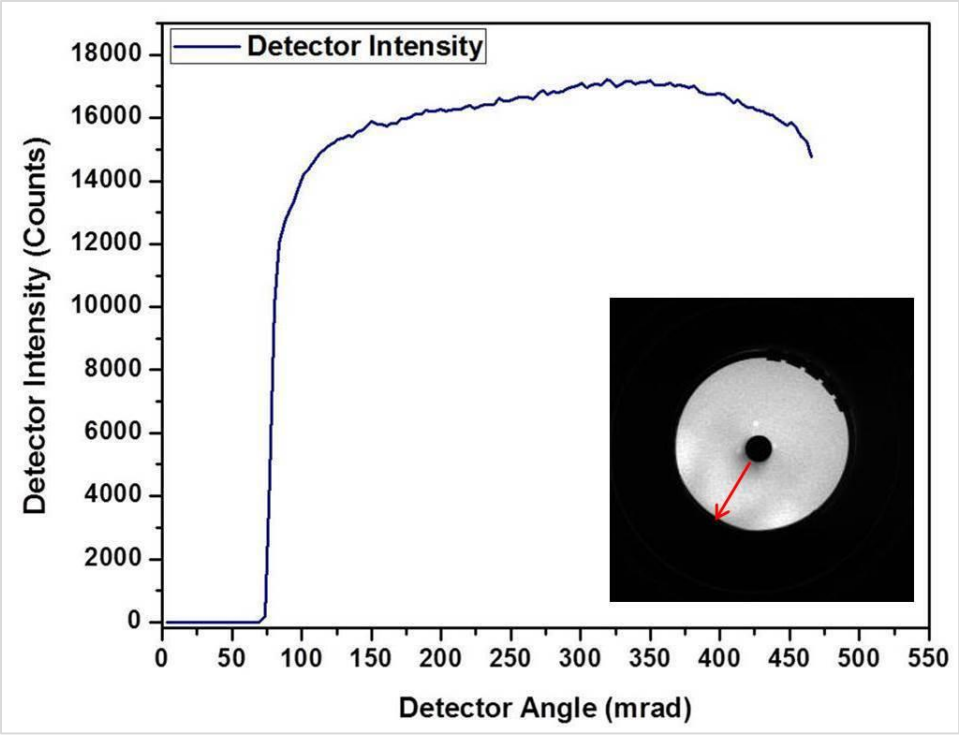

Figure 56 Profile scan of HAADF-STEM detector.

The line profile scan of the HAADF-STEM detector from the inner radius to outer radius shows a variation in counts from 12000 to 16000 as shown in Figure 56. The difference in sensitivity of the detector at certain places produces a lower HAADF-STEM signal especially near the inner radius of the detector, i.e., at low angles where the electron intensity is highest. This may be one of the reasons for the difference between the experimental and simulated curve.

The absorption parameter, $\mu = (2.11 \pm 0.02) * 10^{-3}$nm^{-1}and the initial slope ε measured from Figure 55 is (4.3±0.5)*10^{-3}nm^{-1}.

The corresponding HAADF-STEM intensity for Pt with increasing thickness is shown in Figure 57. The sample was provided by Dr. Bo Yao and consists of six Fe and six Pt layers on a SiO_2 layer on a Si substrate [75, 114].

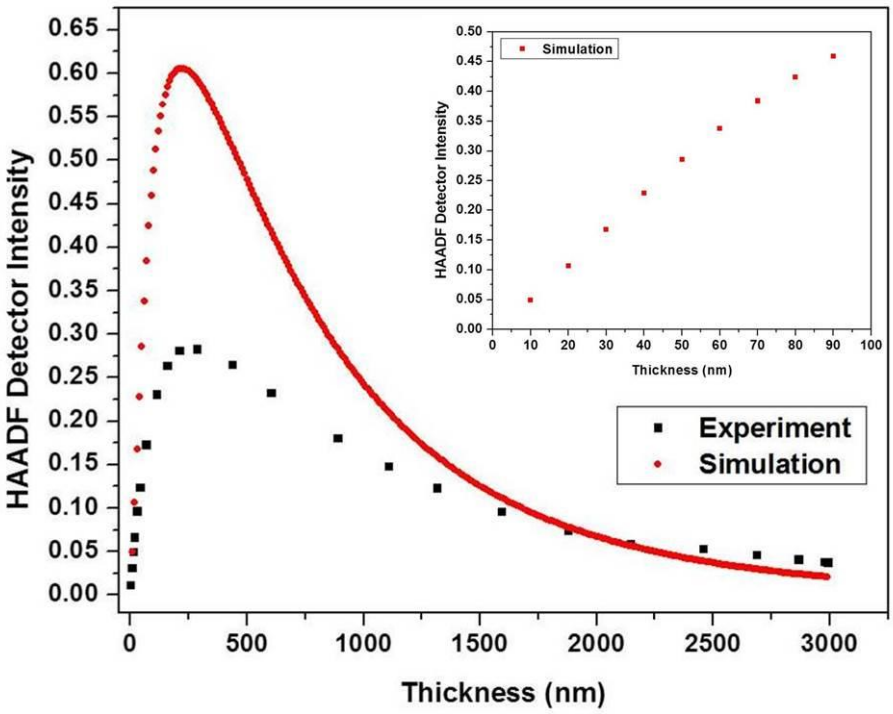

Figure 57 HAADF intensity of wedge shaped Pt vs. thickness for both experiment and simulations. The inset shows the initial slope of the simulated curve.

The initial slope (ε) calculated from the simulation curve is (4.85±0.37)*$10^{-3}$$nm^{-1}$ and the absorption parameter is $\mu = (1.34 \pm 0.04) * 10^{-3}$$nm^{-1}$as determined from the best fit (Appendix II).

The results from simulation does not match with the experiments as in the case of W. The peak HAADF detector signal from the simulations is twice that of the experimental value but the trend of both the simulation and experimental curve is quite similar at higher sample thicknesses as shown in Figure 57.

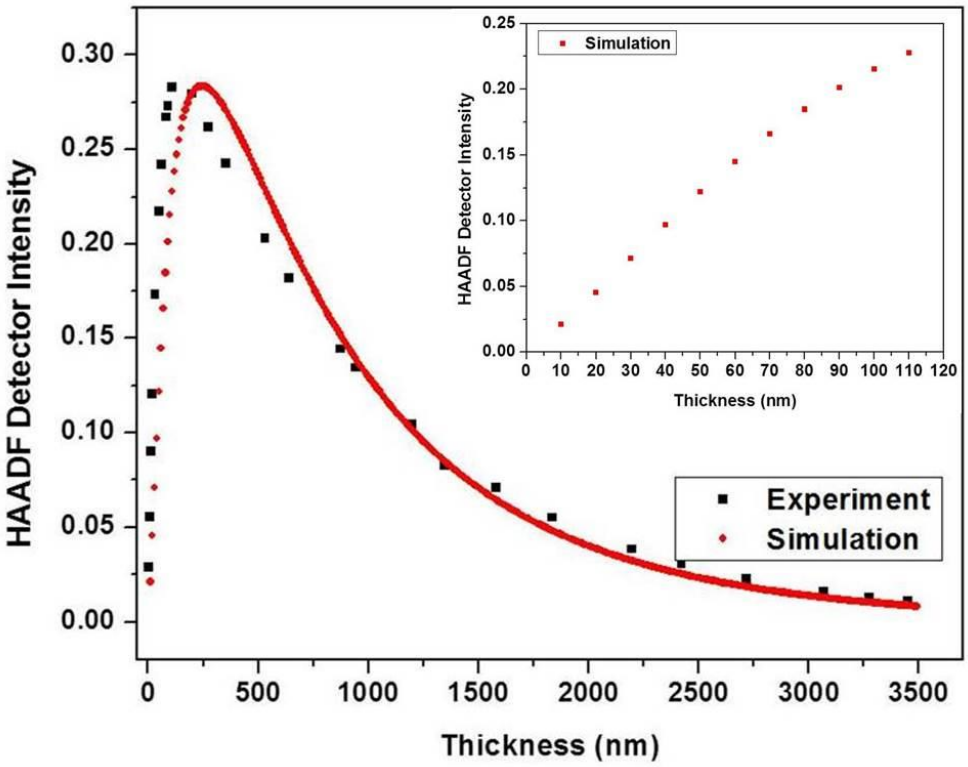

Figure 58 HAADF intensity of wedge shaped Au vs. thickness for both experiment and simulations. The inset shows the initial slope of the simulated curve.

As shown in Figure 58 the peak HAADF signal for the simulation curve is at 250 nm thickness as compared to the experimental curve which is at 115 nm thickness. The difference can be accounted for as in the FIB processing we always don't get a perfect wedge sample and also in the preparation of thick samples gallium back deposition plays a major role. Initial slope of $\varepsilon = (2.19 \pm 0.21) * 10^{-3}\text{nm}^{-1}$ and absorption parameter $\mu = (1.21 \pm 0.01) * 10^{-3}\text{nm}^{-1}$is calculated from the best fit to the simulated curve (Appendix II).

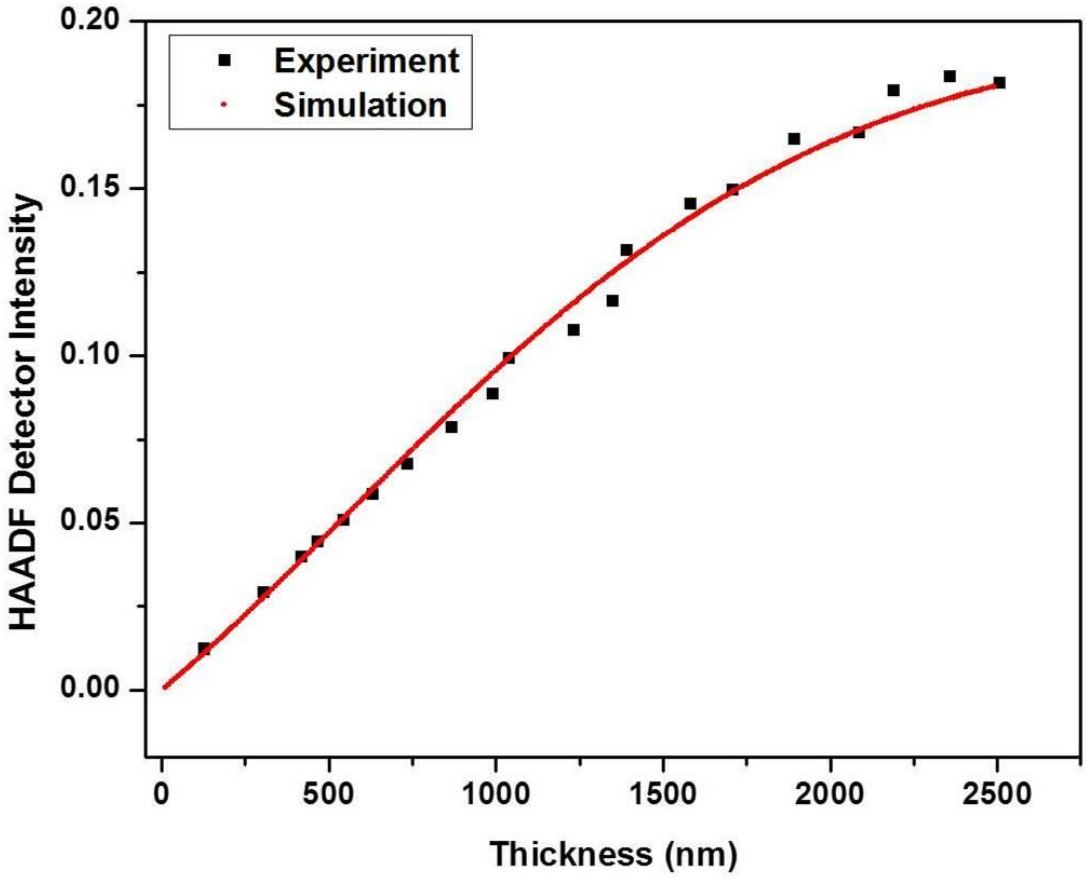

Figure 59 HAADF intensity of wedge shaped Al vs. thickness for both experiment and simulations. The inset shows the the initial slope of the simulated curve.

The HAADF detector signal behavior for a wedge shaped sample of Al has been shown in Figure 59. Initial slope is $\varepsilon = (9.6 \pm 1.0) * 10^{-5}$nm^{-1}as determined from the simulated curve. For a sample thickness of 2.5 μm we see very little absorption as a result of less scattering of electrons. Thus to determine the absorption parameter μ, thicker samples needs to be studied which is difficult to prepare using the FIB. Thus the absorption parameter $\mu = (1.06 \pm 0.28) * 10^{-4}$nm^{-1}for Al may not be an accurate determination.

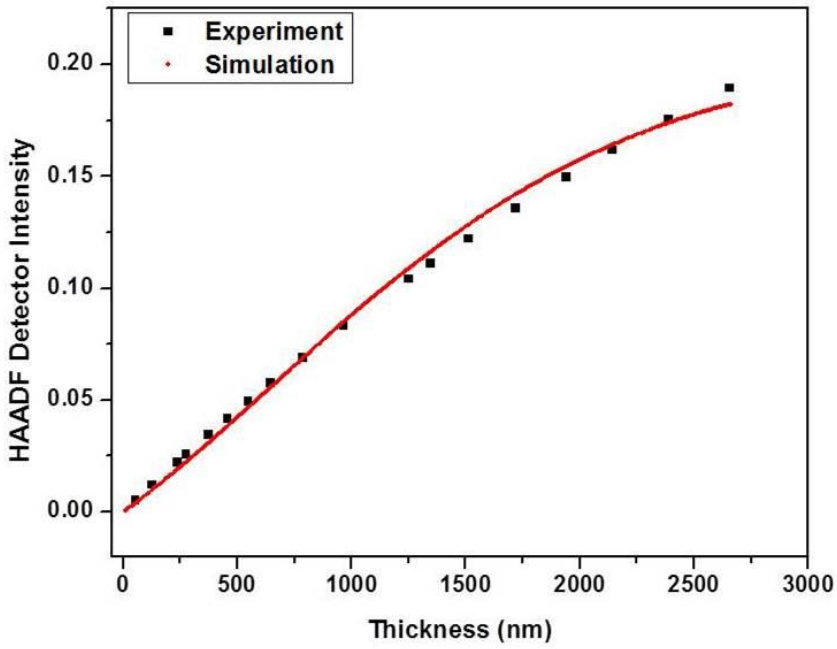

Figure 60 HAADF intensity of wedge shaped Al vs. thickness for both experiment and simulations. The inset shows the initial slope of the simulated curve.

The HAADF detector intensity vs thickness behavior for wedge shaped sample in Si (Z=14) is similar to that of Al (Z=13). From Figure 60, the initial slope of the simulation curve was

determined to be $\varepsilon = (8.1 \pm 0.6) * 10^{-5}\text{nm}^{-1}$ which signifies low absorption ($\mu = (8.6 \pm 2.7) * 10^{-5}\text{nm}^{-1}$) in silicon.

It can be concluded that electrons get scattered more in elements with higher atomic number than that in lower atomic number as confirmed from the simulations. For elements with higher Z, the number of electrons in the core shells surrounding the nuclei increases and thus the incident electrons suffer multiple scattering as it transmits through each slice of the material. Electrons which are scattered at higher angles are scattered back to enter the detection channel of the TEM, thus causing less absorption. Table 1 represents the fitting parameters from both the simulations and the experiment. The simulated curve fits are shown in Appendix II.

Table 1 HAADF-STEM fitting parameters for wedge shaped samples from modified multislice simulations

Material	**Z**	**F(nm^{-1})**	**K/I_0**	**μ(nm^{-1})**	**ε(nm^{-1})**
Al	13	$(1.16\pm0.29)*10^{-4}$	0.96	$(1.06\pm0.28)* 10^{-4}$	$(9.6\pm1.0) * 10^{-5}$
Si	14	$(1.0\pm0.12)*10^{-4}$	0.97	$(8.6\pm2.7)* 10^{-5}$	$(8.1\pm0.6) * 10^{-5}$
Fe	26	$(8.4\pm1.1)*10^{-4}$	0.92	$(1.02\pm0.2)*10^{-4}$	$(1.12\pm0.8) * 10^{-3}$
Cu	29	$(1.53\pm0.02)*10^{-3}$	0.97	$(4.6\pm0.04)*10^{-4}$	$(1.11\pm0.11) * 10^{-3}$
W	74	$(6.98\pm0.08)*10^{-3}$	0.98	$(2.11\pm0.02)*10^{-3}$	$(4.3\pm0.5) * 10^{-3}$
Pt	78	$(8.6\pm0.07)*10^{-3}$	0.94	$(1.34\pm0.04)*10^{-3}$	$(4.85\pm0.37) * 10^{-3}$
Au	79	$(7.88\pm0.06)*10^{-3}$	0.91	$(1.21\pm0.01)*10^{-3}$	$(2.19\pm0.21) * 10^{-3}$

Table 2 shows the experimental values for the wedge shaped samples taken from dissertation of Biao Yuan [90]. A noted difference is observed in the values of K/I_0 between the experiments and simulations. A higher value of K/I_0 indicates that more electrons reach the HAADF detector plane

unabsorbed. This in turn should increase the HAADF signal (as shown in Pt and W). But again the solid state structure and other factors are ignored in the simulations which can alter the HAADF intensity. The absorption parameter (μ) should increase with the increase in atomic number which is true for the simulated values. μ values for Fe and Cu are comparable, whereas elements of higher atomic number (W, Pt and Au) have absorption parameters in the same order.

Table 2 HAADF-STEM fitting parameters for wedge shaped samples from experiments [90]

Material	**Z**	**F(nm^{-1})**	**K/I_0**	**μ(nm^{-1})**	**ε(nm^{-1})**
Al	13	$2.2*10^{-4}$	0.45	-	$9.9*10^{-5}$
Si	14	$2.5*10^{-4}$	0.40	$2.4*10^{-4}$	$1.0*10^{-4}$
Fe	26	$4.0*10^{-5}$	0.40	$8.0*10^{-4}$	$6.1*10^{-4}$
Cu	29	$2.1*10^{-4}$	0.81	$3.8*10^{-4}$	$1.1*10^{-3}$
W	74	$1.14*10^{-3}$	0.45	$1.37*10^{-4}$	$3.0*10^{-3}$
Pt	78	$8.8*10^{-4}$	0.40	$9.0*10^{-4}$	$3.0*10^{-3}$
Au	79	$2.2*10^{-2}$	0.35	$1.0*10^{-3}$	$1.0*10^{-3}$

From simulations, the fraction of scattered electrons per nm (F) can be seen increasing with increasing atomic number. Atoms of higher atomic number elements scatter more due to their greater atomic mass. This justifies the F values determined from the simulations. Also the initial slope increase with increase in atomic number which is depicted from both experiments and simulations. While an exact determination of the HAADF-STEM intensity behavior is very

difficult as has been discussed earlier, but both experiments and simulations provide us a better understanding of the physical phenomena.

CHAPTER 6: INTERFACIAL ATOMIC NUMBER CONTRAST IN THICK TEM SAMPLES

Using a single or dual beam FIB to prepare cross-sections for TEM sometimes produces thick samples. Thick samples reveal an increase in intensity at the interfaces of high and low density materials when using an HAADF-STEM detector.

Figure 61 shows a HAADF-STEM micrograph of a multilayered sample provided by TQS, Apopka, FL. The sample consists of a Ti layer on top of an Au layer. The interface between the Au and Ti layer shows an increase in intensity with bright lines appearing near the interface. A similar bright line is visible in Figure 61 at the interface between Ti and $LiTaO_3$. Figure 62 shows the corresponding profile scan from the Au to the Ti layer.

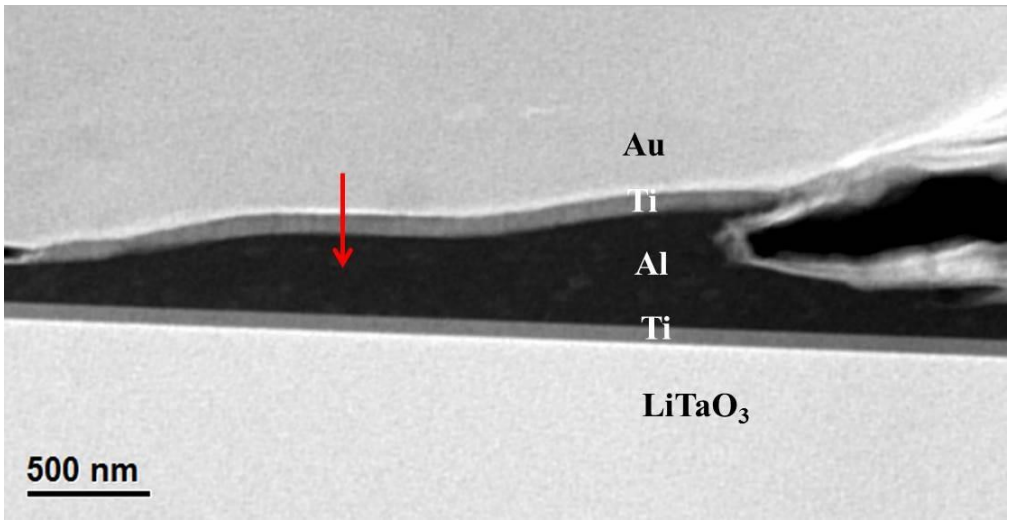

Figure 61 HAADF-STEM micrograph of multilayered sample provided by TriQuint Semiconductors, Inc. Red arrow showing the profile scan direction from Au to Ti Layer.

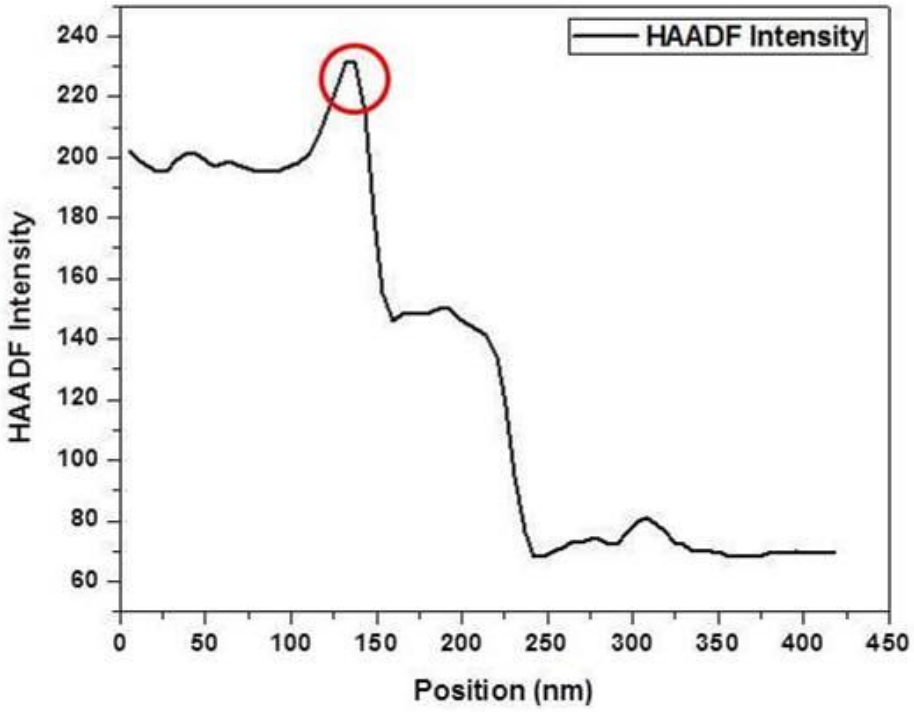

Figure 62 Profile scan showing increase of signal near the interface of Au & Ti. Left: Au, middle: Ti, right: Al.

The profile scan reveals an increase in intensity (marked by red circle in Figure 62) just near the Au and Ti interface. Intuitively, one would assume that there is a higher density material between Au and Ti as the HAADF-STEM signal increases with increasing atomic number. Au being a higher density material than Ti, the above effect has however to be explained by the specifics of scattering of electrons near the interface, as EDS measurements do not reveal any other element between Au and Ti. A local higher density of Au can also be excluded, as Au does not form any compound with Ti that has a significantly higher atomic density.

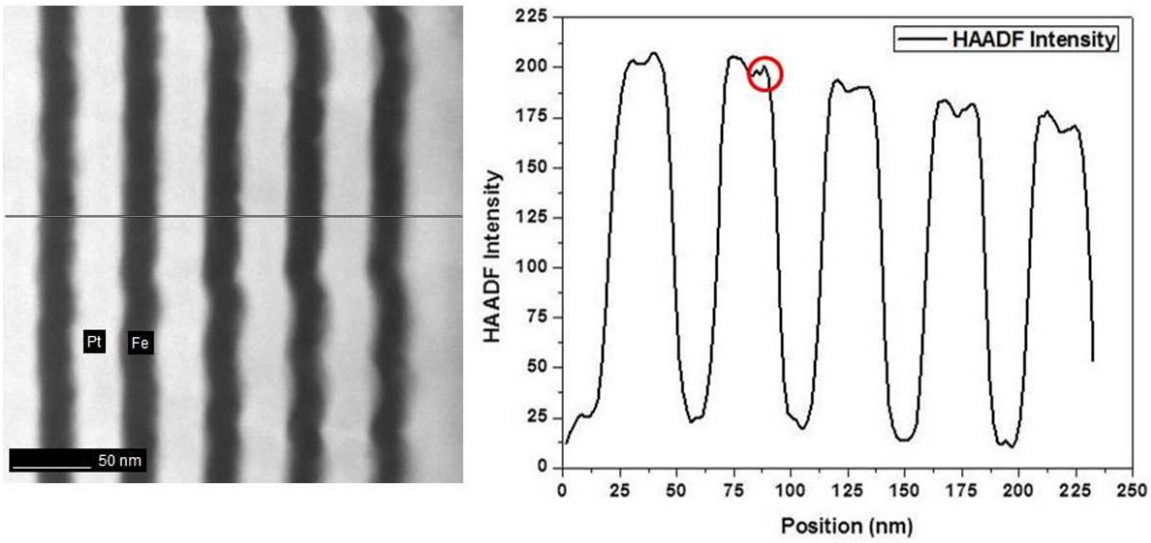

Figure 63 (Left) HAADF STEM micrograph of a multilayer system six Pt (28 nm) and six Fe (22 nm) layers provided by Dr. Bo Yao and Dr. Kevin Coffey (AMPAC, UCF). (Right) Line scan across the Pt & Fe layers showing an increase in the intensity at the interface.

Another example showing the increase of atomic contrast near the interface of Pt and Fe layers is presented in Figure 63. Figure 63 (Left) shows the HAADF-STEM micrograph of six Pt (28 nm) and six Fe (22 nm) layers. A profile scan across the layers confirms an increase in the intensity near the interface (red circle) of Pt and Fe layers as shown in Figure 63 (Right).

6.1 The Ballistic Model

An algorithm based on a ballistic model is developed here using Python programming. Individual electrons are transmitted through the sample in the simulation. For each thin slice of the sample, the individual electrons get scattered with probabilities that are derived from the elastic and

absorptive coefficients of the two materials (e.g., W and SiO_2). *Peng et al*. [2] parameters (elastic coefficients) have been used in the present program. Absorptive parameter (μ) has been used from Table 1. The program calculates the scattering cross-sections of both the materials. A convergent electron beam is defined and for each beam position several thousand electrons are propagated through the sample.

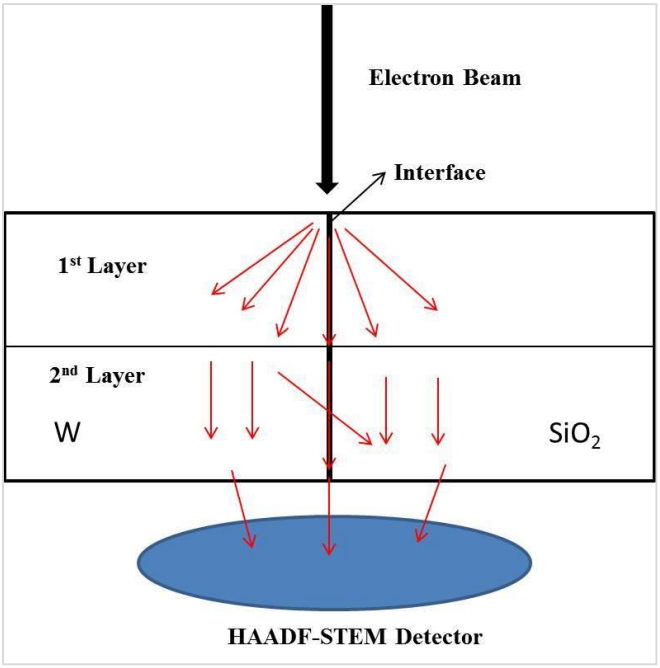

Figure 64 Schematic showing the electron beam hitting at the interface between two materials of higher and lower densities.

The HAADF-STEM signal at different sample thicknesses is determined for several scan positions in both materials at different distances from the interface.

The schematic of the whole system is shown in Figure 64. The program employs absorption and scattering probabilities at every thickness step. The path of each electron is tracked as the electron

passes through the sample suffering multiple scattering events. The tracking is done both in real space as well as in momentum space. The real space position of the electron is recorded to track the position of the electron near the interface and to determine if it is in the low or high density material. This is important as different scattering probabilities are used for both materials. The program also tracks the angle at which the electron traverses the materials. This corresponds to the x-y components of the electrons momentum vector and to the scattering angle of electrons in the diffraction plane.

6.2 Ballistic Model Simulations

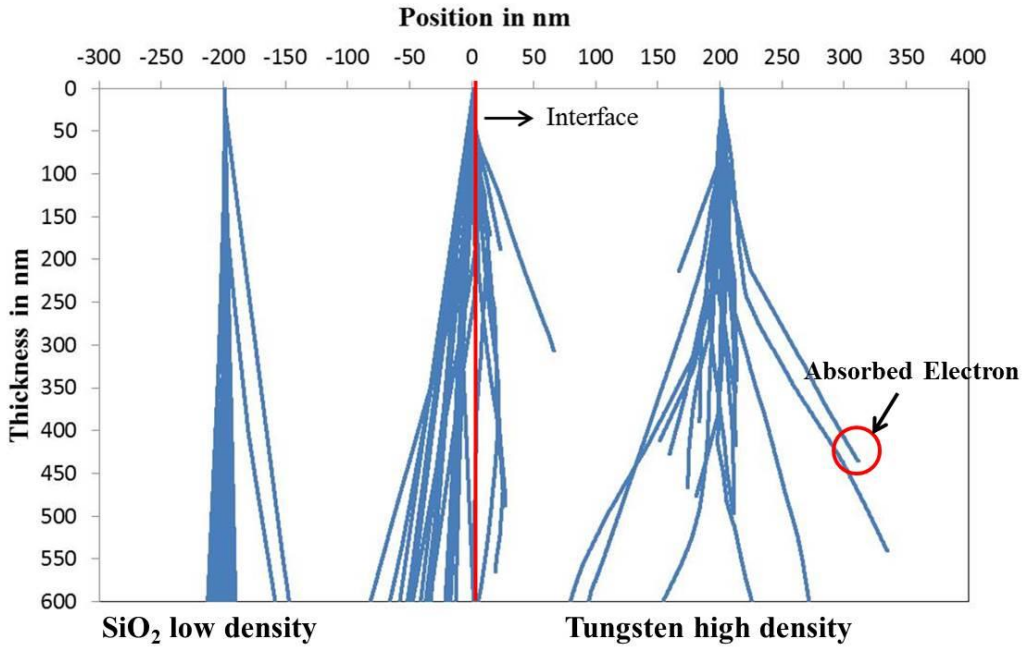

Figure 65 Simulated electron paths near the interface between two materials.

We can observe that electrons get scattered and absorbed more frequently in the high density material (W) as compared to the low density material (SiO_2). Near the interface some of the

electrons scatter from the high density to the lower density material as shown in Figure 65. More electrons get absorbed in the higher density material as the electrons lose energy and are no more collected by any detector in the diffraction plane. An example of this type of electron has been marked by a red circle in Figure 65. The algorithm used in this program counts the number of electrons scattered and absorbed in the high and low density material.

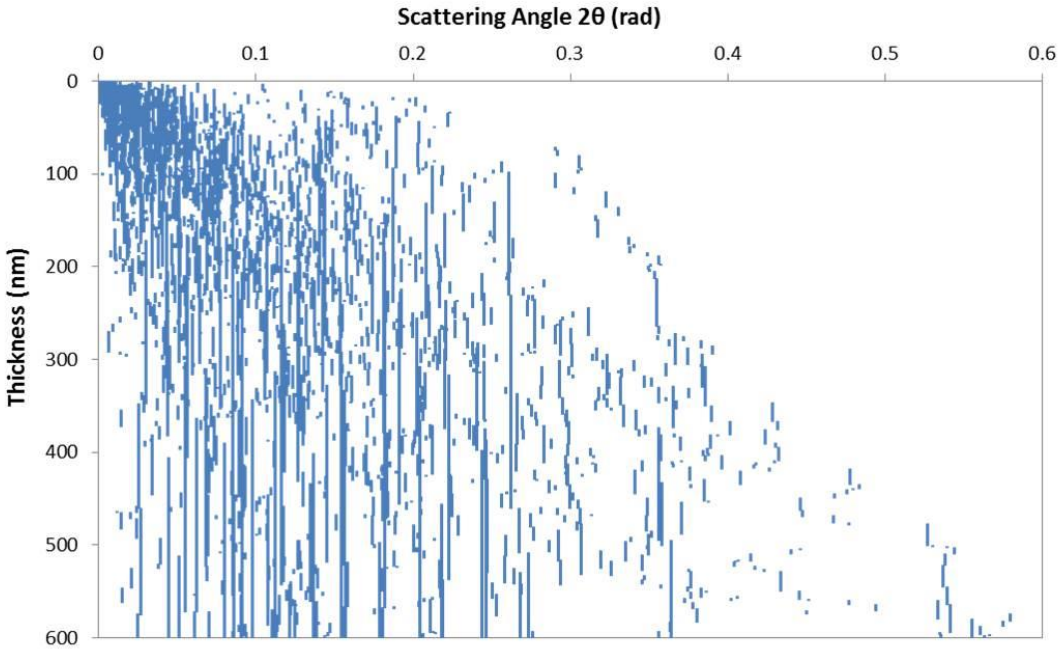

Figure 66 Magnitude of the scattering angle of electrons in a high density material (W) as a function as a function of sample thickness.

The HAADF-STEM detector collects electrons which are scattered at angles between (80-460) mrad, but some electrons are scattered even to higher angles. Electrons which are scattered at even higher angles do not contribute to the detector signal.

Figure 66 shows the magnitude of the scattering angle of some electrons as they pass through the samples. As the thickness of the sample increases, more and more electrons are scattered at higher

angles. The detector intensity is reduced by absorption and to a small part by electrons that are scattered to higher angles than the maximum detection angle of the HAADF-STEM detector (460 mrad).

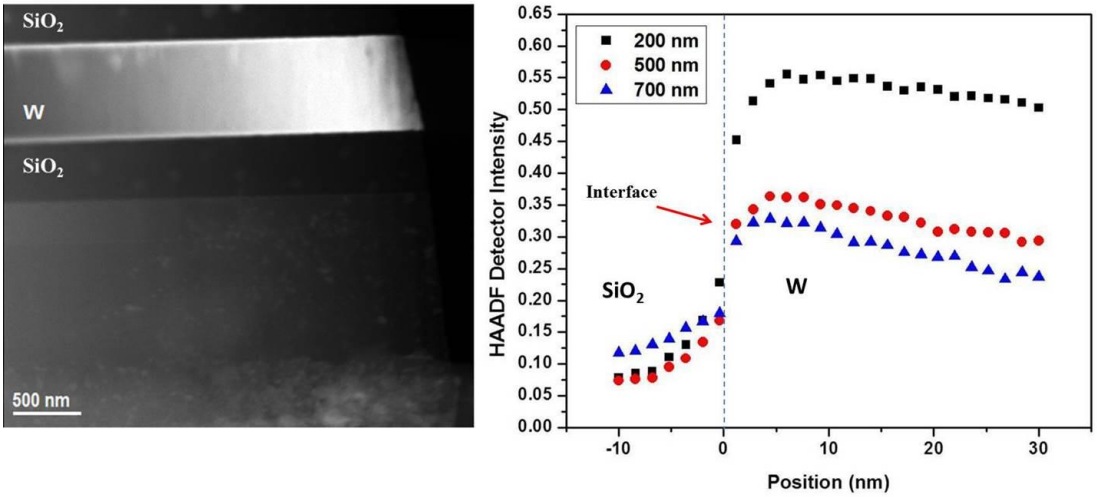

Figure 67 (Left) HAADF –STEM micrograph showing Tungsten and SiO_2 layers for a wedge shaped sample. (Right) HAADF – STEM detector signal for varying sample thickness.

Figure 67 (Right) shows the variation of the detector-STEM signal with increasing thickness of the sample. A wedge shaped FIB sample of W and SiO_2 layers has been used for this purpose. The scattering of electrons from higher to lower density of material near the interface is not much pronounced at lower thickness but with sample thicknesses greater than 400 nm, this effect is much more noticeable as depicted in Figure 67 (Right). Figure 67 also depicts the fact that the increase in detector intensity appears mostly within (0-20) nm from the interface of the two materials.

Figure 68 (Top) shows the grey scale image generated from the ballistic model simulations. The black layer represents SiO_2 and the top white layer W. As we go from the left to the right the

thickness increases which is seen in the gray scale image and from the profile in Figure 68 (Bottom).

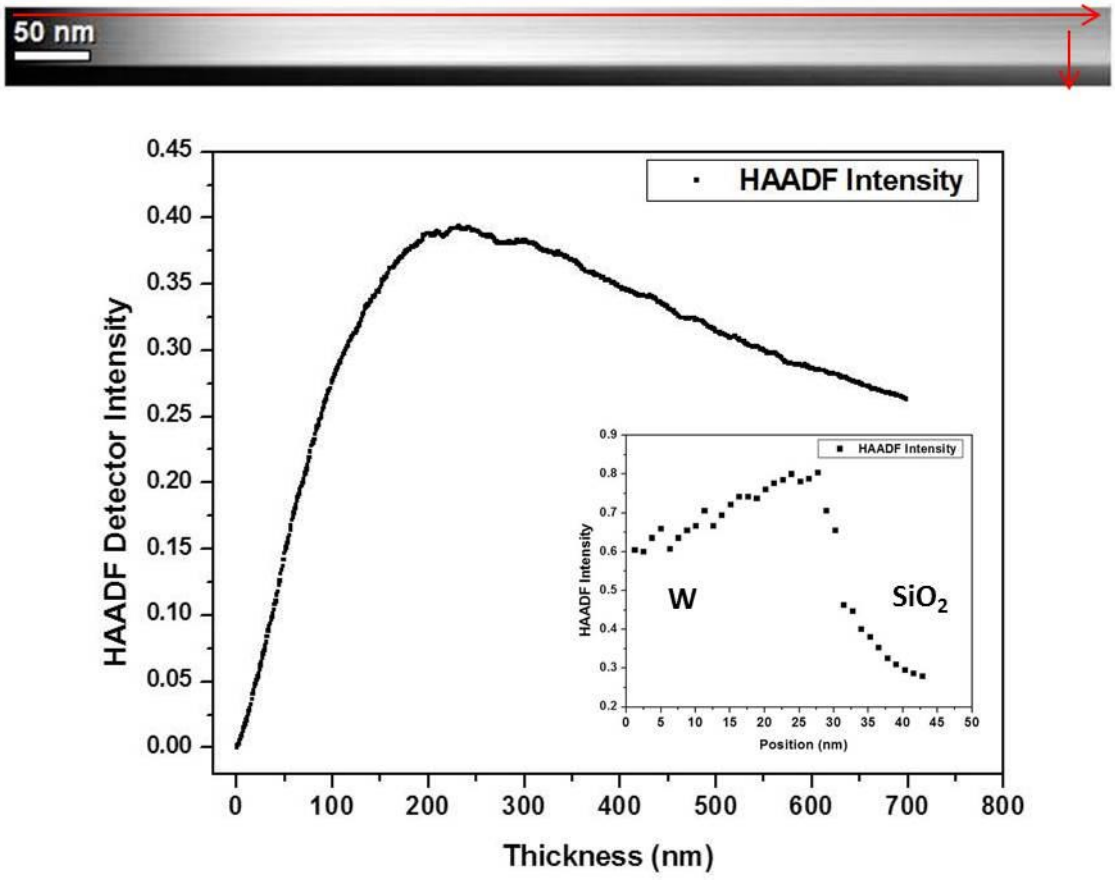

Figure 68 (Top) Gray scale image formed ballistic model simulation. (Bottom) Horizontal line scan for W as marked by the red line . The inset shows the vertical line scan across the SiO_2 –W interface as marked by the red line on the top image.

The inset in Figure 68 (Bottom) shows the vertical scan across the SiO_2-W interface as marked by the red line at 670 nm sample thickness in Figure 68 (Top). There is some statistical noise in the data of this line scan across the simulated interface as 10,000 incident electrons were used for the

simulation. Statistical variations can be reduced by increasing the number of incident electrons in the simulation. Nevertheless, even with this small number of incident electrons used in the simulation, there is an increase in HAADF-STEM signal near the interface followed by a decrease as we go in the tungsten region, as discussed earlier.

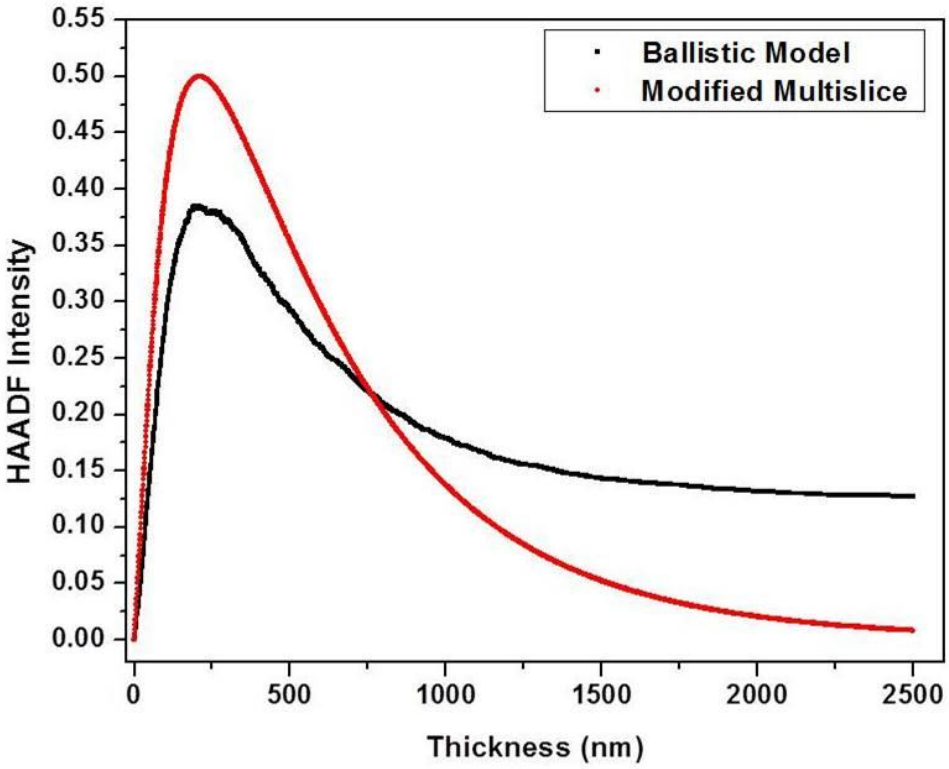

Figure 69 HAADF intensity of wedge shaped W vs. thickness from the ballistic model.

Figure 69 shows the HAADF intensity profile for a wedge-shaped W sample from the ballistic model and modified multislice method discussed above. The HAADF-STEM signal increases with thickness and reaches a peak at 275 nm in both cases but the modified multislice curve suffers more absorption. It can be concluded that the ballistic model for HAADF-STEM contrast

simulations is comparable to the modified multislice method only for sample thickness of up to 300 nm.

CHAPTER 7: CONCLUSIONS

HAADF-STEM has been used for the direct measurement of volumes of NPs using the TEM. The method of the formation of Au NPs by the reduction of different reducing agents produces NPs not only on the surface but also in specific cases inside the polymer matrix several nanometers below the surface. Au NPs formed by this process differ in size according to the strength of reducing agent and range from 2 to 20 nm in diameter. The direct measurement of the mean thickness of NPs from the calibrated HAADF-STEM plan-view image renders more accurate data on the volumes of Au NPs even if they are half buried in the polymer surface. While several research papers [3, 103, 115] have provided quantitative thickness and compositional data using the HAADF-STEM measurements, the above method and analyses provide high accuracy in the determination of particle size distributions as well as three-dimensional volume data. From the statistical analysis, a better understanding of the size distribution of NPs on or near the surface of the polymer is obtained. The distribution of Au NPs should play an important role for the selective deposition of metal NPs for fabrication purposes [116-118].

Our technique measures the volume of Au NPs directly from the intensity-calibrated HAADF-STEM images rather than measuring the diameter. As a result, this technique reduces the experimental error in the measurement of the radius of the NP considerably [119-121]. Statistical analysis identifies the dominant shape of the NPs when they are not exactly spherical [121-123]. In this method the local background noise is subtracted in the HAADF-STEM image for individual NPs to account for the small changes in height of the polymer layer beneath. For Au NPs, we show in Figure 20 that a thickness as high as 50 nm can be reliably determined from calibrated HAADF-STEM micrographs. Initial tilt series imaging of a distribution of Au NPs on SU-8 polymer also

confirms the particle trajectory for further analysis of the Au NPs and 3-D characterization. Special care has to be taken that the NP is well focused to ensure that local thicknesses can be accurately determined from HAADF-STEM micrographs, especially at the NP edges where the thickness variation is large. However, if the integrated intensity is used to determine the volume of an NP small defocusing effects do not significantly change the calculated volume as HAADF-STEM uses mostly incoherently scattered electrons. Defocusing merely blurs the outline of an NP making it more difficult to define its edge. Our method of analysis of Au NPs can be extended to other systems where we find a distribution of NPs on the surface of a substrate as shown in the case of Ag NPs in Figure 33. However, special care has to be taken to account for nonlinearities of the HAADF-STEM signal if the NP thickness reaches values close to the maximum in the HAADF-STEM signal vs. thickness curve.

The morphology of the Ag NPs prepared by electroless deposition method has been investigated in this dissertation [121-123]. Silvering on SU-8 polymer for 30 sec to 8 min has been achieved where Au NPs act as nucleating agent for the growth of silver. Controlled deposition of silver using gum arabic was performed and examined showing defects in Ag NPs the formation of stacking faults and twin boundaries. The density of Ag NPs was also calculated from tilted BF-TEM micrographs. The quantification of the time dependent silver deposition and the defect studies help to understand the morphology for the metallization of silver.

An important conclusion of this work is the HAADF signal measurement for elements at different temperatures. While previous studies suggest that the STEM signal should increase with an increase in temperature in crystalline samples [73, 74] no such increase in the HAADF-STEM signal was observed as shown in Figures 41 & 42. Samples studied in this work were mainly

polycrystalline and amorphous samples. Figure 43 confirms that the HAADF signal increases with an increase in the atomic number of elements as has been suggested in the literature [70, 71, 124, 125]. With the methods developed in this dissertation we now can predict the behavior of the HAADF-STEM signal as a function of sample thickness for different materials.

This work shows that it is not possible to use the classical multislice method for simulations of the HAADF-STEM signal in thick TEM samples. Thus, a modification of the classical multislice method has been introduced in this work. The new modified multislice method determines the intensity of the electron beam as it passes through the sample rather than the wave function. The modified multislice method has been used to determine the HAADF-STEM detector intensity for sample thickness up to 3 μm for various elements using the *Peng et al.* computed elastic scattering parameters. The simulation results don't match with the experimental results as shown in Figure 50 & 51 if absorptive factors from *Peng et al.* [100] are used. The reason for the mismatch is that the absorptive factors from [100] accurately describe the loss of intensity of coherent Bragg reflections, but the experimental signal with the HAADF-STEM detector also collects incoherently scattered electrons. Therefore, the absorptive factors by *Peng et al.* [100] have no significant influence on the HAADF-STEM signal and can be neglected. Instead, an absorption parameter obtained from experimental data has been introduced in simulations.

Equation 5.25 has been proposed by Biao Yuan [90] for the thickness dependence of the HAADF-STEM signals where a absorptive parameter μ is introduced. With the help of the modified multislice method this absorptive parameter was calculated for different elements in the periodic table. The simulation curves match well with the experiments except for high atomic numbers where the experimental HAADF-STEM signal is smaller than the simulated one. Since absorptive

parameters for are not known, the modified multislice cannot be used for any element, unless it is measured from a wedge-shaped TEM sample. The modified multislice uses the atomic densities and does not consider the crystal structure of the materials. Therefore, this method is not well suited for thin samples oriented exactly in low-indexed orientations. These are some of the limitations of this method.

A new ballistic scattering model is proposed in the present work to investigate the behavior of the HAADF-STEM signal at the interface of a high and low density material. A significant increase of the HAADF-STEM signal is observed at the interface between a low and a high density material as shown in Figure 61 & 63 for samples more than 300 nm in thickness [126]. The new ballistic model uses the elastic coefficients calculated by.*Peng et al.* [2, 100] to determine the scattering cross-sections in each material to track the path of the electrons near and across the interface using a convergent incident electron beam. Using Python for programming our model proves that at the interface the electrons move from the higher density material to a lower density material due to the higher frequency of scattering events in the high density material. After reaching the low density material these electrons suffer less scattering and absorption than in the high density material. Thus, the number of electrons reaching the HAADF-STEM detector is higher directly at the interface than further away from the interface. This effect is well pronounced as the thickness of the sample increases (>300 nm) within 10 nm of the interface. Grey-scale images from simulations are consistent with experimental images. Thus the ballistic model clearly demonstrates that the atomic contrast at interface in thick samples has to be interpreted with care and not simply related to atomic number contrast. Results from the simulations performed in this dissertation also

provide insight in the inelastic scattering phenomena and behavior of electrons which contribute to the formation of Z-contrast images in HAADF-STEM.

APPENDIX-A: DERIVATION OF EQUATION 5.7

The atomic scattering factor can be written as:

$$f(q) = f(\theta) = \frac{2Z(1+\frac{eV}{m_0c^2})}{a_{Bohr}(R^{-2}+q^2)} \tag{5.4}$$

where, $R = \frac{a_{Bohr}}{Z^{1/3}}$ and $q = 2.2\pi\frac{Sin\theta}{\lambda}$

$$f(q) = \frac{2Z(1+\frac{eV}{m_0c^2})}{a_{Bohr}(\frac{Z^{2/3}}{a_{Bohr}^{\ 2}}+\frac{16\pi^2Sin^2\theta}{\lambda^2})} = \frac{A}{B+Sin^2\theta}$$

where $A = 2Z(1+\frac{eV}{m_0c^2})$ and $B = \frac{Z^{2/3}\lambda^2}{16a_{Bohr}^{\ 2}\pi^2}$

Now from equation 5.3 interaction cross section can be written as:

$$\sigma = \int_{2\theta_{\min}}^{2\theta_{\max}} \left| f^2(\theta) \right| 2\pi Sin(2\theta)d(2\theta)$$

Integrating over the detector plane simplifies the above equation to:

$$= 4\pi \int_{\theta\min}^{\theta_{\max}} (\frac{A}{B+Sin^2\theta})^2.2Cos\theta Sin\theta d\theta$$

$$= 4\pi\left[\frac{A^2}{B+Sin^2\Theta_{\min}} - \frac{A^2}{B+Sin^2\Theta_{\max}}\right]$$

Substituting the values of *A* and *B* above we get:

$$\sigma = \frac{Z^2\lambda^4}{16\pi^3 a_{Bohr}^{\ 2}}(1+\frac{eV}{m_0c^2})^2\left[\frac{1}{\frac{Z^{2/3}\lambda^2}{16\pi^2 a_{Bohr}^{\ 2}}+Sin^2\Theta_{\min}} - \frac{1}{\frac{Z^{2/3}\lambda^2}{16\pi^2 a_{Bohr}^{\ 2}}+Sin^2\Theta_{\max}}\right] \tag{5.7}$$

APPENDIX-B: CURVE FITTING FOR MODIFIED MULTISLICE SIMULATED PLOTS

Curve fitting for the modified multislice simulation curves is done by using KaleidaGraph. Equation 5.24 has been used for fitting the plots. The absorption parameter (μ), the fraction of scattered electrons per nm (F) and the fraction of unabsorbed electrons (K/I_0) are determined from the best fit of multiple plots for all the elements. These parameters in Table 1 have been compared with the experimental values in Table 2.

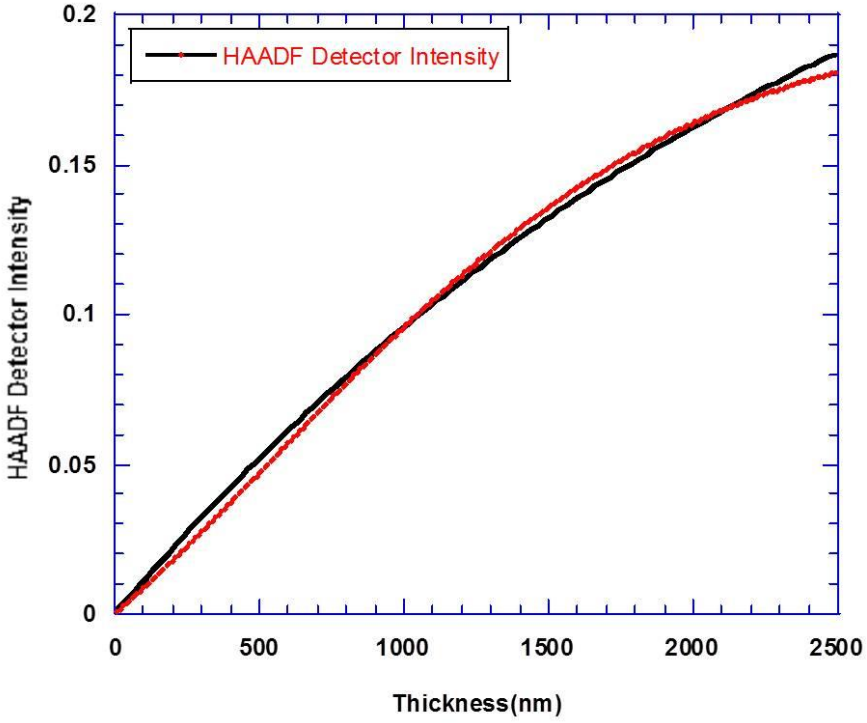

Figure 70 Curve fit according to equation 5.24 (black curve) for Al (Z=13) of the simulated curve (red) determined with the modified multislice method.

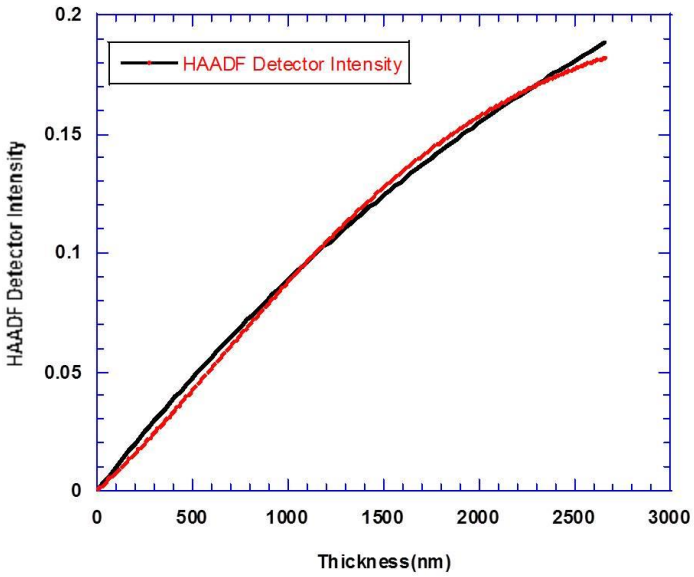

Figure 71 Curve fit according to equation 5.24 (black curve) for Si (Z=14) of the simulated curve (red) determined with the modified multislice method.

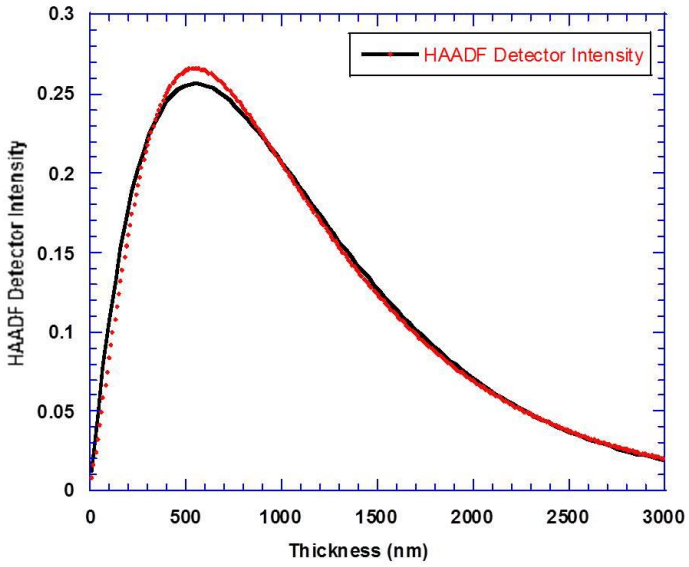

Figure 72 Curve fit according to equation 5.24 (black curve) for Fe (Z=26) of the simulated curve (red) determined with the modified multislice method.

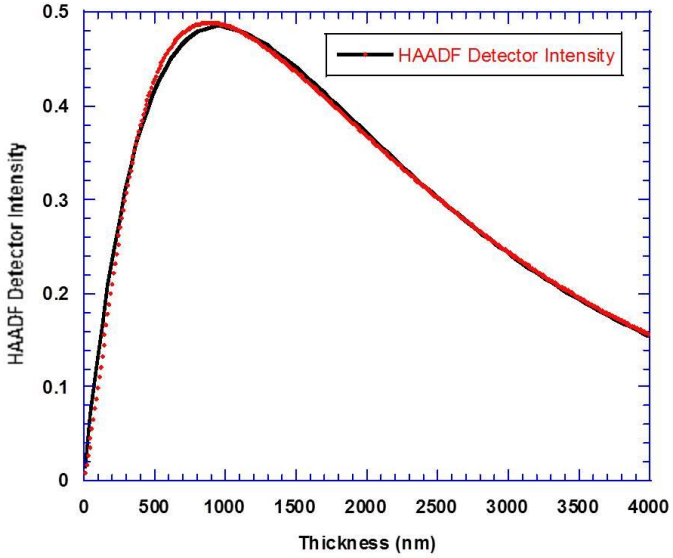

Figure 73 Curve fit according to equation 5.24 (black curve) for Cu (Z=29) of the simulated curve (red) determined with the modified multislice method.

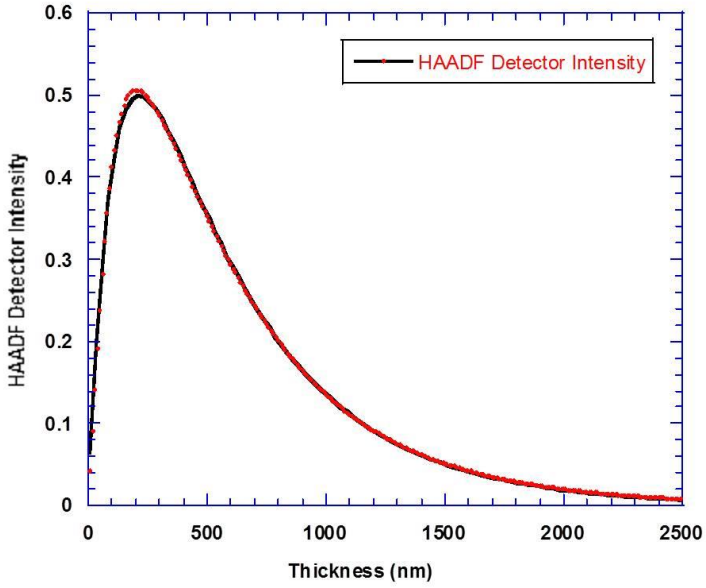

Figure 74 Curve fit according to equation 5.24 (black curve) for W (Z=74) of the simulated curve (red) determined with the modified multislice method.

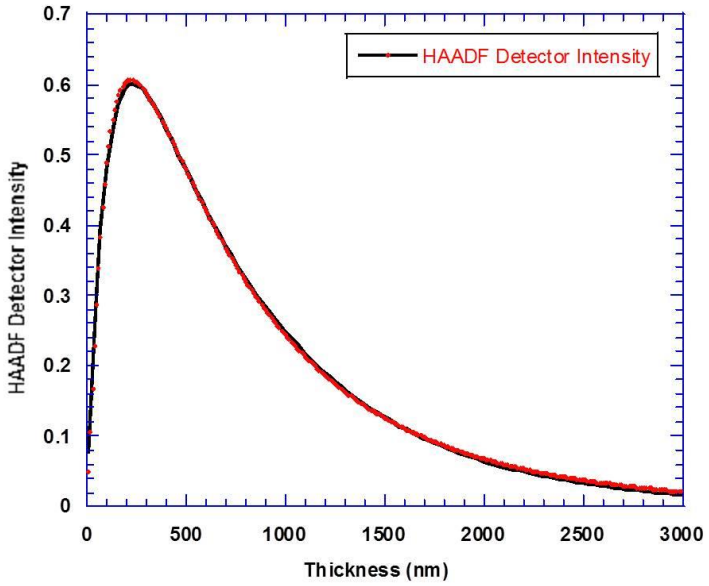

Figure 75 Curve fit according to equation 5.24 (black curve) for Pt (Z=78) of the simulated curve (red) determined with the modified multislice method.

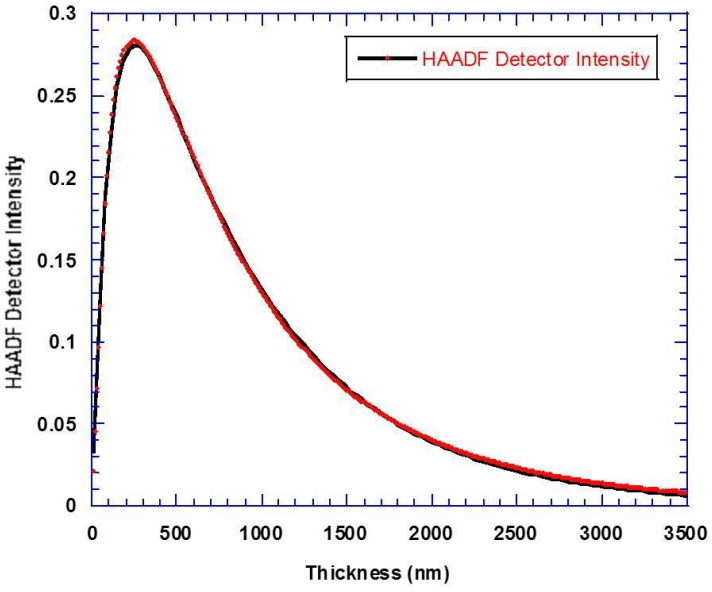

Figure 76 Curve fit according to equation 5.24 (black curve) for Au (Z=79) of the simulated curve (red) determined with the modified multislice method.

REFERENCES

[1] C. N. Grabill, H. E. Williams, S. M. Kuebler, A. Y. Quazzani, A. Bhattacharya, A. Dutta, *et al.*, "Chemical System for Fundamental Study of Electroless Metallization," presented at the Florida American Vacuum Society, Orlando, 2009.

[2] L.-M. Peng, G. Ren, S. L. Dudarev, and M. J. Whelan, "Robust Parameterization of Elastic and Absorptive Electron Atomic Scattering Factors," *Acta Crystallographica Section A,* vol. 52, pp. 257-276, 1996.

[3] S. Van Aert, J. Verbeeck, R. Erni, S. Bals, M. Luysberg, D. V. Dyck, *et al.*, "Quantitative atomic resolution mapping using high-angle annular dark field scanning transmission electron microscopy," *Ultramicroscopy,* vol. 109, pp. 1236-1244, 2009.

[4] S. Van Aert, K. J. Batenburg, M. D. Rossell, R. Erni, and G. Van Tendeloo, "Three-dimensional atomic imaging of crystalline nanoparticles," in *Nature* vol. 470, ed: Nature Publishing Group, a division of Macmillan Publishers Limited, 2011.

[5] G. O. Mallory, J. B. Hajdu, A. Electroplaters, and S. F. Society, *Electroless plating: fundamentals and applications*: American Electroplaters and Surface Finishers Society, 1990.

[6] L. Balogh, D. R. Swanson, D. A. Tomalia, G. L. Hagnauer, and A. T. McManus, "Dendrimer−Silver Complexes and Nanocomposites as Antimicrobial Agents," *Nano Letters,* vol. 1, pp. 18-21, 2000.

[7] C. Aymonier, U. Schlotterbeck, L. Antonietti, P. Zacharias, R. Thomann, J. C. Tiller, *et al.*, "Hybrids of silver nanoparticles with amphiphilic hyperbranched macromolecules exhibiting antimicrobial properties," *Chemical Communications*, pp. 3018-3019, 2002.

[8] S. Sarkar, A. D. Jana, S. K. Samanta, and G. Mostafa, "Facile synthesis of silver nano particles with highly efficient anti-microbial property," *Polyhedron,* vol. 26, pp. 4419-4426, 2007.

[9] M. Weyland, P. A. Midgley, and J. M. Thomas, "Electron Tomography of Nanoparticle Catalysts on Porous Supports: A New Technique Based on Rutherford Scattering," *The Journal of Physical Chemistry B,* vol. 105, pp. 7882-7886, 2001.

[10] E. Carlino and V. Grillo, "Atomic-resolution quantitative composition analysis using scanning transmission electron microscopy Z-contrast experiments," *Physical Review B*, vol. 71, p. 235303, 2005.

[11] T. Inoue, T. Kita, O. Wada, M. Konno, T. Yaguchi, and T. Kamino, "Electron tomography of embedded semiconductor quantum dot," *Applied Physics Letters*, vol. 92, pp. 031902, 2009.

[12] Y. Kenta, H. I. Yumi, T. Seiji, H. Tsukasa, S. Tomohiro, S. Shogo, *et al.*, "The three-dimensional morphology of nickel nanodots in amorphous silica and their role in high-temperature permselectivity for hydrogen separation," *Nanotechnology*, vol. 20, p. 315703, 2009.

[13] K. Yoshida, L. Miao, N. Tanaka, and S. Tanemura, "Direct observation of TiO 6 octahedron forming titanate nanotube by advanced transmission electron microscopy," *Nanotechnology*, vol. 20, p. 405709, 2009.

[14] A. Robledo, C. N. Grabill, S. M. Kuebler, A. Dutta, H. Heinrich, and A. Bhattacharya, "Morphologies from slippery ballistic deposition model: A bottom-up approach for nanofabrication," *Physical Review E*, vol. 83, p. 051604, 2011.

[15] B. Yuan, H. Heinrich, B. Yao, and A. Dutta, "Quantitative Measurement of Volumes for Nanoparticles by High-Angle Annular Dark-Field Scanning Transmission Electron Microscopy," *Microscopy and Microanalysis*, vol. 16, pp. 1764-1765, 2010.

[16] J. M. Cowley, V. I. Merkulov, and J. S. Lannin, "Imaging of light-atom nanocrystals with a thin annular detector in STEM," *Ultramicroscopy*, vol. 65, pp. 61-70, 1996.

[17] D. B. Williams and C. B. Carter, *Transmission Electron Microscopy: A Textbook for Materials Science*: Kluwer Academic Pub, 1996.

[18] K. Ishizuka, "A practical approach for STEM image simulation based on the FFT multislice method," *Ultramicroscopy*, vol. 90, pp. 71-83, 2002.

[19] T. Yamazaki, M. Kawasaki, K. Watanabe, I. Hashimoto, and M. Shiojiri, "Effect of small crystal tilt on atomic-resolution high-angle annular dark field STEM imaging," *Ultramicroscopy*, vol. 92, pp. 181-189, 2002.

[20] S. Bals, B. Kabius, M. Haider, V. Radmilovic, and C. Kisielowski, "Annular dark field imaging in a TEM," *Solid State Communications,* vol. 130, pp. 675-680, 2004.

[21] K. Watanabe, E. Asano, T. Yamazaki, Y. Kikuchi, and I. Hashimoto, "Symmetries in BF and HAADF STEM image calculations," *Ultramicroscopy,* vol. 102, pp. 13-21,2004.

[22] S. Bals, R. Kilaas, and C. Kisielowski, "Nonlinear imaging using annular dark field TEM," *Ultramicroscopy,* vol. 104, pp. 281-289, 2005.

[23] P. Wang, A. L. Bleloch, U. Falke, and P. J. Goodhew, "Geometric aspects of lattice contrast visibility in nanocrystalline materials using HAADF STEM," *Ultramicroscopy,* vol. 106, pp. 277-283, 2006.

[24] T. Morimura and M. Hasaka, "Bloch-wave-based STEM image simulation with layer-by-layer representation," *Ultramicroscopy,* vol. 109, pp. 1203-1209, 2009.

[25] Z. L. Wang, "Thermal diffuse scattering in sub-angstrom quantitative electron microscopy—phenomenon, effects and approaches," *Micron,* vol. 34, pp. 141-155, 2003.

[26] Z. Wang, *Elastic and Inelastic Scattering in Electron Diffraction and Imaging*: Springer US, 2013.

[27] G. Witzgall, R. Vrijen, E. Yablonovitch, V. Doan, and B. J. Schwartz, "Single-shot two-photon exposure of commercial photoresist for the production of three-dimensional structures," *Optics Letters,* vol. 23, pp. 1745-1747, 1998.

[28] Z. Nanyan, X. Jining, G. Manton, and K. V. Vijay, "Chemical bonding of multiwalled carbon nanotubes to SU-8 via ultrasonic irradiation," *Smart Materials and Structures,* vol. 12, p. 260, 2003.

[29] Y.-S. Chen, A. Tal, and S. M. Kuebler, "Route to Three-Dimensional Metallized Microstructures Using Cross-Linkable Epoxide SU-8," *Chemistry of Materials,* vol. 19, pp. 3858-3860, 2007.

[30] M.-C. Daniel and D. Astruc, "Gold Nanoparticles: Assembly, Supramolecular Chemistry, Quantum-Size-Related Properties, and Applications toward Biology, Catalysis, and Nanotechnology," *Chemical Reviews,* vol. 104, pp. 293-346, 2003.

[31] R. G. DiScipio, "Preparation of Colloidal Gold Particles of Various Sizes Using Sodium Borohydride and Sodium Cyanoborohydride," *Analytical Biochemistry,* vol. 236, pp. 168-170,1996.

[32] M. Khalid, I. Pala, N. Wasio, and K. Bandyopadhyay, "Functionalized surface as template for in situ generation of two-dimensional metal nanoparticle assembly," *Colloids and Surfaces A: Physicochemical and Engineering Aspects,* vol. 348, pp. 263-269,2009.

[33] G. Danscher, "Histochemical demonstration of heavy metals," *Histochemistry,* vol. 71, pp. 1-16, 1981.

[34] Z. Huang, "Combining Ar ion milling with FIB lift-out techniques to prepare high quality site-specific TEM samples," *Journal of Microscopy,* vol. 215, pp. 219-223, 2004.

[35] R. J. Patterson, D. Mayer, L. Weaver, and M. W. Phaneuf, ""H-Bar Lift-Out" and "Plan-View Lift-Out": Robust, Re-thinnable FIB-TEM Preparation for Ex-Situ Cross-Sectional and Plan-View FIB Specimen Preparation," *Microscopy and Microanalysis,* vol. 8, pp. 566-567, 2002.

[36] R. M. Anderson, "Comparison of FIB TEM Specimen Preparation MethodsTEM," *Microscopy and Microanalysis,* vol. 8, pp. 44-45, 2002.

[37] W. Brostow, B. P. Gorman, and O. Olea-Mejia, "Focused ion beam milling and scanning electron microscopy characterization of polymer + metal hybrids," *Materials Letters,* vol. 61, pp. 1333-1336, 2007.

[38] J. Li, T. Malis, and S. Dionne, "Recent advances in FIB–TEM specimen preparation techniques," *Materials Characterization,* vol. 57, pp. 64-70, 2006.

[39] J. Loos, J. K. J. van Duren, F. Morrissey, and R. A. J. Janssen, "The use of the focused ion beam technique to prepare cross-sectional transmission electron microscopy specimen of polymer solar cells deposited on glass," *Polymer,* vol. 43, pp. 7493-7496, 2002.

[40] In-situ or Ex-situ? Which TEM section lift-out method is best? *NanoScope FIB technology article*.

[41] G. McMahon, J. Rybczynski, Y. Wang, Y. Gao, D. Cai, P. Dhakal, *et al.*, "Applications of Multibeam SEM/FIB Instrumentation in the Integrated Sciences," *Microscopy Today,* vol. 17, pp. 34-39, 2009.

[42] L. A. Giannuzzi and F. A. Stevie, *Introduction to Focused Ion Beams: Instrumentation, Theory, Techniques and Practice*, 1 ed.: Springer US, 2005.

[43] FEI, "FIB manual for FEI 200 Series system", ed: FEI, 1996.

[44] A. Latif, "Nanofabrication using Focused Ion Beam," PhD, Material Science & Metallurgy, Cambridge, 2000.

[45] N. D. Browning, D. J. Wallis, P. D. Nellist, and S. J. Pennycook, "EELS in the STEM: Determination of materials properties on the atomic scale," *Micron,* vol. 28, pp. 333-348, 1997.

[46] J. Liu and L. Allard, "Channeling Contrast in Sub-Ångström Resolution High-Angle Annular Dark-Field Images of Planar Interfaces," *Microscopy and Microanalysis,* vol. 17, pp. 1300-1301, 2011.

[47] S. E. Maccagnano-Zacher, K. A. Mkhoyan, E. J. Kirkland, and J. Silcox, "Effects of tilt on high-resolution ADF-STEM imaging," *Ultramicroscopy,* vol. 108, pp. 718-726, 2008.

[48] C. Kübel, A. Voigt, R. Schoenmakers, M. Otten, D. Su, T.-C. Lee, *et al.*, "Recent Advances in Electron Tomography: TEM and HAADF-STEM Tomography for Materials Science and Semiconductor Applications," *Microscopy and Microanalysis,* vol. 11, pp. 378-400, 2005.

[49] A. Taleb, C. Mangeney, and V. Ivanova, "Metallic Nanostructure Formation Using Self-Assembled Chemically Anchored Gold Nanoparticles," *Journal of The Electrochemical Society,* vol. 158, pp. K28-K34, February 1, 2011.

[50] P. D. Nellist and S. J. Pennycook, "Accurate structure determination from image reconstruction in ADF STEM," *Journal of Microscopy*, vol. 190, pp. 159-170, 1998.

[51] E. M. James and N. D. Browning, "Practical aspects of atomic resolution imaging and analysis in STEM," *Ultramicroscopy*, vol. 78, pp. 125-139, 1999.

[52] J. V. Sanders, "Transmission electron microscopy of catalysts," *Journal of Electron Microscopy Technique*, vol. 3, pp. 67-93, 1986.

[53] E. B. Prestridge, G. H. Via, and J. H. Sinfelt, "Electron microscopy studies of metal clusters: Ru, Os, Ru · Cu, and Os · Cu," *Journal of Catalysis*, vol. 50, pp. 115-123,1977.

[54] L. D. Menard, S.-P. Gao, H. Xu, R. D. Twesten, A. S. Harper, Y. Song, *et al.*, "Sub-Nanometer Au Monolayer-Protected Clusters Exhibiting Molecule-like Electronic Behavior: Quantitative High-Angle Annular Dark-Field Scanning Transmission Electron Microscopy and Electrochemical Characterization of Clusters with Precise Atomic Stoichiometry," *The Journal of Physical Chemistry B*, vol. 110, pp. 12874-12883, 2006.

[55] H. Heinrich, B. Yuan, H. Nukala, and B. Yao, "Quantitative Scanning Transmission Electron Microscopy for the Measurement of Thicknesses and Volumes of Individual Nanoparticles," *MRS Online Proceedings Library*, vol. 1184, HH-01-06, 2009.

[56] A. Troupis, T. Triantis, A. Hiskia, and E. Papaconstantinou, "Rate-Redox-Controlled Size-Selective Synthesis of Silver Nanoparticles Using Polyoxometalates," *European Journal of Inorganic Chemistry*, vol. 2008 (36), pp. 5579-5586, 2008.

[57] R. Shankar, V. Shahi, and U. Sahoo, "Comparative Study of Linear Poly(alkylarylsilane)s as Reducing Agents toward Ag(I) and Pd(II) Ions−Synthesis of Polymer−Metal Nanocomposites with Variable Size Domains of Metal Nanoparticles," *Chemistry of Materials*, vol. 22, pp. 1367-1375, 2010.

[58] M. T. Reetz, M. Maase, T. Schilling, and B. Tesche, "Computer Image Processing of Transmission Electron Micrograph Pictures as a Fast and Reliable Tool To Analyze the Size of Nanoparticles," *The Journal of Physical Chemistry B*, vol. 104, pp. 8779-8781,2000.

[59] A. Dutta, C. J. Clukay, C. N. Grabill, D. J. Freppon, A. Bhattacharya, S. M. Kuebler, *et al.*, "Nanoscale characterization of gold nanoparticles created by in situ reduction at a polymeric surface," *Journal of Microscopy*, vol. 251, pp. 27-34, 2013.

[60] K. D. Sattler, *Handbook of Nanophysics Set*: Taylor & Francis, 2010.

[61] A. Seeger, "The stacking-fault energy of gold and silver," *Philosophical Magazine*, vol. 9, pp. 887-890,1964.

[62] H. Paul, J. H. Driver, C. Maurice, and A. Piątkowski, "Recrystallization mechanisms of low stacking fault energy metals as characterized on model silver single crystals," *Acta Materialia,* vol. 55, pp. 833-847, 2007.

[63] M. J. Yacamán, J. A. Ascencio, H. B. Liu, and J. Gardea-Torresdey, "Structure shape and stability of nanometric sized particles," *Journal of Vacuum Science Technology B*, vol. 19, pp. 1091-1103, 2001.

[64] H. B. Liu, J. A. Ascencio, M. Perez-Alvarez, and M. J. Yacaman, "Melting behavior of nanometer sized gold isomers," *Surface Science,* vol. 491, pp. 88-98, 2001.

[65] S. Marco, T. Boudier, C. Messaoudi, and J. L. Rigaud, "Electron tomography of biological samples," *Biochemistry (Moscow),* vol. 69, pp. 1219-1225, 2004.

[66] J. Frank, *Electron Tomography: Three-Dimensional Imaging With the Transmission Electron Microscope*: Plenum Press, 1992.

[67] W. Baumeister, R. Grimm, and J. Walz, "Electron tomography of molecules and cells," *Trends in Cell Biology,* vol. 9, pp. 81-85.

[68] U. Ziese, K. P. de Jong, and A. J. Koster, "Electron tomography: a tool for 3D structural probing of heterogeneous catalysts at the nanometer scale," *Applied Catalysis A: General,* vol. 260, pp. 71-74, 2004.

[69] P. A. Midgley and M. Weyland, "3D electron microscopy in the physical sciences: the development of Z-contrast and EFTEM tomography," *Ultramicroscopy,* vol. 96, pp. 413-431, 2003.

[70] M. M. J. Treacy and J. M. Gibson, "Coherence and multiple scattering in “Z-contrast” images," *Ultramicroscopy,* vol. 52, pp. 31-53, 1993.

[71] S. J. Pennycook, "Z-contrast stem for materials science," *Ultramicroscopy,* vol. 30, pp. 58-69, 1989.

[72] Augsten, "L. Reimer, Scanning Electron Microscopy — Physics of Image Formation and Microanalysis (Springer Series in Optical Sciences, Volume 45. Editiorial Board: J. M. Enoch, D. L. Macadam, A. L. Schawlow, K. Shimoda and T. Tamir). XVIII + 457 S., 247 Abb., 5 Tab. Berlin-Heidelberg-New York-Tokyo 1985. Springer Verlag. DM 112,00. ISBN: 3-540-13530-8," *Journal of Basic Microbiology,* vol. 27, pp. 166-166, 1987.

[73] M. Libera, J. A. Ott, and K. Siangchaew, "Temperature-dependent high-angle electron scattering from a phase-separated amorphous GeTe thin film," *Ultramicroscopy,* vol. 63, pp. 81-91, 1996.

[74] T. Mehrtens, M. Schowalter, D. Tytko, P. Choi, D. Raabe, L. Hoffmann, *et al.*, "Measuring composition in InGaN from HAADF-STEM images and studying the temperature dependence of Z-contrast," in *Journal of Physics: Conference Series*, 2013, p. 012009.

[75] R. V. Petrova, "Quantitative High-Angle Annular Dark Field Scanning Transmission Electron Microscopy for Material Science," PhD, Department of Physics, University of Central Florida, Orlando, 2006.

[76] R. F. Loane, P. Xu, and J. Silcox, "Incoherent imaging of zone axis crystals with ADF STEM," *Ultramicroscopy,* vol. 40, pp. 121-138, 1992.

[77] R. F. Loane, P. Xu, and J. Silcox, "Thermal vibrations in convergent-beam electron diffraction," *Acta Crystallographica Section A,* vol. 47, pp. 267-278, 1991.

[78] J. M. Cowley, *Electron Diffraction Techniques*: International Union of Crystallography, 1992.

[79] D. D. Perovic, C. J. Rossouw, and A. Howie, "Imaging elastic strains in high-angle annular dark field scanning transmission electron microscopy," *Ultramicroscopy,* vol. 52, pp. 353-359, 1993.

[80] J. M. Cowley and Y. Huang, "De-channelling contrast in annular dark-field STEM," *Ultramicroscopy,* vol. 40, pp. 171-180, 1992.

[81] Z. L. Wang and J. M. Cowley, "Simulating high-angle annular dark-field stem images including inelastic thermal diffuse scattering," *Ultramicroscopy,* vol. 31, pp. 437-453, 1989.

[82] A. Howie and U. Valdrè, "Temperature dependence of the extinction distance in electron diffraction," *Philosophical Magazine,* vol. 15, pp. 777-781, 1967.

[83] S. J. Pennycook and D. E. Jesson, "High-resolution Z-contrast imaging of crystals," *Ultramicroscopy,* vol. 37, pp. 14-38, 1991.

[84] D. E. Jesson and S. J. Pennycook, "Incoherent Imaging of Crystals Using Thermally Scattered Electrons," *Proceedings: Mathematical and Physical Sciences,* vol. 449, pp. 273-293, 1995.

[85] J. M. Cowley and A. F. Moodie, "The scattering of electrons by atoms and crystals. I. A new theoretical approach," *Acta Crystallographica,* vol. 10, pp. 609-619, 1957.

[86] K. Ishizuka and N. Uyeda, "A new theoretical and practical approach to the multislice method," *Acta Crystallographica Section A,* vol. 33, pp. 740-749, 1977.

[87] E. J. Kirkland, R. F. Loane, and J. Silcox, "Simulation of annular dark field stem images using a modified multislice method," *Ultramicroscopy,* vol. 23, pp. 77-96, 1987.

[88] *Absorption cross section.* Available:http://en.wikipedia.org/wiki/Absorption_cross_section

[89] M. Rühle and F. Ernst, *High-Resolution Imaging and Spectrometry of Materials*: Springer, 2003.

[90] B. Yuan, "Direct Measurement of Thicknesses, Volumes or Compositions of Nanomaterials by Quantitative Atomic Number Contrast In High-Angle Annular Dark-Field Scanning Transmission Electron Microscopy," PhD, Mechanical, Materials and Aerospace Engineering University of Central Florida, Orlando, 2012.

[91] M. A. Coulthard, "A relativistic Hartree-Fock atomic field calculation," in *Proceedings of the Physical Society*, 1967, p. 44.

[92] P. A. Doyle and P. S. Turner, "Relativistic Hartree-Fock X-ray and electron scattering factors," *Acta Crystallographica Section A,* vol. 24, pp. 390-397, 1968.

[93] V. Vand, P. F. Eiland, and R. Pepinsky, "Analytical representation of atomic scattering factors," *Acta Crystallographica,* vol. 10, pp. 303-306, 1957.

[94] S. Kirkpatrick, C. D. Gelatt, and M. P. Vecchi, "Optimization by Simulated Annealing," *Science,* vol. 220, pp. 671-680, 1983.

[95] W. H. Press, *Numerical Recipes in Pascal (First Edition): The Art of Scientific Computing*: Cambridge University Press, 1989.

[96] A. Weickenmeier and H. Kohl, "Computation of absorptive form factors for high-energy electron diffraction," *Acta Crystallographica Section A,* vol. 47, pp. 590-597, 1991.

[97] D. M. Bird and Q. A. King, "Absorptive form factors for high-energy electron diffraction," *Acta Crystallographica Section A,* vol. 46, pp. 202-208, 1990.

[98] S. W. Lovesey, *Theory of Neutron Scattering from Condensed Matter*: Clarendon Press, 1984.

[99] V. F. Sears and S. A. Shelley, "Debye-Waller factor for elemental crystals," *Acta Crystallographica Section A,* vol. 47, pp. 441-446, 1991.

[100] L.-M. Peng, G. Ren, S. L. Dudarev, and M. J. Whelan, "Debye-Waller Factors and Absorptive Scattering Factors of Elemental Crystals," *Acta Crystallographica Section A,* vol. 52, pp. 456-470, 1996.

[101] C. R. Hall and P. B. Hirsch, "Effect of Thermal Diffuse Scattering on Propagation of High Energy Electrons Through Crystals," *Proceedings of the Royal Society of London. Series A. Mathematical and Physical Sciences,* vol. 286, pp. 158-177, 1965.

[102] Y. Peng, P. D. Nellist, and S. J. Pennycook, "HAADF-STEM imaging with sub-angstrom probes: a full Bloch wave analysis," *Journal of Electron Microscopy,* vol. 53, pp. 257-266, 2004.

[103] J. M. LeBeau, S. D. Findlay, L. J. Allen, and S. Stemmer, "Quantitative Atomic Resolution Scanning Transmission Electron Microscopy," *Physical Review Letters,* vol. 100, p. 206101, 2008.

[104] T. Morimura, "STEM image simulation by Bloch-wave method with layer-by-layer representation," *Journal of Electron Microscopy,* vol. 59, pp. S23-S28, 2010.

[105] E. J. Kirkland, "Nonlinear high resolution image processing of conventional transmission electron micrographs: I. Theory," *Ultramicroscopy,* vol. 9, pp. 45-64, 1982.

[106] K. Ishizuka, "A practical approach for STEM image simulation based on the FFT multislice method," *Ultramicroscopy,* vol. 90, pp. 71-83, 2002.

[107] R. Erni, H. Heinrich, and G. Kostorz, "Quantitative characterisation of chemical inhomogeneities in AlAg using high-resolution Z-ontrast STEM," *Ultramicroscopy,* vol. 94, pp. 125-133, 2003.

[108] K. Ishizuka, "FFT multislice method - The silver anniversary," *Microscopy and Microanalysis,* vol. 10, pp. 34-40, 2004.

[109] T. Yamazaki, K. Watanabe, K. Kuramochi, and I. Hashimoto, "Extended dynamical HAADF STEM image simulation using the Bloch-wave method," *Acta Crystallographica Section A,* vol. 62, pp. 233-236, 2006.

[110] P. Hawkes and J. C. H. Spence, *Science of Microscopy*: Springer, 2008.

[111] S. J. Pennycook and P. D. Nellist, *Scanning Transmission Electron Microscopy: Imaging and Analysis*: Springer, 2011.

[112] G. Van Tendeloo, D. Van Dyck, and S. J. Pennycook, *Handbook of Nanoscopy 2 Volume Set*: John Wiley & Sons, 2012.

[113] A. Dutta, C. Reid, and H. Heinrich, "Simulation of Incoherent Scattering in High-Angle Annular Dark-Field Scanning Electron Microscopy," *Microscopy and Microanalysis,* vol. 19, pp. 852-853, 2013.

[114] B. Yao, PhD, Mechanical, Materials and Aerospace Engineering University of Central Florida, Orlando, 2008.

[115] J. LeBeau, S. Findlay, L. Allen, and S. Stemmer, "Quantitative HAADF-STEM and EELS," *Microscopy and Microanalysis,* vol. 14, pp. 1352-1353, 2008.

[116] D. Panjwani, M. Yesiltas, J. Nath, D. E. Maukonen, I. Rezadad, E. M. Smith, *et al*., "Patterning of oxide-hardened gold black by photolithography and metal lift-off," *Infrared Physics & Technology*, vol. 62, pp. 94-99, 2014.

[117] D. Panjwani, M. Yesiltas, S. Singh, E. D. Barco, R. E. Peale, C. Hirschmugl, *et al*., "Stencil lithography of gold-black IR absorption coatings,"*Infrared Physics & Technology*, vol. 66, pp. 1-5, 2014.

[118] C. J. Clukay, C. N. Grabill, M. A. Hettinger, A. Dutta, D. J. Freppon, A. Robledo, *et al*., "Controlling formation of gold nanoparticles generated in situ at a polymeric surface," *Applied Surface Science*, vol. 292, pp. 128-136, 2014.

[119] A. Dutta, B. Yuan, C. J. Clukay, C. N. Grabill, H. Heinrich, A. Bhattacharya, *et.al*.," Quantification of metallic nanoparticle morphology with tilt series imaging by transmission electron microscopy,"*Bulletin of the American Physical Society*, 2012, March 2. Retrieved from http://meetings.aps.org/Meeting/MAR12/Session/Y1.2.

[120] A. Dutta, H. Heinrich, S. M. Kuebler, C. N. Grabill, A. Bhattacharya," Quantitative Transmission Electron Microscopy of Nanoparticles and Thin-Film Formation in Electroless Metallization of Polymeric Surfaces,"*Bulletin of the American Physical Society*, 2011, March 25. Retrieved from http://meetings.aps.org/Meeting/MAR11/Session/Z10.14.

[121] M. Lively, A. Bhattacharya, C. N. Grabill, S. M. Kuebler, A. Dutta, H. Heinrich," Simulation studies of electroless metal deposition using gold nano-clusters on polymeric

surfaces,"*Bulletin of the American Physical Society*, 2010, March 16. Retrieved from http://meetings.aps.org/Meeting/MAR10/Session/K1.152.

[122] S. M. Kuebler, C. J. Clukay, A. Dutta, C. N. Grabill, H. Heinrich, A. Bhattacharya," Morphologies of an anisotropic diffusion limited growth model to study electroless deposition,"*Bulletin of the American Physical Society*, 2012, February 28. Retrieved from http://meetings.aps.org/Meeting/MAR12/Session/K1.233.

[123] A. Dutta, B. Yuan, H. Heinrich, C. N. Grabill, H. Williams, S. M. Kuebler, *et al*.," The Morphology of Silver Layers on SU8 polymers prepared by Electroless Deposition, *Bulletin of the American Physical Society*, 2010, March 18. Retrieved from http://meetings.aps.org/Meeting/MAR10/Session/V19.8.

[124] H. Khallaf, C. T. Chen, L. Chang, O. Lupan, A. Dutta, H. Heinrich, *et al*.," Chemical bath deposition of SnO2 and Cd2SnO4 thin films," *Applied Surface Science*, vol. 258 (16), pp. 6069-74, 2012.

[125] H. Khallaf, C. T. Chen, L. Chang, O. Lupan, A. Dutta, H. Heinrich, *et al*.," Investigation of chemical bath deposition of CdO thin films using three different complexing agents," *Applied Surface Science*, vol. 257 (22), pp. 9237-42, 2011.

[126] A. Dutta and H. Heinrich, "Interfacial Atomic Number Contrast in Thick Samples," *Microscopy and Microanalysis*, vol. 20, pp. 136-137, 2014.